



NTNU – Trondheim
Norwegian University of
Science and Technology

Pelton Turbine - Model Test of a Runner

Audun Tufte Larsen

Master of Energy and Environmental Engineering

Submission date: July 2015

Supervisor: Ole Gunnar Dahlhaug, EPT

Co-supervisor: Torbjørn K. Nielsen, EPT
Bjørn Winther Solemslie, EPT

Norwegian University of Science and Technology
Department of Energy and Process Engineering

EPT-M-2015-49

MASTEROPPGAVE

for

Student Audun Tufte Larsen

Våren 2015

Pelton turbin – Modellmålinger av et løpehjul*Pelton turbine- Model test of a runner***Bakgrunn**

Blant Norges 1050 kraftverk så er det ca. 30% som har Pelton turbiner installert. Mange av disse turbinene er mer enn 40 år gamle og det er tid for oppgraderinger og eventuelt utskifting av disse. Selv om Pelton turbinen er over 100 år gammel er det fremdeles områder hvor kunnskap mangler, da spesielt innen strømmingen i skovlene. Ved Vannkraftlaboratoriet er det blitt designet en modellturbin som skal testes i laboratoriet for å bedre kunnskapen rundt strømmingen. Denne turbinen har en geometri som kan deles med alle andre FoU-miljø Det er ønskelig at målinger skal bli tilgjengelig slik at andre kan benytte dette løpehjulet til for å videreutvikle CFD til bruk for Pelton-turbiner.

Mål

Gjennomføre detaljert filming av strømning i en Pelton skovl ved Vannkraftlaboratoriet.

Oppgaven bearbeides ut fra følgende punkter:

1. Fullføre implementering av laser for belysning i Peltonriggen
2. Sette seg inn i tilgjengelige postprosesseringsverktøy for bruk med høyhastighetsfilmer
3. Utvikle prosedyrer og gjennomføre filming ned i peltonskovlen med boroskop
4. Sammenligne strømmingen i peltonturbinen ved to forskjellige dysehøyder
5. Hvis tiden tillater det kan også mulighetene for å følge partikler i vannet gjennom skovlen undersøkes.

Senest 14 dager etter utlevering av oppgaven skal kandidaten levere/sende instituttet en detaljert fremdrift- og eventuelt forsøksplan for oppgaven til evaluering og eventuelt diskusjon med faglig ansvarlig/veiledere. Detaljer ved eventuell utførelse av dataprogrammer skal avtales nærmere i samråd med faglig ansvarlig.

Besvarelsen redigeres mest mulig som en forskningsrapport med et sammendrag både på norsk og engelsk, konklusjon, litteraturliste, innholdsfortegnelse etc. Ved utarbeidelsen av teksten skal kandidaten legge vekt på å gjøre teksten oversiktlig og velkrevet. Med henblikk på lesning av besvarelsen er det viktig at de nødvendige henvisninger for korresponderende steder i tekst, tabeller og figurer anføres på begge steder. Ved bedømmelsen legges det stor vekt på at resultatene er grundig bearbeidet, at de oppstilles tabellarisk og/eller grafisk på en oversiktlig måte, og at de er diskutert utførlig.

Alle benyttede kilder, også muntlige opplysninger, skal oppgis på fullstendig måte. For tidsskrifter og bøker oppgis forfatter, tittel, årgang, sidetall og eventuelt figurnummer.

Det forutsettes at kandidaten tar initiativ til og holder nødvendig kontakt med faglærer og veileder(e). Kandidaten skal rette seg etter de reglementer og retningslinjer som gjelder ved alle (andre) fagmiljøer som kandidaten har kontakt med gjennom sin utførelse av oppgaven, samt etter eventuelle pålegg fra Institutt for energi- og prosesseteknikk.

Risikovurdering av kandidatens arbeid skal gjennomføres i henhold til instituttets prosedyrer. Risikovurderingen skal dokumenteres og inngå som del av besvarelsen. Hendelser relatert til kandidatens arbeid med uheldig innvirkning på helse, miljø eller sikkerhet, skal dokumenteres og inngå som en del av besvarelsen. Hvis dokumentasjonen på risikovurderingen utgjør veldig mange sider, leveres den fulle versjonen elektronisk til veileder og et utdrag inkluderes i besvarelsen.

I henhold til ”Utfyllende regler til studieforskriften for teknologistudiet/sivilingeniørstudiet” ved NTNU § 20, forbeholder instituttet seg retten til å benytte alle resultater og data til undervisnings- og forskningsformål, samt til fremtidige publikasjoner.

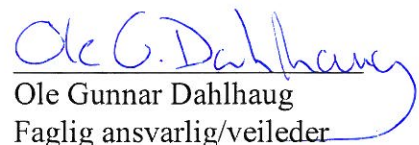
Besvarelsen leveres digitalt i DAIM. Et faglig sammendrag med oppgavens tittel, kandidatens navn, veileders navn, årstall, institutt navn, og NTNUs logo og navn, leveres til instituttet som en separat pdf-fil. Etter avtale leveres besvarelse og evt. annet materiale til veileder i digitalt format.

- Arbeid i laboratorium (vannkraftlaboratoriet, strømningsmeknikk, varmeteknikk)
 Feltarbeid

NTNU, Institutt for energi- og prosesseteknikk, 5. januar 2015



Olav Bolland
Instituttleder



Ole Gunnar Dahlhaug
Faglig ansvarlig/veileder

Medveileder(e):

- Torbjørn K. Nielsen torbjorn.nielsen@ntnu.no
- Bjørn Winther Solemslie bjorn.w.solemslie@ntnu.no

SAMMENDRAG

Selv om Pelton-turbinen er en over 100 år gammel oppfinnelse, finnes det ennå områder som mangler kunnskap. For å kunne forbedre turbinens virkningsgrad ytterligere, trengs det en dypere forståelse av skovl-designets påvirkning på strømningens oppførsel. Det har derfor blitt bygget en modellturbin med kjent geometri ved Vannkraftlaboratoriet ved NTNU, sammen med en test-rigg og oppsett for høyhastighetsfilming av strømning i skovlen.

I utgangspunktet var en del av planen å analysere strømninger ved to forskjellige dysehøyder. Ettersom målet var å finne generelle metoder for å sammenligne strømninger, ble det imidlertid, som følge av tidsbegrensninger, bestemt at dysehøyden like gjerne kunne holdes konstant, men at filmer fra to forskjellige driftspunkt skulle sammenlignes. Siden det nye oppsettet stadig var under bearbeiding ble det besluttet å utføre sammenligningen av strømningene på filmer fra det originale oppsettet. Det ble også bestemt å prioritere å fullføre implementering av det nye oppsettet fremfor å følge partikler i vannet, som opprinnelig planlagt.

Først ble filmer fra det originale oppsettet analysert ved hjelp av bildeprosesseringsverktøy. Ulike måter å kvalitativt sammenligne strømninger på ble funnet og presentert. Det var imidlertid ikke mulig å analysere bildene kvantitativt. Dessuten ble bare deler av skovlens syklus filmet.

Mulige forbedringer av oppsettet ble derfor diskutert, for å muliggjøre mer detaljert filming, samt legge til rette for kvantitativ analyse. De foretrukne forbedringene ble designet og produsert. Et nytt oppsett for høyhastighetsfilming, basert på et boroskop påmontert løpehjulet, ble deretter implementert. Oppsettet inkluderer belysning ved hjelp av en pulserende laser. Prosedyrer for installasjon og bruk av det nye oppsettet er presentert.

Det nye kamera-oppsettet ble testet og virket etter planen. Det ga nærbilder av hele den ene halvdelen av skovlen gjennom hele skovlens syklus. Dessverre fungerte ikke laseren da testingen ble foretatt, og bildene ble dermed for mørke til å bli analysert detaljert. Det endelige resultatet fra det nye oppsettet lot derfor vente på seg.

Så fort laseren blir fikset er det grunn til å tro at det nye oppsettet for høyhastighetsfilming vil kunne gi så detaljerte bilder at det muliggjør kvantitativ eksperimentell analyse av strømningen i en Pelton skovl.

ABSTRACT

Even though the Pelton turbine is more than a 100-year-old invention, there is still a lack of knowledge regarding the flow inside the bucket. A deeper understanding of the influence of bucket design on the flow behavior is necessary to enable further increase of the hydraulic efficiency. A model runner with known geometry has thus been made at the Waterpower Laboratory at NTNU, together with a test rig and setup for high-speed flow visualization.

Originally, the flows at two different nozzle heights were to be analyzed, as part of the thesis. However, since the goal was to find methods to compare flows in general, due to time limitations it was decided to compare the flows at two different operating conditions having the same nozzle height instead. Furthermore, the flow comparison was performed using films from the original setup, since the new setup was under implementation during the entire period. As it was decided to prioritize the implementation of a new experimental setup, time did neither allow for particle tracing through the bucket, as originally planned.

At first, films from the original visualization setup were analyzed, using image post-processing tools. Different ways of comparing flows qualitatively were found and presented. However, the obtained images did not enable quantitative analyses of the flow. Furthermore, the camera setup generated images from only parts of the bucket duty cycle.

Consequently, a discussion of potential improvements of the setup was carried out, to enable filming with even more details and to make quantitative analysis of the flow possible. The preferred alternatives for improvements were designed and produced. As a result, a new experimental setup for high-speed flow visualization, based on an onboard borescope, was implemented on the test rig. This included an illumination setup based on a pulsating laser. Procedures for installing and use of the new setup are presented.

The new camera setup was tested and worked successfully, providing close-up images of a whole bucket half through the entire runner rotation. However, the laser did not work during testing, so the images were too dark to analyze with much detail. Thus, the total performance of the new setup is not known yet.

However, as soon as the laser has been fixed, there is belief that the resulting setup for high-speed flow visualization will generate images, which are so detailed that quantitative experimental analyses of the flow inside a Pelton bucket is made possible.

PREFACE

This Master's thesis has been conducted at the Waterpower Laboratory at the Norwegian University of Science and Technology (NTNU), and concludes my Master of Science degree in Energy and Environmental Engineering.

I would like to express my gratitude towards my supervisor, Prof. Ole Gunnar Dahlhaug, who has given me the opportunity to be a part of a project with a greater vision, to have had faith in me to let me learn by doing, and for his motivational advice during the process.

To my co-supervisor, Bjørn Winther Solemslie, I am also full of thanks. He has done a lot more than expected as a supervisor, and patiently guided me through great advising.

I am thankful for all the help given during laboratory work, by Bård Brandåstrø, Trygve Opland and Joar Grilstad. Halvor Haukvik deserves special thanks. Without his patience and sense of perfectionism, the implementation of the new experimental setup would not have been made possible.

I am grateful to all my fellow students who have made the past year memorable, especially those of you who gave me company during the late nights.

Big thanks goes to my roommates for motivation, and for taking good care of me when home from school.

Last, but not least, thanks be to God for helping me seeing the bigger picture.

Audun Tufte Larsen
Trondheim, July 2, 2015

TABLE OF CONTENTS

Sammendrag.....	i
Abstract.....	ii
Preface	iii
Table of contents	iv
List of figures.....	vi
List of tables	viii
Nomenclature	ix
1 Introduction.....	1
2 Framework of the study	3
2.1 Previous work.....	3
2.2 Background.....	5
2.3 Methodology and objectives.....	7
3 Theory.....	9
3.1 The Pelton turbine.....	9
3.2 Water-film thickness measurements	14
3.3 Edge detection	16
4 Test rig facilities.....	19
4.1 Instrumentation	19
4.2 Calibration	21
5 Original experimental setup	23
6 Image processing.....	25
6.1 Introduction.....	25
6.2 Description of methods.....	25
6.3 Comparing the flow in the bucket for two operating conditions	26
6.4 Summary	32
6.5 Other areas of application	33
7 Possible improvements to the original setup.....	35
7.1 Bucket.....	35
7.2 Camera setup	36

7.3	Lighting.....	37
8	Implementing improvements to the setup.....	39
8.1	Bucket.....	39
8.2	Camera setup.....	42
8.3	Lighting.....	47
9	New experimental setup.....	49
9.1	General description.....	49
9.2	Illumination by means of a laser.....	51
9.3	Illumination by lamps.....	52
10	Results from the new setup.....	53
10.1	Still picture.....	53
10.2	High-speed flow visualization.....	54
11	Evaluation.....	57
11.1	Evaluation of the improvements on the setup.....	57
11.2	Image processing.....	57
12	Conclusion.....	59
13	Further Work.....	61
	References.....	
	Appendix A – High-speed visualization procedure.....	
	Appendix B – Laser procedure.....	
	Appendix C – Calibration data.....	
	Appendix D - Summary of risk assessments.....	

LIST OF FIGURES

Figure 2.1: The onboard borescope location and assembly [1]	4
Figure 2.2: Field of observation [1].....	4
Figure 2.3: Bucket dimensions.....	6
Figure 2.4: Hill-diagram for the runner of interest [18]	7
Figure 3.1: Velocity diagram for a Pelton runner [19].....	9
Figure 3.2: Main dimensions [1]	10
Figure 3.3: Top view of the bucket [1].....	11
Figure 3.4: Front view of the bucket [1]	11
Figure 3.5: Duty cycle sequence [1].....	12
Figure 3.6: Apparent grid displacement due to optical refraction [1].....	15
Figure 3.7: Simplified 2D optical model [1]	15
Figure 3.8: Interpolation in the processed image [1]	16
Figure 3.9: Result of using Canny edge detector [23].....	17
Figure 4.1: The Pelton turbine test rig.....	20
Figure 4.2: Schematic of the hydraulic system and instrumentation arrangement	20
Figure 4.3: Schematic of the calibration setup [24].....	21
Figure 5.1: Original experimental setup	23
Figure 6.1: Choice of investigation points; a) 4 mm b) 14 mm.....	26
Figure 6.2: Extent of back wash indicated by yellow lines a) 4 mm, $n_{11}=39$, b) 4 mm, $n_{11}=44$	28
Figure 6.3: The lines show the cut-out leakages. a) 4 mm, $n_{11}=39$, b) 4 mm, $n_{11}=44$	29
Figure 6.4: Edge detection, using the Canny method in a) on b). Disturbance regions are put in boxes.	30
Figure 6.5: Waterfront propagation. a) 4mm, $n_{11}=39$, b) 4mm, $n_{11}=44$	31
Figure 6.6: 4 mm nozzle opening, $n_{11}=44$. Edges of the cut-out are indicated by red lines, and the jet by yellow lines. The black line in the middle indicates the splitter location.	33
Figure 6.7 a): Misalignment of the camera relative to the turbine. The lines are vertical, showing a slight displacement in the upper left lip edge.....	34
Figure 6.8: b) The hindmost part of the image	34
Figure 8.1: Visual effect on reflection of sandblasting a bucket of the turbine of Solemslie	40
Figure 8.2: Making a grid in the bucket manually	42
Figure 8.3: CAD-drawing from the design process, illustrating the desired setup.....	43
Figure 8.4: CAD-drawing from the design process, illustrating the resulting visible area seen through the borescope, as of Figure 8.3.....	44
Figure 8.5: The optical system is split in a rotating and a stationary section.....	44
Figure 8.6: The borescope	45
Figure 8.7: Schematic of the optical system.....	45
Figure 8.8: Schematic of the supporting system	46

Figure 9.1: Installed new setup, with an onboard borescope	49
Figure 9.2: Close-up of the inside of the borescope casing.....	50
Figure 9.3: Complete installation, with the laser for lighting placed to the right. The other light sources are only used during installation	51
Figure 9.4: One optical fiber-cable for laser light placed inside a metal pipe, situated just over the nozzle exit.	51
Figure 9.5: Experimental setup with lighting from lamps	52
Figure 10.1: Visible region seen through the borescope, when no water in the system.....	53
Figure 10.2: Test with water for the old lighting setup, test 1	54
Figure 10.3: Test with water 2	55
Figure 10.4: Test with water 3	55

LIST OF TABLES

Table 2.1: Physical dimensions	6
Table 4.1: Measurement instruments and their range	19
Table 8.1: Summary of the effects of surface treatments.....	40

NOMENCLATURE

Symbol	Description	Unit
B	Bucket width	m
c	Absolute water velocity	m/s
D	Diameter	m
E	Specific hydraulic energy	J/kg
F	Force	N
f	Friction factor	-
g	Acceleration of gravity	m/s^2
Δh	Height difference	m
H_e	Effective head	m
H_{dyn}	Dynamic head	m
H_{stat}	Static head	m
Q	Mass	kg
Q_{11}	Modified speed factor	\sqrt{m}/s
N	Number of measurements	-
n	Rotational speed	rpm
n_{11}	Modified speed factor	$rpm\sqrt{m}$
n_{ED}	Speed factor	-
P	Power	W
P_m	Mechanical power	W
P_h	Hydraulic power	W
P_{Lm}	Power dissipated in bearings and shaft seals	W
p_{amp}	Atmospheric pressure	Pa
Δp	Differential pressure	Pa
Q	Volumetric flow rate	m^3/s
Q_{ED}	Discharge factor	-
Re	Reynolds number	-
u	Peripheral velocity	m/s
Z	Number of nozzles	-
W	Bucket width	m

Abbreviations

BEP	Best Efficiency Point
CFD	Computational Fluid Dynamics
IEC	International Electrical Commission
NTNU	Norwegian University of Science and Technology

1 INTRODUCTION

Hydropower has played an important role in Norwegian economy over the last century. In a time where the focus on human activities' effect on climate change increases, the importance of hydropower as a renewable energy source becomes even greater. More countries seek to substitute energy sources like coal and gas, renewable sources like hydropower. At the same, the worldwide electricity consumption is increasing, putting a further demand on better turbine performances.

Even though the Pelton turbine is more than a 100-year-old invention, there are still areas with lack of knowledge, especially regarding the flow in the bucket. Up to now, the Pelton runner has been designed using model testing and semi-empirical methods. Compared to the reaction turbines, the understanding of key phenomena is weak [1]. The flow in a bucket is both unsteady, contains two phases and develops between rotating borders. Due to the simultaneous presence of these characteristics, numerical simulations of the flow have proved difficulties. However, recent development within numerical models has raised an optimism towards using Computational Fluid Dynamics (CFD) as an important tool for performance improvements, as similar to that of reaction turbines [1]. Hence, there is a need for further experimental investigations, both to better the understanding of the effect of bucket design on the flow behaviors, and to be able to validate numerical simulations.

A model of a Pelton runner has been developed at the Waterpower Laboratory at NTNU, together with a setup for high-speed flow visualization, as part of an ongoing Ph.D. project [2]. In addition to improve the knowledge of the flow in a Pelton turbine, that project has a goal to make the design processes and results available in public.

As part of the ongoing work at the Laboratory to better the understanding of the flow in a Pelton turbine, this project will focus on detailed high-speed flow visualization in a bucket of the reference turbine, made by Solemslie [2]. The original experimental setup had already shown several weaknesses regarding the image quality, limiting the amount of information that could possibly be found of the flow, by analyzing the obtained images.

Therefore, a goal was set to improve the experimental setup, in order to perform detailed filming of the flow. To be able to measure the goal achievement, the terms *perform detailed filming* in the goal formulation was chosen by the author to be specified as: *perform filming with such detail that quantitative analysis of the flow is made possible*. Achieving such a goal would be a great step towards improving the understanding of the bucket flow, and making tools for validating CFD results.

2 FRAMEWORK OF THE STUDY

This chapter presents the motivation for the study and approach of the task. This includes previous work, a discussion of the set objectives, and the structure of the document.

2.1 PREVIOUS WORK

The following research has been done regarding the flow inside a Pelton bucket, not connected to the test rig of this study, and image post-processing.

2.1.1 Analytical studies

Based on the relative accelerations terms and the vector at all time normal to the surface, Christie [3] reconstructed the path of a water particle in a bucket. However, neglecting the change of water-film thickness, the continuity equation was not taken into consideration, leaving only approximate solutions. Hana [4] tried to improve the method of Christie. Zhang [5] theoretically analyzed the flow interactions between the jet and the bucket. Using basic mechanical and geometrical relations, he made equations describing the exact angular positions of the bucket at some critical positions during the jet-bucket interaction. Deriving the so-called extended invariance equation, he made simplifications for estimating the hydraulic efficiency and relative flow.

2.1.2 Numerical studies

Using the two-phase homogeneous model together with pressure measurements, Perrig *et al.* [6] carried out investigations of the free surface flow in a bucket. The numerical investigation proved good agreement with the experimental results. Five distinct zones in the bucket were specified, and it was showed that the regions between the middle of the bucket and the inlet contributed the most to the power delivered to the bucket. In addition, an apparent presence of the Coanda effect on the bucket backside was revealed from the numerical results, contributing with a lift force.

Rossetti *et al.* [7] used a hybrid Eulerian-Lagrangian approach to investigate the deviation capability of the bucket at different loads in various bucket regions, and its influence on the hydraulic efficiency. Moreover, an attempt was made to determine the water particle trajectories and the flow field within a rotating bucket during jet-bucket interaction. Zoppé *et al* [8] compared the results from a numerical analysis, based on a two-phase flow volume of fluid (VOF) method, with experimental data on a fixed bucket. The analysis presented a good consistency between the results, in particular concerning the pressure distribution. Hana [4] tested various commercial numerical tools against a theoretical analysis. Although getting results in the same order of magnitude, he expressed the need of experimental ways of validating the results.

2.1.3 Experimental studies

Perrig [1] divided the flow in the Pelton turbine facility into 4 regimes: (i) confined steady-state flows in the upstream pipes and distributor, (ii) free jets past the injectors, (iii) transient free-surface flows in the buckets, and (iv) 2-phase dispersed flows in the casing.

Perrig stated further that, because of the different dominant forces in the different regimes, it is impossible to fulfill the similitude criteria for both the piping and bucket flows at the same time. Thus, when up-scaling from a model to prototype for a whole system, it is necessary to have an empirical approach.

Lowy [9] investigated the various losses in a fixed Pelton bucket, with particular focus on the jet-cutting process. A discussion of which losses that were avoidable was carried out. Perrig *et al.* [10] put into evidence the unsteadiness of the free surface flow, using high-speed visualization on a bucket. Perrig [1] did further in-depth investigations with high-speed flow visualizations and a borescope, both onboard the runner and externally. He visually studied the relative flow in the bucket throughout the bucket cycle and the entire jet-bucket interaction. The water-film thicknesses was analyzed by post-processing images from the borescope filming, and the used method is discussed in detail in Chapter 3.2.

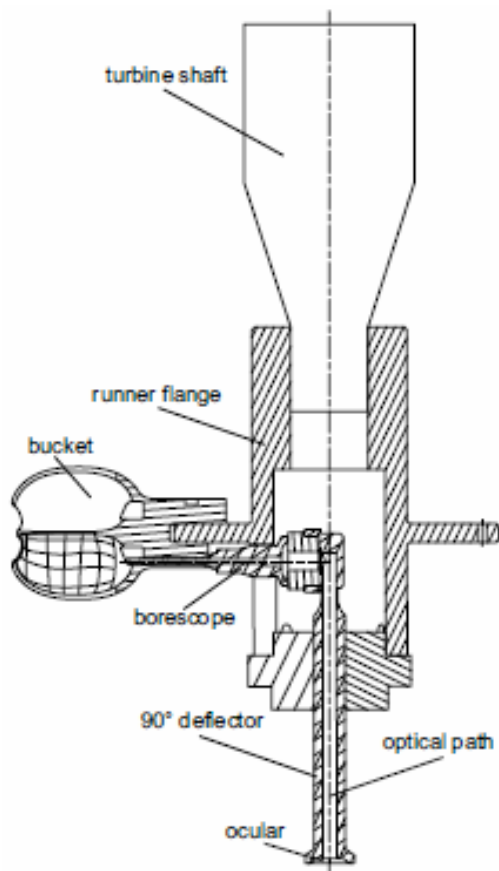


Figure 2.1: The onboard borescope location and assembly [1]

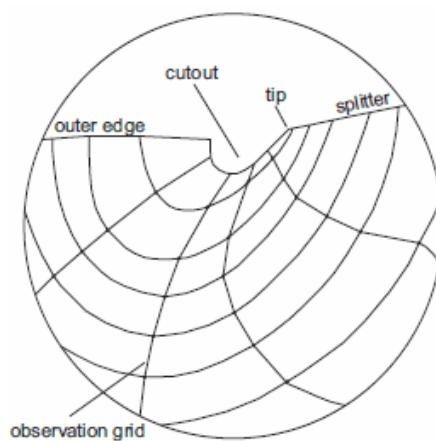


Figure 2.2: Field of observation [1]

Zoppé *et al* [8] showed that the flow pattern on a fixed bucket was independent of the test head. Perrig [1] confirmed that statement for a rotating bucket, given the relative speeds were the same. Moreover, he observed apparent flow stratification of the water sheet. Thus, crossing of streamlines or flow interferences would be possible, partly caused by the Coriolis effect. This led to a discussion of the possible occurrence of mixing losses inside the bucket, as earlier discussed by Lowy [9]. Perrig [1] further confirmed the numerical assumptions [6] of the presence of a Coanda effect on the bucket backside, leading to damages caused by cavitation. The pressure distribution inside and outside of the bucket was also investigated, showing good agreement with numerical results [6].

Staubli and Hauser [11] installed a camera, together with two strobe lights, inside a Pelton turbine casing of a prototype power plant in California. Despite the difficulties of instrumentation, they managed to analyze the jet outburst and flow structures on the jet surface through flow visualization.

Hana [4] facilitated for flow observation on a Pelton bucket to verify his results from CFD analyses. Trefall [12] did further high-speed flow visualizations on another test rig at the Waterpower Laboratory at NTNU. Comparing the performance of a model with that of the prototype, she addressed certain skepticism towards the accuracy of the scaling laws of IEC. Furthermore, she experienced how fog and water between the camera and the bucket had a bad influence on the image quality. Wessel [13] improved the experimental setup. Compared to the case of Trefall, a better camera and stronger lighting sources were used, and the camera position was changed. However, the image quality was still not found satisfactory for large volume flows and low rotational speeds.

Regarding image processing, one study comparing different edge detection techniques is that of Maini & Aggarwal [14]. By studying the available algorithms in the software MATLAB 7.0, they concluded that for almost all test cases the Canny operator performed the best at pointing out the true edges. The Canny algorithm is well known, and can for instance be found in the book “Algorithms for Image Processing and Computer Vision” by J. Parker [15]. However, another study of edge detection techniques for liquid level inspection in bottles [16] concludes that Shen-Castan’s ISEF edge detector gives better results than Canny for their special case. One reason for this, they explain, might be Canny assuming step edges, using Gaussian function to approximate edges. In contrast, ISEF is based on an exponential filter, and uses zero-crossings for detection. For smooth edges, zero-crossings often offer better localization [17].

2.2 BACKGROUND

The following work has been done at the Waterpower Laboratory at NTNU on the reference turbine of Solemslie, the same as used in this study.

2.2.1 Runner design

The model runner of interest was designed by Bjørn W. Solemslie at the Waterpower Laboratory at NTNU, and the design procedure was also made available in public [2]. Hence, the design strategy and data of design parameters were available at the Laboratory. The bucket design was specified by defining the outline of the bucket, the deepest line, and 14 curves on both sides of that line, using Bézier curves. The points were then implemented in Creo Parametric. Thus, the coordinates of the points making up the curves in the bucket, is to be found in Creo Parametric, and the rest of the coordinates in the bucket can be found by interpolation.

Originally, the runner was designed for a jet-circle diameter, D_1 , of 513.4 mm. However, early model tests performed in 2014 showed an increase in performance for a shorter D_1 [13], thus D_1 was set equal to 493.4 mm. In Table 2.1 all design parameters for the bucket are listed, together with the value of D_1 used in this report.

Because of this in-depth knowledge of the bucket design, all experimental results could be seen in light of the thought behavior of the flow. Thus, a deeper understanding of the effects of the bucket design on performance is made possible.

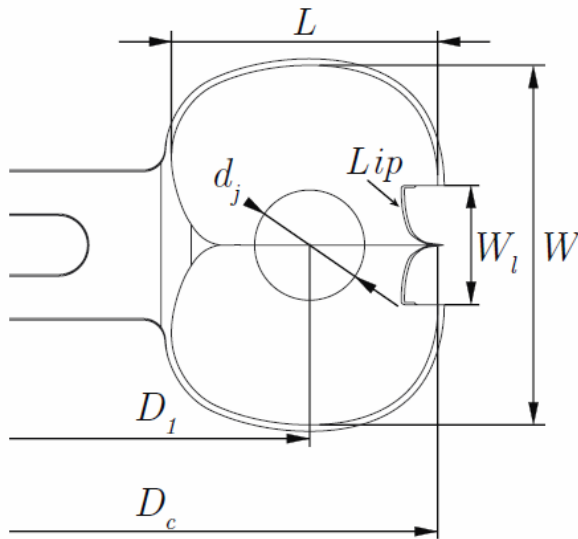


Figure 2.3: Bucket dimensions

Table 2.1: Physical dimensions

Parameter	Value
Head (H)	70.0 m
Jet-circle diameter (D_1)	493.4 mm
Tip diameter (D_c)	595.8 mm
Bucket width (W)	114.2 mm
Bucket length (L)	84.7 mm
Jet diameter (d_j)	35.0 mm
Lip width (W_l)	37.9 mm
Number of buckets	23
Pitch angle (τ)	10.90°
D_1/d_j	14.10
W/d_j	3.26
D_1/W	4.32

2.2.2 Hill-diagram and flow observations

During the author's project work in the fall of 2014, a Hill-diagram was made for the runner investigated in this thesis. The Hill-diagram is shown in Figure 2.4. Possible reasons behind the somewhat abnormal appearance, having two distinct peaks, were discussed in detail in the

project [18]. Using high-speed visualization, both cut-out leakage and back wash were observed at a great extent. Concerning the magnitude of these losses, it seemed like whereas the cut-out leakage was the largest for high runner speeds, the back wash was the largest at low runner speeds. Hence, it could be assumed that the ratio of the amount of cut-out leakage to the amount of back wash had some effect on the development of two efficiency peaks. Moreover, it was observed that for $Q_{11} > 0.015$, the jet struck into the inner edges of the cut-out, causing losses. This could explain why the measured efficiency dropped rapidly for volume flows exceeding this value. However, further investigation is needed to confirm these assumptions and, if possible, to quantify any of the observed losses. To get a better understanding of the relation between the assumed flow behavior in the design process and the actual flow behavior when testing the turbine, more advanced flow visualization techniques and image post processing are needed.

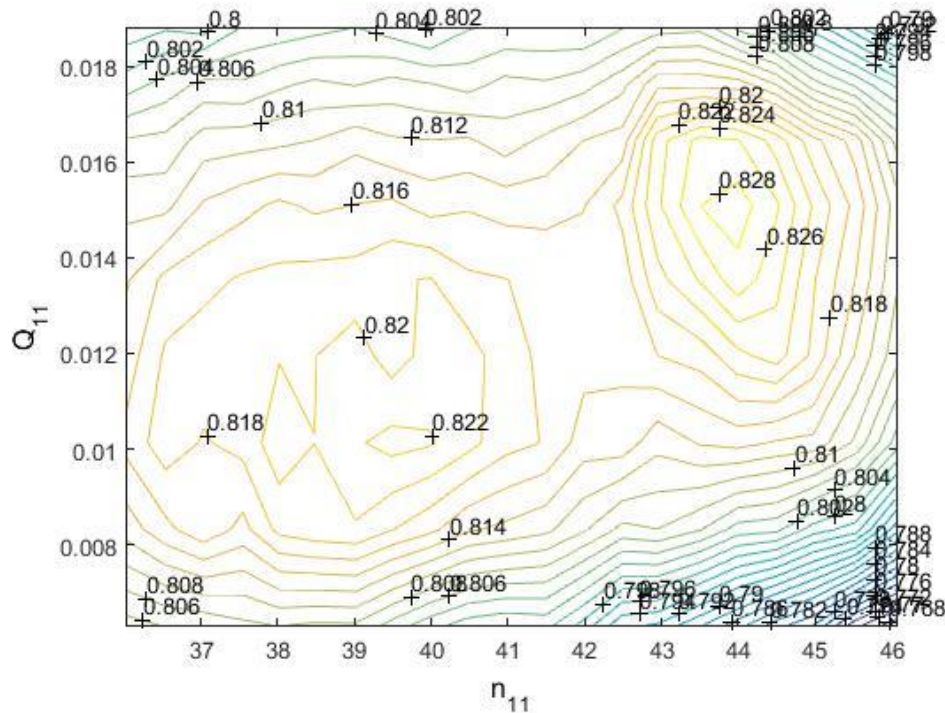


Figure 2.4: Hill-diagram for the runner of interest [18]

2.3 METHODOLOGY AND OBJECTIVES

The goal formulation of the given assignment was set to: *perform detailed filming of the flow in a Pelton bucket at the Waterpower Laboratory*. However, to be able to measure the goal achievement, the terms *perform detailed filming* in the goal formulation was chosen by the author to be specified as *perform filming with such detail that quantitative analysis of the flow is made possible*. This was considered a goal to stretch for, as quantitative flow analysis in a Pelton bucket has so far been subject of minor research. Furthermore, achieving such a

goal would imply many further possibilities for validating CFD results and better the understanding of the bucket flow.

In order to achieve that goal, the following approaches were carried through in the present study, based on the underlying objectives given in the assignment of the thesis:

- **Investigating available image post-processing tools**

This was necessary in order to be able to analyze the flow.

- **Analyzing films from the original setup, using image processing**

In order to bring to light what areas of the original setup that needed improvement, an analysis of obtained films from said setup was undertaken.

- **Comparing two flows at different operating conditions**

An underlying objective of the assignment was to compare two flows having different nozzle heights. With advice from the supervisor, this objective was changed to rather compare two flows with different operating conditions, having the same nozzle height. This was done due to time limitations. Besides, the goal was to find general methods of analyzing, thus the points chosen were not of great importance.

As a basis for comparison, the Hill-diagram obtained during the fall of 2014 was used, as shown in Figure 2.4.

- **Implementing a lighting setup by means of a laser**

A laser was already to be found at the Waterpower Laboratory, but had to be implemented together a tent for coverage.

- **Perform filming with the new camera setup**

This had to be done in order to test the new experimental setup.

- **Developing procedures for installing and use of the new setup**

To make sure that other people would be able to repeat the processes, and continue after end of this project, procedures had to be carried out.

- **Tracing particles**

Because of time limitations, this was not carried out. By advice from the supervisors, the implementation of the new experimental setup was prioritized.

3 THEORY

This chapter contains a presentation of the most relevant background theory.

3.1 THE PELTON TURBINE

The following theory is regarding the operational principle, the flow in the bucket, dimensioning and model testing.

3.1.1 Operational principle

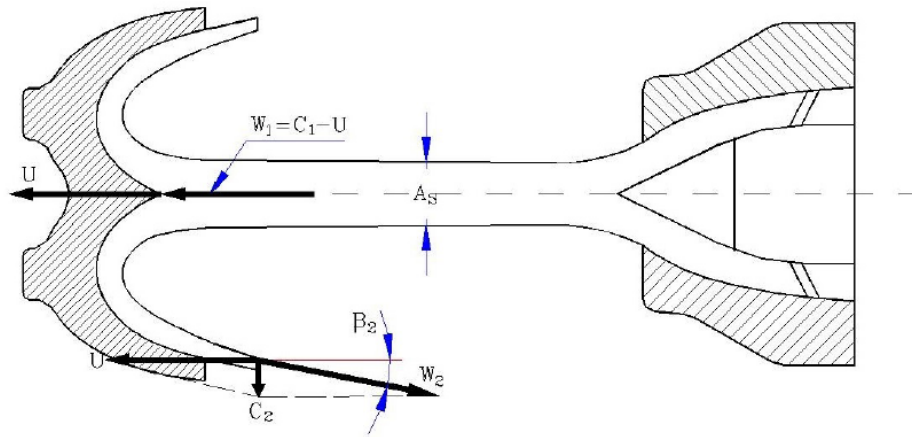


Figure 3.1: Velocity diagram for a Pelton runner [19]

The Pelton turbine is an impulse turbine, meaning that all of the energy extracted by the runner comes from a water jet, containing only energy associated with velocity. Bernoulli's equation states that the maximum speed obtainable, c_{\max} , for a water jet, is

$$c_{\max} = \sqrt{2gH_e} \left[\frac{m}{s} \right] \quad (3.1)$$

where H_e denotes the effective head driving the water, measured in meter water column, and g the acceleration of gravity. However, the losses associated with the nozzle are not taken into account when calculating the effective head. As a result, the absolute velocity for real turbines can be approximated to $c \approx 0.97c_{\max}$ [20]. Figure 3.1 shows the velocity diagram, where subscript 1 denotes the bucket inlet, subscript 2 denotes the bucket outlet. The figure illustrates that the flow exiting the nozzle only has a component in the peripheral direction, $c_{u1} = c_1$. As the runner itself is moving with a peripheral velocity, u , the velocity contributing to the acting force on the runner is the relative velocity, $w = c - u$. By balancing the forces on the runner, it can readily be shown that the optimal peripheral velocity is $u = 0.5c_1$ [19].

3.1.2 Optimal dimensions

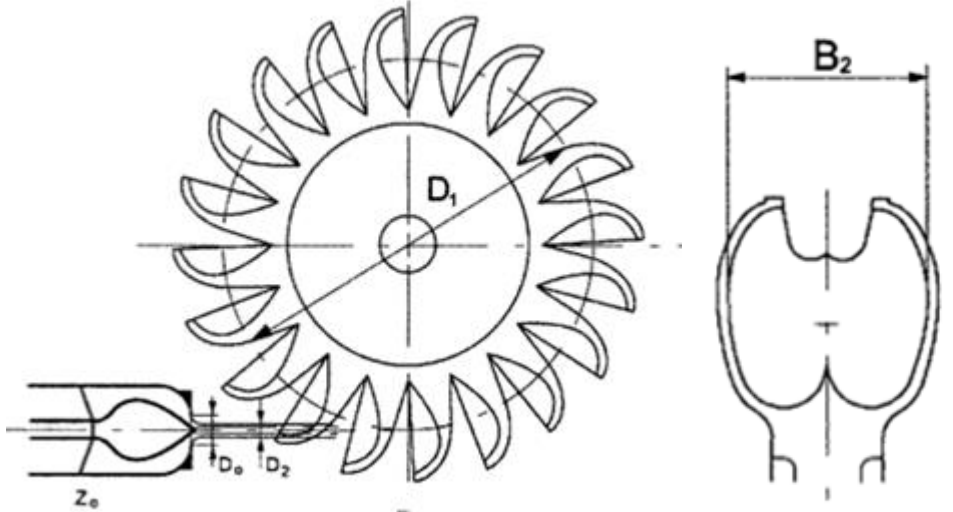


Figure 3.2: Main dimensions [1]

It is common to operate with dimensionless variables, as this makes scaling a lot easier. c_{\max} is used for this purpose, hence $c_{ref} = \sqrt{2gH_e}$. Thus, the reduced version of the Euler turbine equation for flow without losses then takes the form

$$\eta_h = 2(\underline{u}_1 \underline{c}_{u1} - \underline{u}_2 \underline{c}_{u2}) [-] \quad (3.2)$$

where η_h is the hydraulic efficiency, and subscript 1 and 2 denotes the inlet and outlet of the bucket, respectively [21]. The largest possible efficiency is obtained when $\underline{c}_{u2} = 0$. At this point the absolute velocity of the water coming out of the bucket, is directed 180 degrees away from the inlet jet. This occurs when $u = 0.5c_1$.

When designing a Pelton turbine it is necessary to let some of the variables be based on experience, or “rules of thumb” [21]. One starts by assuming $\underline{c}_{u2} = 0$ at best operating point, knowing that this is seldom completely accurate. Taken losses into consideration, the hydraulic efficiency is set to $\eta_h = 0.96$. Hence, using Equation (3.2) $\underline{u}_1 = 0.48$. The diameter of the water jet, d_2 , can then be determined using the continuity equation

$$d_2 = \sqrt{\frac{4Q}{Z\pi c_{u1}}} [m] \quad (3.3)$$

Here Q denotes the total volume flow rate, in cubic meters per second, and Z the number of jets. Next, the diameter of the nozzle opening, d_0 , can be set to be approximately $1.3 d_2$ [21]. The bucket width, B , is normally $3.1-3.3 d_2$, increasing with increasing number of jets. The diameter of the runner, D_1 , is determined by the ratio D_1/d_2 , and is thus connected to the bucket width as well. To make sure all water is caught by the buckets, the runner diameter has to be big enough to make room for enough buckets. Additionally, a small D_1/d_2 , may lead to cavitation on the backside of the bucket lips. Consequently, D_1/d_2 is seldom less than 9.5, even for small heads lower than $H = 400\text{m}$ [21].

3.1.3 Geometry of the bucket

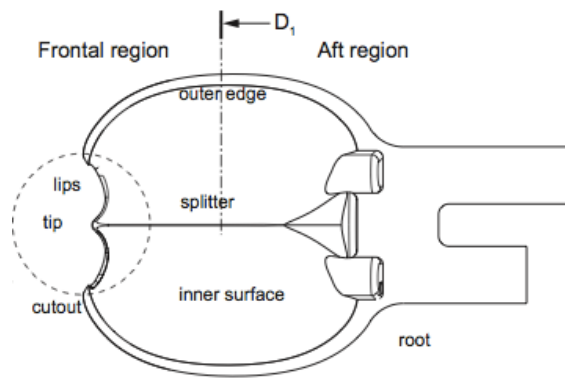


Figure 3.3: Top view of the bucket [1]

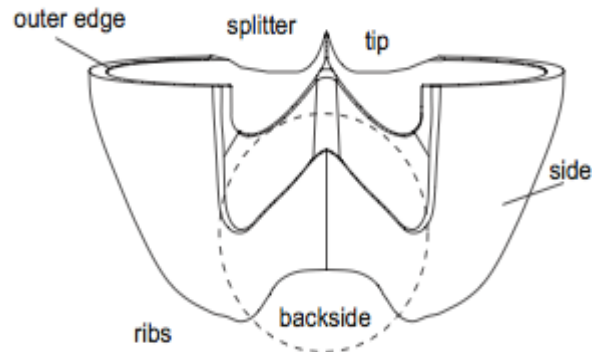


Figure 3.4: Front view of the bucket [1]

Looking at a relative force balance on a single bucket, it can readily be shown that $w_{u1} = -w_{u2}$ gives the greatest net force acting on the bucket [19]. This means that the water from the jet should be turned 180 degrees by the bucket, in order to achieve the highest efficiency. However, this would also mean that the exiting water from one bucket would potentially hit the succeeding bucket on the backside, contributing to a torque in the negative direction. To avoid this phenomena called back wash, a small angle, β_2 , with the peripheral direction is made on the inside of the bucket outer edge. The shape of the cut-out area and bucket backside has to be designed as to not interact with the jet on a too early stage, so-called inlet heeling [1]. At the same time, the gradient just in front of the lips in the bucket inside should be made big enough to avoid the water taking the “easy way out”, leading to cut-out leakage. In general, smooth transitions in the inner surface gradients should be aimed for, in order not to create abrupt changes in direction for the water particles. In order to avoid the jet getting split too rapidly, the splitter angle should be less than 20 degrees [1]. The width of the cut-

out has to be wide enough to give space for the incoming jet, although making sure that the ratio D_1/B is big enough to avoid cavitation [19].

3.1.4 Bucket duty cycle

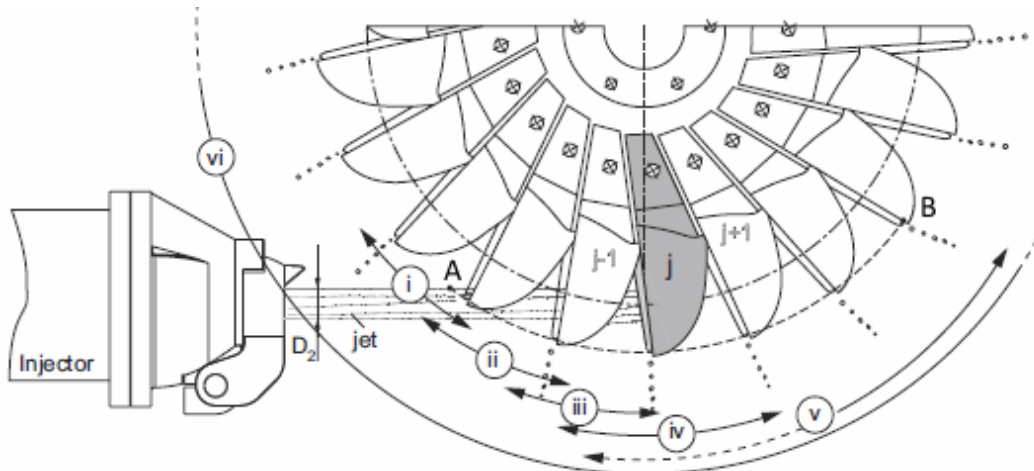


Figure 3.5: Duty cycle sequence [1]

The duty cycle of any bucket, j , ranges from the first interaction between the jet and the bucket, to the point in which the last part of the water sheet evacuates the same bucket. For convenience, the flow sequence can be divided into steps, as done by Perrig [1] in Figure 3.5. The duty cycle, where the water is contributing to the runner torque, is approximated on the figure as the arc AB . Since the exact points where the different steps will start and end depend on several parameters like the runner geometry, jet velocity and runner speed, the steps illustrated in Figure 3.5 overlap each other, showing the potential areas for places where the steps could start. However, for one specific turbine, step (ii) to (v) are supposed to start where the preceding step ends. A univocal datum, where the angular position of bucket j is equal to zero (*i.e.* $\theta_j = 0^\circ$) is needed. It can be defined as the point where a virtual point on the bucket j splitter on the circle of D_1 meets the middle of the jet front, as seen at the end of step (iii) on Figure 3.5 [1].

The characteristics of the different steps are as follows, with approximate bucket positions given as for the runner of Perrig [1]:

Approach of the tip to the jet ($\theta_j < -40^\circ$): The jet surface gets a little disturbed by water droplets dripping off the oncoming bucket.

Initial feeding process ($-40^\circ < \theta_j < -10^\circ$): From the point where the bucket gets contact with the first single water filament to the point where the jet is fully separated. In this step,

the jet is divided into two separate branches. The resulting flow sheet inside the bucket evolves and the outflow process starts at the end of this step.

Entire separation of the jet ($-10^\circ < \theta_j < 0^\circ$): The jet is now fully separated, and feeds bucket j mainly normally to the splitter.

Last stage of inflow ($0^\circ < \theta_j < 15^\circ$): The last contact phase with the jet, which somehow could be distorted due to jet outburst. Some of the water may escape through the cut-out.

Last stage of outflow ($15^\circ < \theta_j < 50^\circ$): The water sheet inside the bucket gets thinner and thinner as more water exits, until it all breaks up.

Series of droplets ($50^\circ < \theta_j < \infty$): There will always be some droplets releasing from the outer edges and splitter throughout the entire runner periphery.

3.1.5 Model testing

In order to predict the performance of a prototype turbine, performing a model test can be an important tool. The standard for model testing, IEC 60193 [22], defines the hydraulic efficiency, η_h , as

$$\eta_h = \frac{P_m + P_{Lm}}{\rho g Q H_e} = \frac{\omega(T_m + T_{Lm})}{\rho g Q H_e} [-] \quad (3.4)$$

P_m denotes the mechanical power delivered to the shaft, P_{Lm} the friction losses in the bearings, and T the mechanical torque for the respective parts. H_e is the effective head, ω the rotational speed in rad/s, ρ the density of the water, g the gravitational acceleration and Q the inlet volume flow.

To compare the results from the model with that of the prototype, similar hydraulic conditions for both cases is necessary [22]:

Dynamic similarity: All the forces acting on the prototype have to be equally scaled down to those acting on the model, meaning that ideally both Reynolds, Weber and Froude numbers should be equal. However, this is hard to obtain. As a result, IEC 60193 [22] recommends prioritizing the Fr -similitude, as this is a sensitive parameter when it comes to correcting for the efficiency using up-scaling laws. We is easier to correct for, as well as Re , as the friction factor is nearly constant when Re is turbulent.

Geometric and kinematic similarity: All dimensions should be scaled equally, and the velocity diagrams kept the same. Although, considering the relative surface roughness, geometric similarity is almost impossible to obtain.

Keeping $\underline{Q}/D_1^2 = \text{const}$ and $\underline{\omega}D_1 = \text{const}$ the geometric similarity considerations are preserved [20]. By combining these relations, one can derive new numbers that are useful for connecting the model with corresponding values for the prototype. Concerning runner speed and volume flow rate, several different versions of these numbers are in practice today. In Norway, normal practice is to use a pair of semi-dimensionless numbers, called unit speed and unit flow, respectively

$$n_{11} = \frac{nD_1}{\sqrt{H_e}} [\text{rpm}\sqrt{\text{m}}] \quad (3.5)$$

$$Q_{11} = \frac{Q}{D_1^2 \sqrt{H_e}} \left[\frac{\sqrt{\text{m}}}{\text{s}} \right] \quad (3.6)$$

When testing a model in the laboratory, the measured efficiencies for all relevant operating points are plotted against both n_{11} and Q_{11} , making up the so-called Hill-diagram.

3.2 WATER-FILM THICKNESS MEASUREMENTS

One way of validating results from numerical simulations is the measurement and comparison of water-film thicknesses. As of the author's knowledge, no one has yet been able to calculate the thickness of the water-film analytically. Thus, it is left to experimental tests to validate the thicknesses given by numerical solutions.

Because of refraction of light in water, the water-film in a bucket will induce an image of the background, which is displaced compared to the real background. The extent of displacement is dependent on the water-film thickness. Thus, by marking the inside of the bucket with known points, it is possible to measure the water-film thickness in one image by comparing it with another image without water in the bucket. Figure 3.6 shows an apparent grid displacement due to optical refraction, where the dashed lines illustrates the induced grid, whereas the continuous lines are the ones marked on the bucket [1].

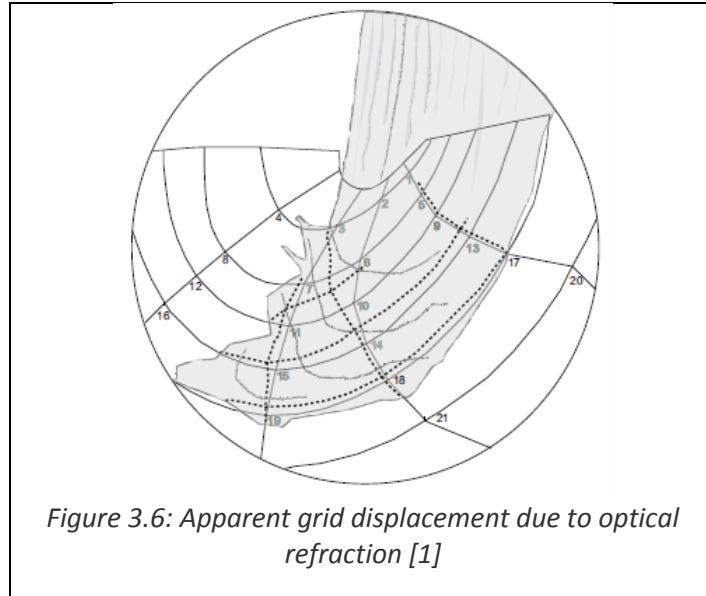


Figure 3.6: Apparent grid displacement due to optical refraction [1]

Assuming that the borescope distal lens can be reduced to a single point, and that the water-film surface is parallel to the bucket surface, Perrig [1] states that the problem can be approximated to a two-dimensional problem, as shown in Figure 3.7.

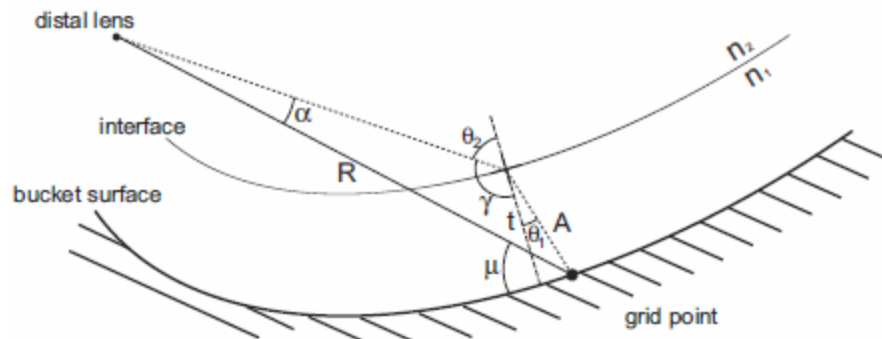


Figure 3.7: Simplified 2D optical model [1]

Using the Sine theorem and the Law of refraction it can be shown [1] that the water-film thickness, t , can be expressed as

$$t = \frac{R \cos \theta_1}{\sin(\theta_2 - \theta_1)} \sin \alpha \quad [m] \quad (3.7)$$

As illustrated in Figure 3.7, R represents the distance from the lens to the real grid points. Together with the angle μ , R is to be found in the CAD model of the bucket, where all positions are known. θ_1 and θ_2 denotes the refraction angles in water in air, respectively, and α the

apparent displacement angle. Using the fact that $\theta_2 = \alpha - \mu + \pi/2$ together with the Law of refraction, both refraction angles can be defined. Thus, the only unknown variable is the apparent displacement angle, α . Through post processing, the image of interest can be put together with an image showing the grid in a dry bucket. This way, the apparent displacement vector from one grid point j to the displaced grid point j' , can be calculated directly through interpolation, as schematized in Figure 3.8 [1]. Here, a reference datum is set of one's own choice. The displacement angle at one grid point, j , can hence be found as [1]

$$\alpha_j = \frac{\Delta y^2 + \Delta z^2}{\sqrt{(y_{j+1} - y_j)^2 + (z_{j+1} - z_j)^2}} (\mu_{j+1} - \mu_j) [^\circ] \quad (3.8)$$

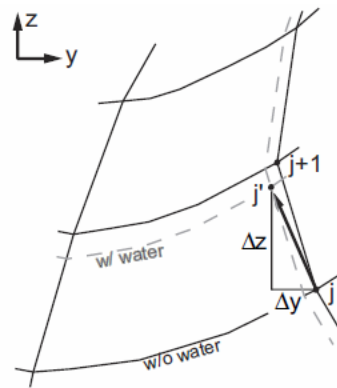


Figure 3.8: Interpolation in the processed image [1]

3.3 EDGE DETECTION

Within the scheme of image processing, edges inside an image play an important role, characterizing the boundaries of an object and thus its localization. Hence, finding the edges, or edge detection, is one of the most commonly used operations within image processing today [15]. An edge can be defined as a local abrupt change in pixel intensity [14]. As small changes in pixel intensity can be found everywhere in an image, the challenge for edge detection is to filter out noise and useless information, while still preserving the necessary structural properties. Usually an edge detector has to perform several operations before an edge can be located [15], [17]:

- **Smoothing**
Suppressing as much noise as possible using a low-pass filter, without smoothing the edges.
- **Enhancement**
Sharpening the edges by applying a filter. Histogram equalization may also be used, if necessary.

- **Detection**
Determining which pixels to spare, and which to be regarded as noise. Using lower or upper thresholds might be a tool.
- **Localization**
Determining the exact location of an edge, as the width of an edge usually covers several pixels. This could also involve edge thinning and linking between parts of lines, which may have been separated due to filtering.

However, these actions influence the performance of one another, thus imposing inevitable trade-offs. For instance, a larger filter will reduce more noise, but at the same time, it will add uncertainty to the localization of the edge. This also comes to choosing the values of thresholds, thinning or linking. As a result, it is difficult to design a general edge detection algorithm that performs well in all contexts [23]. Consequently, there have been a lot of research on this topic over the history, and a variety of different algorithms can be found today. Hence, it is crucial to have a good understanding of the algorithms, before choosing one for one's special case.

The majority of different methods may be grouped into two categories, according to their way of using derivatives in detection [14]: Gradient based and Laplacian based edge detection. While gradient methods detect edges by searching for minima and maxima of the first derivative of the pixel values, the Laplacian method looks for zero-crossings in the second derivative. Figure 3.9 shows an example of using the Canny edge detector on an image, with different shapes of edges.



Figure 3.9: Result of using Canny edge detector [23]

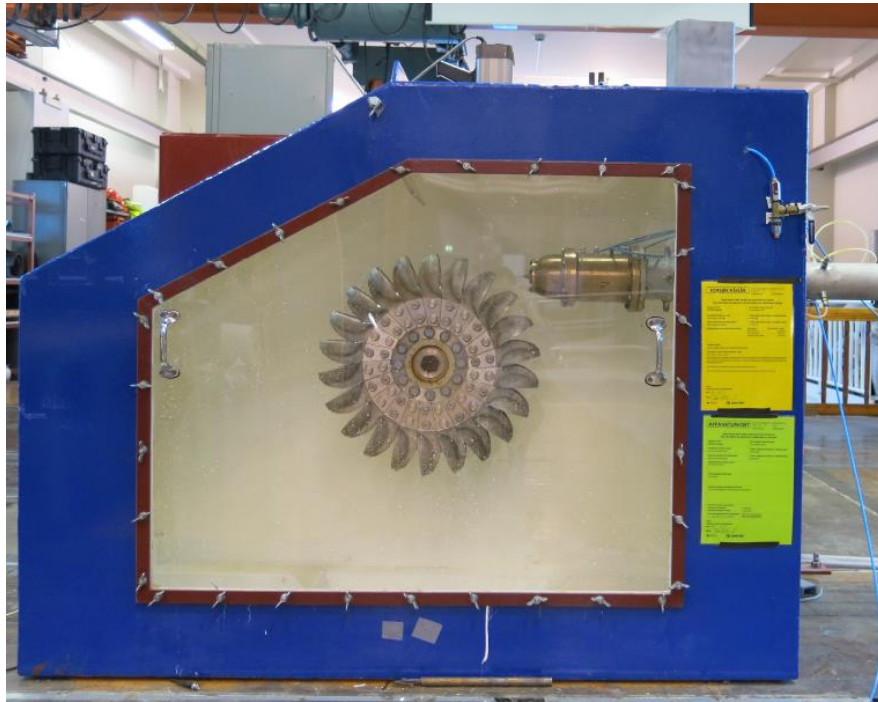
4 TEST RIG FACILITIES

4.1 INSTRUMENTATION

The experiments were conducted in a single jet, horizontal axis Pelton turbine test rig at the Waterpower Laboratory at NTNU. The turbine was connected to a 55 kW DC generator. The maximum capacity of the centrifugal pump driving the test rig was $Q \approx 100$ l/s, providing a maximum head for the turbine of $H = 100$ m. A picture of the test rig and schematic of the hydraulic system and instrumentation arrangement are shown in **Error! Reference source not found.** and Figure 4.2, respectively. The instrumentation for the test rig has been in accordance with the IEC 60193 standard [22]. All analogous measurement signals were converted, sent through a National Instruments logging card and processed in a specialized LabView program. Hence, all instruments were connected to the same computer, monitored from the control room. To ease the data logging process, current and frequency signals from instruments were converted into corresponding voltage values. As illustrated in Figure 4.2, the electromagnetic flow meter, thermometer and pressure transmitter were situated along the distributor pipe. The torque was measured with a rotating torque flange mounted on the shaft, and the friction torque was measured with a beam force cell connected to the shaft bearings. The rotational speed was measured using an infrared light source and a photodetector, connected to the torque flange. The physical properties measured are listed in Table 4.1, together with their measurement instruments and their range.

Property	Instrument	Max value
Torque	HBM T10F/FS	500 Nm
Flow rate	Krohne Aquaflux F 2000	100 l/s
Pressure	Druck PTX 1830	100 m
Friction torque	HBM Z6 Beam Force Cell	12.5 Nm
Rotational speed	Optical rotameter	-
Water temperature	PT-100 element	-

Table 4.1: Measurement instruments and their range



4.1: The Pelton turbine test rig

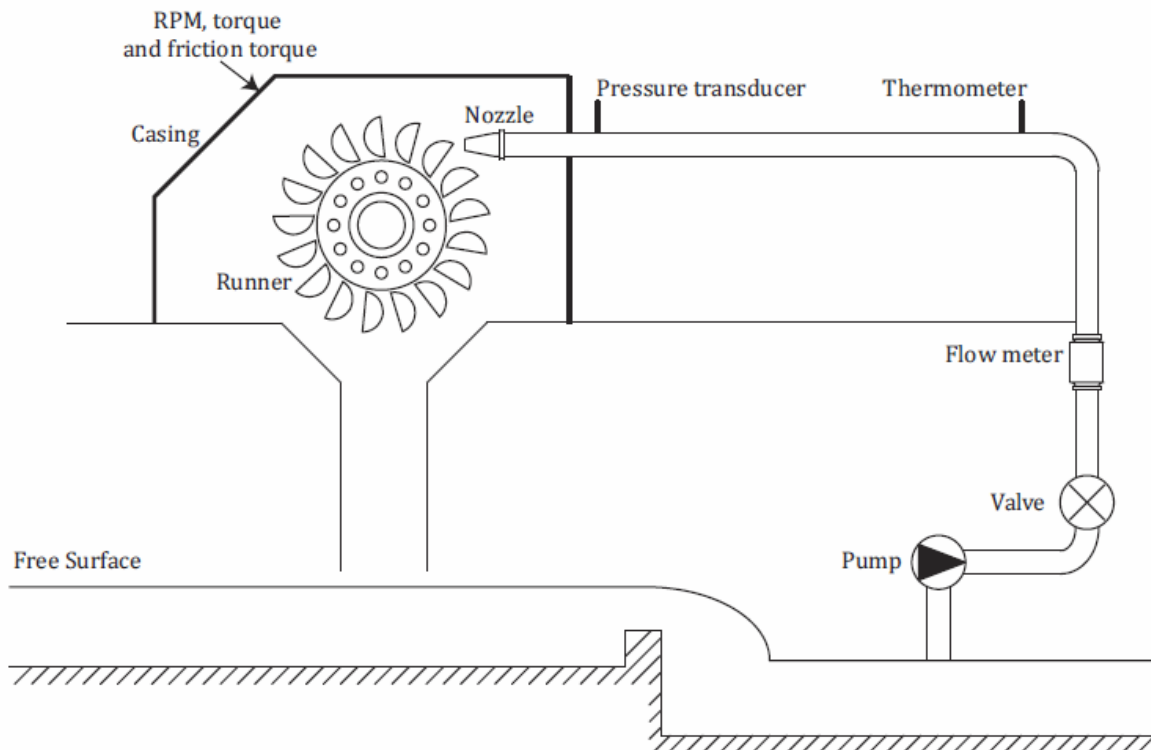


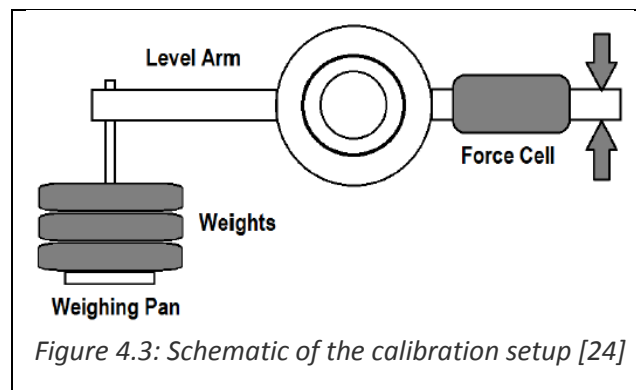
Figure 4.2: Schematic of the hydraulic system and instrumentation arrangement

4.2 CALIBRATION

Before performing a model test, it is important to calibrate the instruments in order to correct for any possible drifts since last calibration. Following the recommendations of IEC 60193 [22], all instruments were calibrated during the author's project work [18] in the fall of 2014. An investigation of calibration reports at the Waterpower Laboratory at NTNU for the past years concluded that only the calibration results from friction torque showed any kind of drifting tendency from year to year. Thus, it was decided to make a new calibration of the friction torque only. Calibration methods for those done in the fall of 2014, along with calibration data and corresponding uncertainties, are to be found in Appendix C.

4.2.1 Friction torque

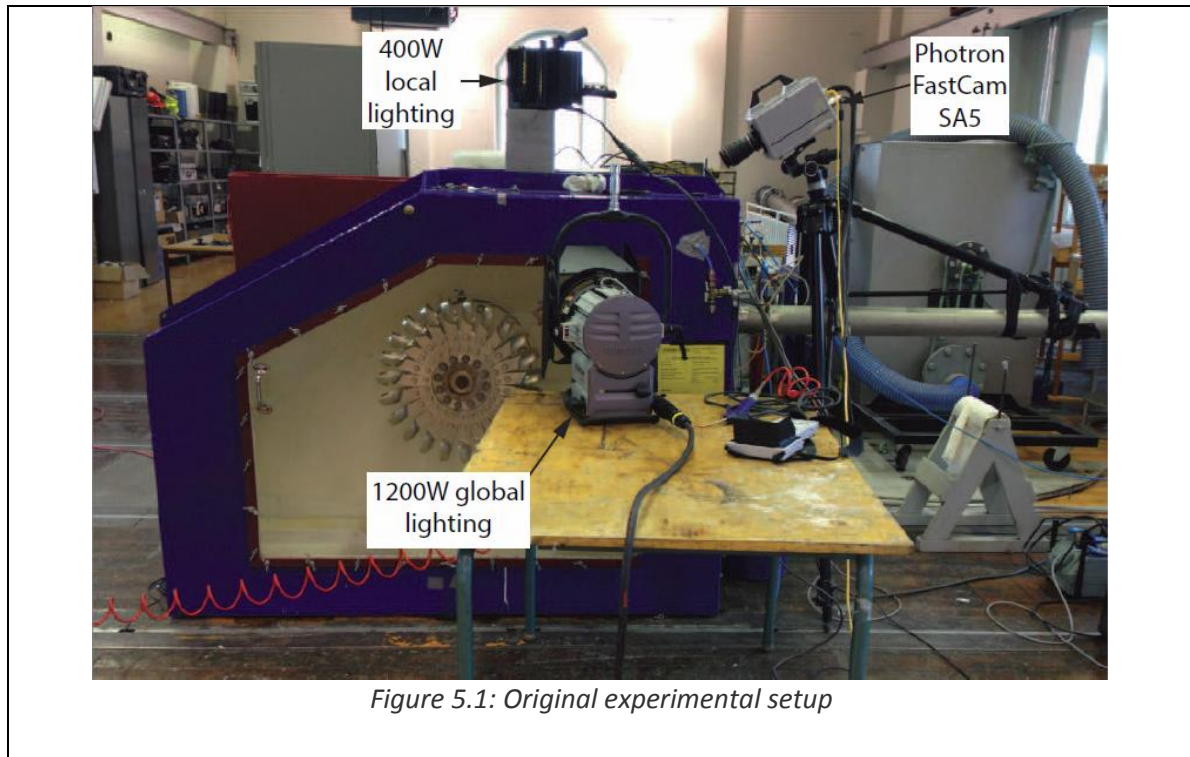
The main shaft was connected to the inside of a cylinder by two roller bearings, and to the generator by a torque flange. A beam force cell was connected to the same cylinder, which took up and measured the torque by the roller bearings. The schematic of the calibration setup is given in Figure 4.3. Following the friction torque calibration procedure of Reinertsen [24], the torque transducer was first disconnected from the flange connected to the generator shaft. This had to be done in order to measure the friction of the bearings alone. Since the level arm was known, putting different, known weights on the weighing pan gave torque values to calibrate against the measured voltage values. The voltage range was set to 0-10 V, to make sure the force cell would not go into saturation. To remove any influence of stick friction, a light knock on the bearing block was given in between each increase, or decrease, of weight on the weighing pan. The hysteresis effect in the force cell was evident during calibration. Hence a double set of points were measured, both with on-load and off-load of weights.



As for all the other calibrations, for each pair of corresponding values logged, thousands of consecutive calculations of the measured values were undertaken in a specialized LabView program. After the variations between the values had become satisfyingly small, the average of the last values was plotted against each other. Then a relationship between the torque and voltage values was obtained, and a linear approximation found. The results, along with measured uncertainties, are to be found in Appendix C.

5 ORIGINAL EXPERIMENTAL SETUP

The model tests and high-speed filming with the original setup were conducted during the fall of 2014 [18]. Hence, the films analyzed for the original experimental setup are taken from that work. The setup is shown in Figure 5.1.



The high-speed filming was conducted with a Photron Fastcam SA5. The camera is capable of recording up to 750,000 frames per second (fps), though at the expense of the resolution. At full resolution (1024 x 1024 pixels) it can provide recordings at frame rates up to 7000 fps. The camera is installed with 16 GB of internal memory, which at maximum framerate at full resolution is equivalent to a capacity of 1.56 seconds of recording, or 10,918 frames. For instance, at a runner speed of 600 rpm, and the above-mentioned preferences, the camera can record up to 15 revolutions of the runner, having 700 equally spread images displaying each revolution. The lens used was a Sigma 105 mm f.2,8.

The turbine was illuminated by a 1200 W HMI Fresnell lamp in front of the rig, and a 400 W Dedolight D lamp placed on top of the rig. A trigger was placed in connection with the rotational measurement device, and controlled by a computer. The camera was controlled by the computer, and started its recordings by a synchronization signal based on the trigger. Thus, all films started at the same angular position. To ensure the films from different rotational speeds could be comparable, a program was made in LabView to calculate and set the synchronous frame rate on the camera. This way, all films were equal regarding the

angular position of the turbine in each frame, and hence two images from two different runner speeds were made comparable. However, the shutter speed needed to be adjusted manually according to the change of flow and runner speed, in order to ensure same lighting conditions.

6 IMAGE PROCESSING

6.1 INTRODUCTION

To be able to explain the differences in runner performance for two different operating points, several phenomena were decided to investigate through image processing: the extent of back wash, extent of cut-out leakage and waterfront propagation. While the back wash and cut-out leakage were analyzed only qualitatively, an attempt to analyze the waterfront propagation quantitatively was made. In addition, image processing was used to locate the jet, calculate potential misalignment with the runner, as well as the alignment of the camera relative to the runner. This was investigated due to the primitive method of directing the jet in the original experimental setup.

6.2 DESCRIPTION OF METHODS

The waterfront in the bucket was attempted traced using an algorithm based on the “Canny” edge detector algorithm in MATLAB. In brief, the algorithm first specified the area of investigation and then used the Canny-detector to reveal any apparent edges in the image in all directions, for each succeeding frame in a given film. The waterfront was also traced manually, by putting succeeding frames on top of each other, and examining the differences between the images. Firstly, the frame with the first occurrence of outflow was found for each operating point, as a basis for comparison. Then the waterfront was traced backwards for the preceding frames, for as many frames as needed. The change in angular position of the bucket between each succeeding frame is the same independent of the runner speed, as a result of the triggering mechanism.

Edge detection was also used to locate the jet, relative to the lip opening. By examining the gradients of the pixels in the horizontal direction of the image, all vertical edges over a given threshold were found. By investigating the region between the nozzle opening and first bucket in contact, the edges of the jet as well as the nearly vertical cut-out edges were found. This way, the parallel displacement of the jet was found, and the relative bucket load calculated. Moreover, by using the same method of tracing the edges, only adjusting the region of investigation to cover the entire image, it was possible to reveal any tilting of the camera relative to the runner, in addition to the straightness of the jet. The obtained results of performing an edge tracing were complete vertical lines. Thus, looking at the hindmost part of the image farthest away from the nozzle opening, one could compare the actual cut-out edges and jet edges with the obtained vertical lines.

Considering the extent of back wash and cut-out leakage, the comparison was made on basis of the frame in each operating point showing the most visible losses.

6.3 COMPARING THE FLOW IN THE BUCKET FOR TWO OPERATING CONDITIONS

This chapter presents the results from the post processing of films, conducted for the original experimental setup. The flow in the Pelton bucket at $H = 30$ m and nozzle opening of 4 mm is compared for the two cases of runner speeds of $n_{11}=39$ and $n_{11}=44$. Possible reasons for the differences in behaviors are discussed, and their possible effects on the hydraulic efficiency. In all figures comparing the flows, the right side of the bucket has been used as basis for comparison. However, to ease the comparison through symmetry, the left hand side image in each of those images are mirrored.

6.3.1 Choice of operating points of investigation

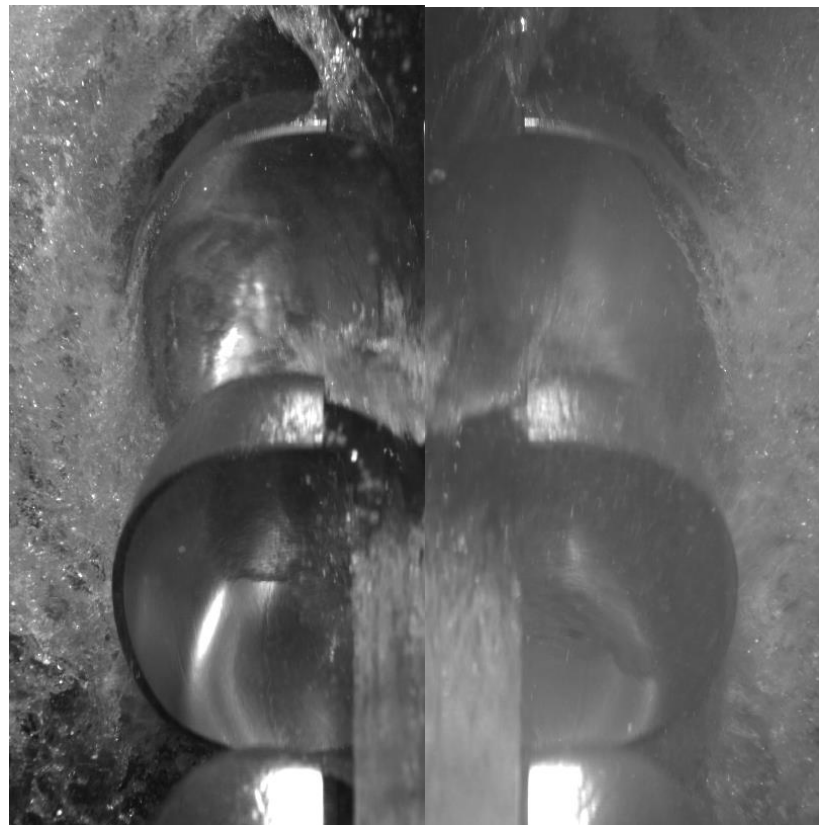


Figure 6.1: Choice of investigation points; a) 4 mm b) 14 mm

One of the goals of the thesis was to find ways to get information of the flow in a Pelton bucket by using post-processing tools on the images. The point of comparing films from two different operating points was merely to show how this information can be used to better understand why the runner performance change when changing the operating conditions, based on image analysis. Thus, for this point of view, the only requirement to which points to investigate was that the images could be analyzed.

The available films to investigate were taken with the original experimental setup. Clearly, the quality of the films were very different, depending on the amount of water in front of the camera and lighting sources. Figure 6.1 shows the differences between the images taken at nozzle openings of $\gamma = 4$ mm and $\gamma = 14$ mm, corresponding to flow rates of $Q_{11} = 0.0083$ and $Q_{11} = 0.0164$, respectively. Both films were conducted at $H = 30$ m and runner speed at $n_{11} = 39$. Both images are taken of the right bucket half, while the image of $\gamma = 4$ mm is mirrored to ease the comparison through symmetry. In the right hand image with $\gamma = 14$ mm, it is almost impossible to recognize the waterfront close to the bucket outer edge. Moreover, the darkness in the image forced a use of a higher shutter speed, which in turn made the image more blurry. This effect got even worse for higher heads, as the volume flow rate got bigger. Thus, the chosen points of investigation needed to be at a relatively low head with low flow rates.

The obtained Hill-diagram of the runner of interest, as shown in Figure 2.4, was used as a basis for the flow comparison. The data showed that the hydraulic efficiency of the runner when $\gamma = 4$ mm was 82.0 % at $n_{11} = 39$, while reduced to 80.3 % at $n_{11} = 44$ – a reduction of 1.7 %. As Figure 6.1 shows, the image taken at $\gamma = 4$ mm, $n_{11} = 39$ and $H = 30$ m also gave a clear visible image. Thus, the goal was left to compare films at these two operating conditions, using image post-processing, in order to explain the difference in runner performance

6.3.2 Back wash

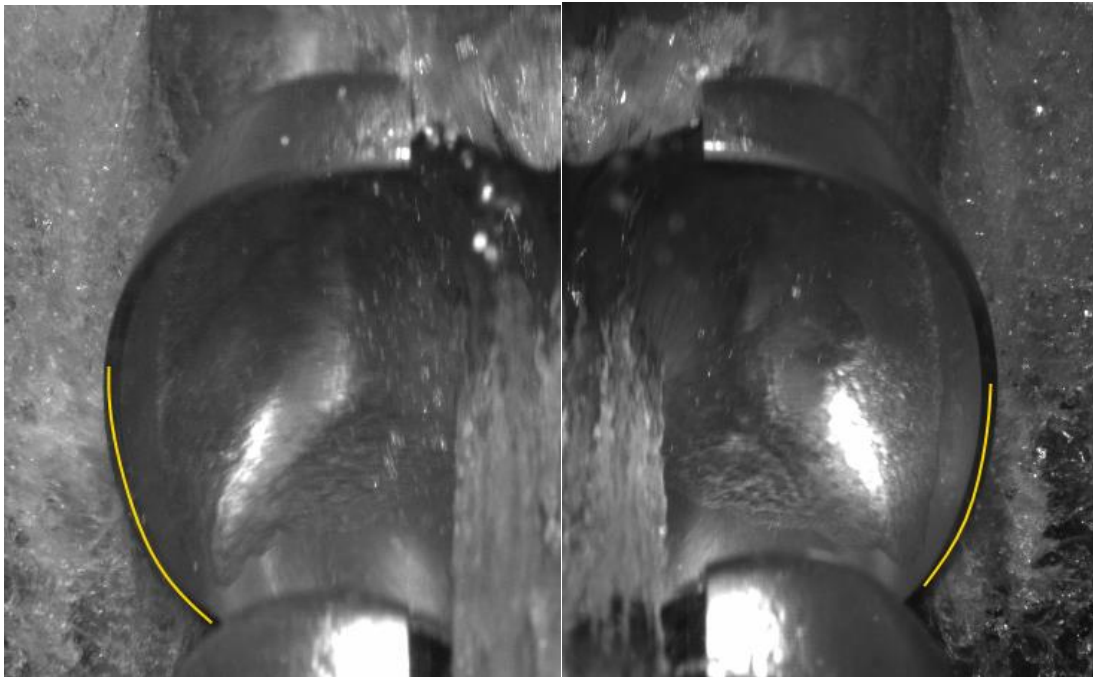


Figure 6.2: Extent of back wash indicated by yellow lines a) 4 mm, $n_{11}=39$, b) 4 mm, $n_{11}=44$

The yellow lines along the outer bucket edges in Figure 6.2 show the area where back wash is observed. The images are taken at the respective frames having the largest extent of back wash. Clearly, the extent of back wash is the least at the right hand side image, with $n_{11}=44$. This can readily be explained by looking at the outlet velocity diagram of a Pelton turbine. As u_2 increases, the direction of c_2 changes more towards the direction of u_2 . Hence, less water strikes the succeeding bucket, and more back wash is avoided. The quantitative contribution of the back wash to the total efficiency loss is rather difficult to measure. However, as seen in Figure 2.4 of the Hill-diagram, the efficiency is 1.7 % larger for the case having the most back wash, meaning that there are other losses present which sum of contributions are larger for the case with the least back wash.

6.3.3 Cut-out leakage

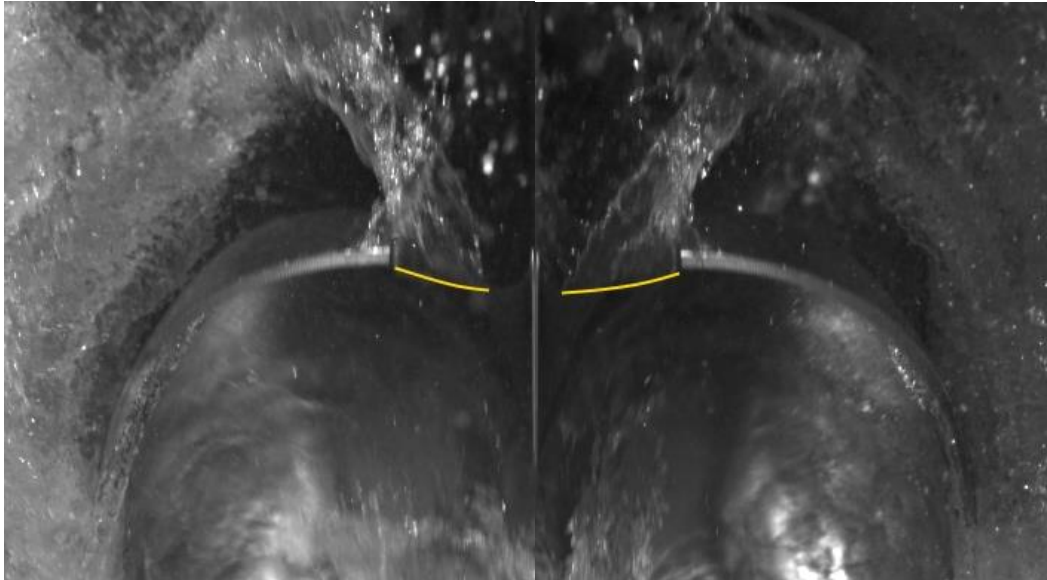


Figure 6.3: The lines show the cut-out leakages. a) 4 mm, $n_{11}=39$, b) 4 mm, $n_{11}=44$

Another type of losses is water running through the turbine without being utilized, *i.e.* cut-out leakage. In Figure 6.3, the yellow lines along the bucket lips indicate the region where cut-out leakage is observed. The images are taken at the frames having the largest extent of cut-out leakage, for $n_{11}=39$ and $n_{11}=44$, respectively. The left hand side image has been mirrored to ease the comparison. Evidently, the most water escapes through the cut-out for the case with the largest runner speed. This is a consequence of the higher rotational runner speed giving less resistance for the water to enter through the cut-out.

6.3.4 Waterfront propagation: edge tracing with the Canny method

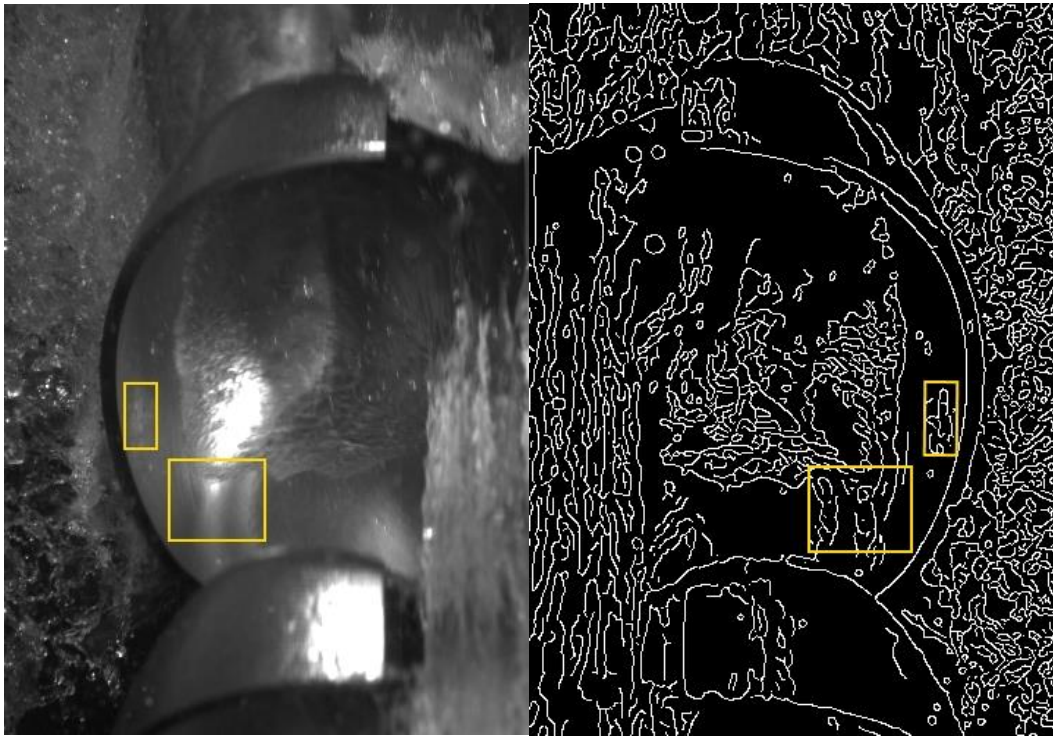


Figure 6.4: Edge detection, using the Canny method in a) on b). Disturbance regions are put in boxes.

The right hand side of Figure 6.4 shows a random image taken from the film for a nozzle opening of 4 mm and $n_{11}=44$. The result of using the edge tracing algorithm based on the Canny method, as described in Chapter 6, for that left hand side image, is shown at the right hand side of Figure 6.4. Again, the left hand side image is mirrored to ease the comparison. As seen, the Canny method does well in detecting the clear and distinct edges in the image. However, when it comes to tracing the waterfront propagating inside the bucket, some problems arise. First of all, reflection from the external illumination of the bucket contributes with its own pixel gradients where this takes place. As a result, the edge detector algorithm recognizes these areas and mixes the edges of reflection areas with those of the waterfront. The large yellow box in Figure 6.4 show an example of an area where the algorithm fails to detect the waterfront, as it blends with the area of reflection. The small yellow box also indicates an area of a little reflection. However, as long as the waterfront keeps away from such areas, those kind of small areas could be discarded as noise by the algorithm. Another problem faced regarding waterfront tracing is that part of the waterfront falls into the shadow of both the jet, the inside of the bucket region next to the cut-out edges, and for later frames, the succeeding the bucket. Thus, with this placement of the camera, only parts of the waterfront are visible.

6.3.5 Waterfront propagation: manual edge tracing

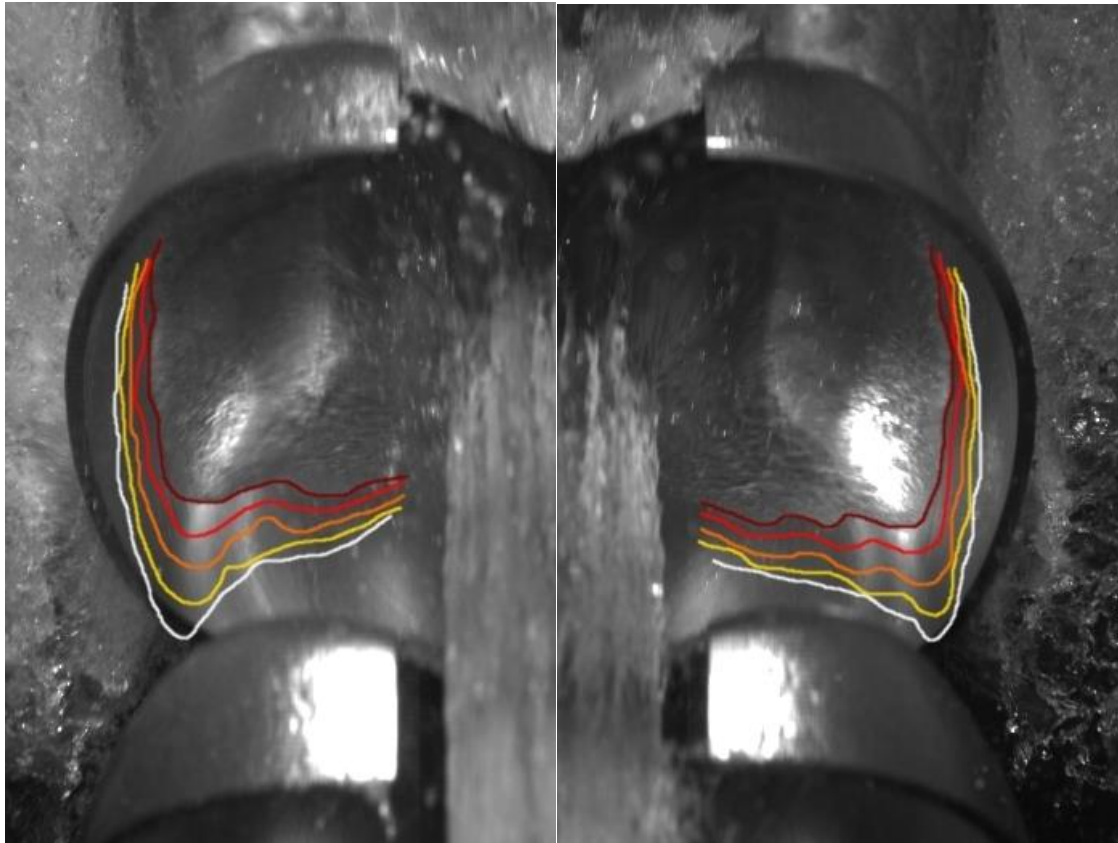


Figure 6.5: Waterfront propagation. a) 4mm, $n_{11}=39$, b) 4mm, $n_{11}=44$

The waterfront propagation was also investigated by means of visual detection, and manual drawing. Succeeding images from films were put on top of each other, and the waterfront was traced. The left hand side of Figure 6.5 shows a mirrored image of the waterfront propagation for five succeeding frames in a right bucket half, at a nozzle opening of 4 mm and $n_{11}=39$. The right hand side shows the case for $n_{11}=44$, with the same nozzle opening. The frame having the first occurrence of outflow forms a basis for comparison, and its waterfront is in both cases indicated by the white line. To allow for that basis, the two images are a bit shifted from each other. One can see how the two waterfronts propagate through the bucket towards the points of first outflow occurrences. It is apparent that the middle part of the water sheet is travelling a longer distance over the same amount of frames for the case having the lowest runner speed, as the distances between the waterfront lines are largest when $n_{11}=39$. This is in accordance with theory, as the relative outflow speed, w_2 , decreases with increasing runner speed, u_2 .

Considering the shapes of the waterfronts, both images show a tendency of a wavy waterfront (red lines) flattening towards a straighter waterfront (white lines). The reason behind the waves can possibly be explained by a combination of several factors, like that different part of the jet meet different bucket gradients, an uneven jet cross-section or a misaligned jet velocity profile. However, the steep gradients at both the outer edges and at the root force the waterfront to move towards the same point, as indicated by the white lines, thus flattening the waterfront.

The shapes of the waterfronts also differ from one another. It seems like more of the water in the right hand image has direction towards the root of the bucket, then for the left side, image when comparing the change of waterfront from the red to the white line. This may explain the higher efficiency for the case at the left hand image.

6.4 SUMMARY

Several post-processing tools were used for comparison of two flows at operating conditions of $H=30$ m, nozzle opening of 4 mm and runner speeds of respectively $n_{11}=39$ and $n_{11}=44$. The difference in the hydraulic efficiency was 1.7 %, in favor of the case of $n_{11}=39$. The image processing methods were able to qualitatively show that the reason for the better performance for the case of $n_{11}=39$ may be explained by less cut-out leakage and a more optimal bucket design for those relative velocities, leading to a more favorable direction and shape of the waterfront. Although more back wash was obtained for the said case, apparently its contribution to the loss was of less importance. However, no found available image processing tools were able to quantify these phenomena. An edge tracing algorithm based on the Canny edge detector failed to distinguish the waterfront from areas of reflection. Thus, in order to quantitatively measure the velocity profile of the water sheet, the waterfront propagation, together with the different phenomena's contributions to the total loss, modifications of the original experimental setup are necessary.

6.5 OTHER AREAS OF APPLICATION

6.5.1 Localization of the jet

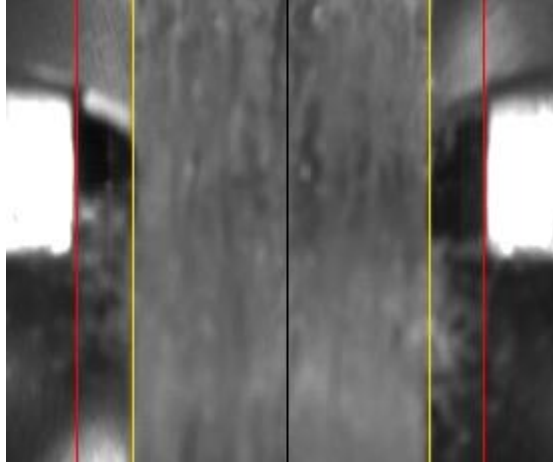


Figure 6.6: 4 mm nozzle opening, $n_{11}=44$. Edges of the cut-out are indicated by red lines, and the jet by yellow lines. The black line in the middle indicates the splitter location.

Edge detection can also be used to locate the jet. The width of the cut-out, W_l , is 37.9 mm, which corresponds to 204 pixels in Figure 6.6. Thus, the size in each direction of the quadratic pixels in the image are $37.9/204 \approx 0.186$ mm/pixel. Hence, the jet diameter is measured to 27.2 mm, with 14.1 mm and 13.1 mm on the right and left sides of the splitter, respectively. This correspond to a jet displacement relative to the jet diameter of 1.8 % to the left. The difference in jet area interacting with each side of the bucket is calculated to 52.3 % for the left bucket side and 47.7 % for the right bucket side, relative to the jet diameter. Assuming the water density of the jet is equal across the jet cross-section, although this is just an approximation due to jet outburst as well as a translation of the jet velocity profile impinging the bucket; these numbers can be approximated as relative bucket loads.

6.5.2 Camera alignment

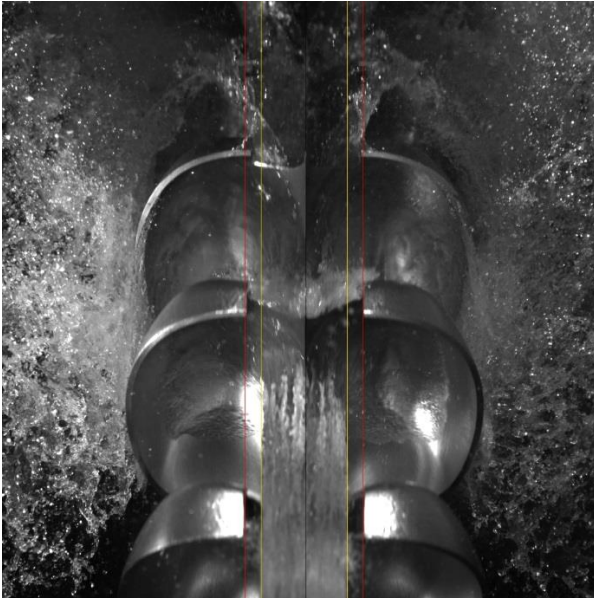


Figure 6.7 a): Misalignment of the camera relative to the turbine. The lines are vertical, showing a slight displacement in the upper left lip edge.

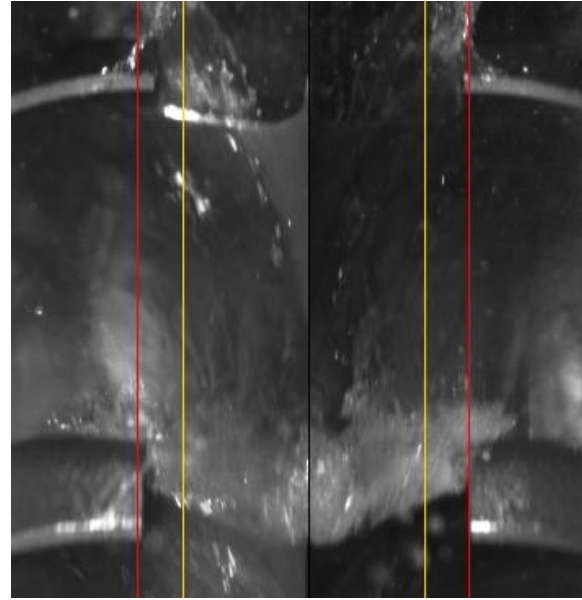


Figure 6.8: b) The hindmost part of the image

Edge detection can also be used to align the camera position according to the turbine. The same edge detection method was used for this purpose, as was used in calculating the alignment of the jet relative to the cut-out. A slight misalignment of the camera is observed. All colored lines have 90 degrees angle with the bottom horizontal line. Figure 6.8 shows the hindmost part of the visualized part of the turbine. One can observe the vertical red line crossing the left edges of the two cut-outs in the image, indicating that the camera is tilted slightly to the right, relative to the runner. By rotating the same original image in MATLAB and repeating the edge detection, the tilt of the camera was found to be 0.3 degrees in the clockwise direction.

7 POSSIBLE IMPROVEMENTS TO THE ORIGINAL SETUP

The original experimental setup allows for detailed filming of the flow inside a Pelton bucket to some extent. However, as experienced during post-processing of the films, there is a potential for improvements, to get even clearer, more detailed and close-up images, with less amount of disturbances. Moreover, some improvements are necessary in order to be able to analyze the flow quantitatively. In this chapter, possible areas for improvements to the original experimental setup are presented.

7.1 BUCKET

7.1.1 Surface treatment

As experienced during the image processing, the great extent of reflection of light in the buckets made it difficult to trace the waterfront, using edge detection methods. A possible solution is to treat the bucket surface of the bucket of interest, by changing its color or making it matt, to hinder reflection.

7.1.2 Marking the inside of the bucket

To analyze the waterfront in the bucket quantitatively, some kind of marking is needed, to specify the positions accurately in three dimensions. A set of marks with known coordinates will also allow for measurement of the water-film thickness, as described by Perrig [1]. Since the bucket-coordinates are known, and to be found in the CAD-drawing, the only requirement for marking is to transfer these from the drawing to marks on the bucket as accurately as possible.

Two types of marking are considered: a complete grid with crossing lines, and only a certain number of dots. One advantage of having a complete grid is that it gives a good set of reference points for flow visualization, and at the same time opens for measuring the water-film thickness the same way as Perrig [1]. However, when using a gradient-based edge tracing method for post processing of images, it may be difficult to track the waterfront when passing a gridline. The contrasts may blend, as in the case of reflection in the bucket. There are several ways of doing the marking itself. One solution is to make a stencil that perfectly fits the inside of the bucket, and then paint on it. In that case, it would be easier to choose to have only a certain number of dots, as a 3D-printed stencil of a detailed mesh would be difficult to obtain. On the other hand, it is possible to mark directly on the bucket; either with a pen, although not a very accurate method, or with a laser.

7.2 CAMERA SETUP

One of the major drawbacks of the original experimental setup is that one can only observe parts of the bucket duty cycle. Since the bucket duty cycle takes about 90 degrees to complete [1], the bucket of interest filmed by one still camera will at some point come in the shadow of the succeeding bucket, regardless of placement of the camera. Hence, to cover the entire duty cycle one can film separate parts of the cycle and then change the camera position. One can also use a visualization system that is able to rotate together with the bucket of interest.

Other aspects to consider to get more out of the flow visualization, are related to the image quality. For example, as seen in Figure 6.1, the large distance between the camera lens and the moving buckets results in disturbances on the image, concerning fog and larger water droplets.

One solution could be to build an extension of the lens, for example with an endoscope, and place it close to the area of interest. Another solution is to place the camera itself inside the casing, closer the turbine. However, no matter how close the camera gets to the turbine, still water will come between the lens and the buckets. Moreover, placing the camera inside the turbine casing makes it harder to prevent water from sticking to the lens. Because of the curved nature of the bucket design, it is impossible to visualize all areas inside a bucket at the same time when the camera, or endoscope, is fixed outside the runner. The jet will cover some regions as well.

Placing an endoscope on the runner itself, like an experimental setup similar to that of the onboard borescope setup by Perrig [1], offers a solution to the option of a rotating visualization system. One will be able to see the entire bucket cycle, and the area of observation will only be limited to the angle of vision out from the borescope lens, not obstructed by the jet nor by the curved bucket outline. Because of centrifugal forces, it is unlikely that water droplets will stick on the lens of the borescope, when placed like that of Perrig [1].

However, a camera setup based on an onboard borescope, requires more light to the area of investigation. Furthermore, the system includes optical parts that rotates at hundreds of revolutions per minute, as is vulnerable to damage. It takes much time for each practitioner to learn how to set up and use, and introduces more needs for post-processing, as the borescope lens is of the fish-eye type. Of course, there will also be an issue of costs.

7.3 LIGHTING

For larger volume flows, in particular at low rotational speeds, the outflow from the buckets blocks out the light from the external light sources. The less amount of light reaching the area of investigation goes at the expense of the camera shutter speed, and thus image quality.

In the case of a setup based on an onboard borescope, the amount of light that reaches the camera is even less than that of the original setup. This puts an even higher demand on the illumination intensity. Furthermore, since a setup using borescope opens up for visualization of the entire bucket duty cycle, different light sources should be placed at several locations around the turbine to make this possible. The light sources should be situated in such a manner that all angular positions of the bucket of investigation potentially get equal amount of light. One possible solution is to install a set of waterproof flash lamps inside the turbine casing. Although, a challenge for the flash lamps will be to provide enough power. Another solution is illumination by means of a laser.

8 IMPLEMENTING IMPROVEMENTS TO THE SETUP

This chapter presents the processes of choosing and designing the preferred solutions to improvements, on basis of the discussion in Chapter 7.

8.1 BUCKET

8.1.1 Surface treatment

To be able to choose the right form of surface treatment to the bucket to avoid the most reflection of light, a process of testing the effect of different surface treatments was carried out.

8.1.1.1 Method of investigation

For convenience, the tests were conducted in a sink in the Waterpower Laboratory, having water running over the bucket. The same lamps as in the original experimental setup were used, and the buckets were all fixed in the same position in the sink, aiming for approximately similar lighting conditions as in the original experimental setup. The same camera as used for the original experimental setup was then used to film the bucket. However, the comparison was only relative between the different buckets of interest, so the most important thing was to keep the lighting conditions similar for all tested surface treatments.

The original buckets on the turbine of Solemslie were made of anodized aluminum. Lacquers available in the Laboratory having different colors, both shiny and matte, were sprayed on test buckets made of aluminum, similar to the basis of the bucket on the turbine of Solemslie. Afterwards, a chemical approach of treating the surface was tried on the bucket of Solemslie. A strong alkaline detergent, called "HD-vask", consisting of potassium hydroxide and several phosphates, were poured over the bucket. As a result of the chemical reaction taken place, a small layer of aluminum oxide was evident on the bucket, creating a matte film. This process of filling the bucket with detergent and wiping it off could be repeated several times, making the bucket surface more matte for each time. The last method used was sandblasting. An olivine type of sand (GL 60, Biltema), with average grain diameter of 0.34 mm and hardness of 6.5-8 Mohs, was used.

8.1.1.2 Results

It was clear that the buckets having white, or beige, surface gave larger reflection than the original aluminum bucket. On the other hand, the bucket covered with black lacquer gave less gleam than the original bucket, even though the lacquers was shiny. However, the black surface absorbed so much light that the frame rate on the camera had to be turned down to 250 fps, to get satisfactory brightness on the image. Thus, with current lighting available, this seemed like a major drawback. A gray colored, matte lacquer served as a compromise, giving the best results among the lacquers tested. The chemical method with detergent gave an even better result, allowing for adjusting the dullness by choosing the number of small oxide-

layers. However, when repeating the process many times it was hard to control the resulted thicknesses of the layers, resulting in a slight change of bucket geometry, of unknown manner. Nevertheless, the visual the effect of sandblasting was by far the best, giving a complete matte surface. A drawback of sandblasting was that the surface became somewhat rougher, although the visible rings inside the bucket from the machining process were still visible after the sandblasting. However, the small change in the surface roughness is considered negligible in the context of the high velocity and turbulent nature of the water running through the bucket. The results from the testing are summed up in Table 8.1 and the visual effect on reflection of sandblasting the bucket of Solemslie is illustrated in **Error! Reference source not found.** The images are taken of the right bucket half at the same operating conditions. The left hand side of the image is mirrored to ease the comparison. Although the focus of the camera was not very good, the reduced reflection of light in the right hand side image is evident.

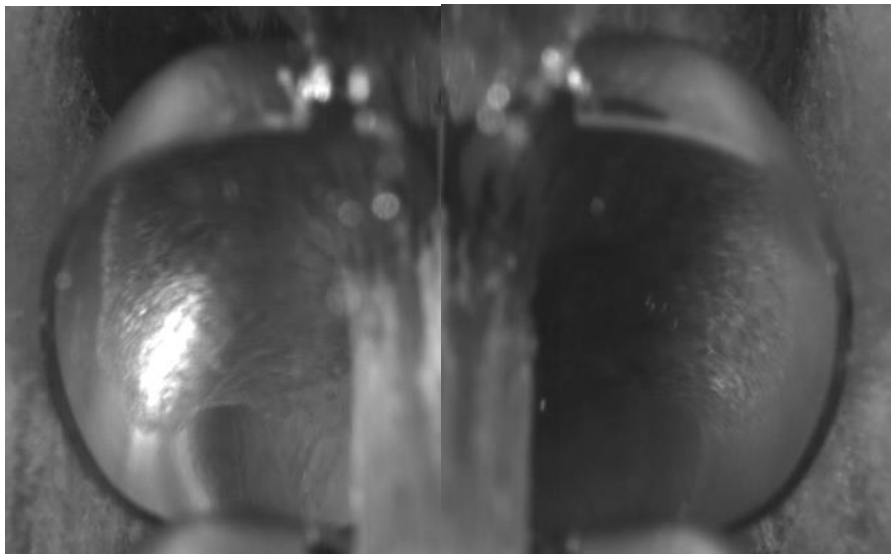


Figure 8.1: Visual effect on reflection of sandblasting a bucket of the turbine of Solemslie

Table 8.1: Summary of the effects of surface treatments

Surface treatment	Apparent reflection relative to that of the original bucket coating	Drawback
Black, shiny lacquer	Less	Much light needed
Red, shiny lacquer	Same	-
White, matte lacquer	More	-
Grey, matte lacquer	A little less	-
Chemical treatment	Less	Change of geometry

Sandblasting |

A lot less

| Rougher surface

8.1.2 Marking the inside of the bucket

Concerning the choice between marking the bucket inside with a complete grid with crossing lines or only dots, both alternatives were considered.

For the latter alternative, the number of dots, or markings, had to be enough so that an image of the bucket with no water in it could be perfectly aligned with the corresponding CAD-image with known coordinates. To make a set of solvable equations for this alignment process in MATLAB, 15 dots were found to be sufficient. Since the coordinates are known in every pixel of the image, the apparent displacement angle, α , can be calculated directly from the image, knowing the accurate location of the distal lens, and hence the distances to it. Thus, direct water-film thickness measurement is possible for this reference system, without the need of making a new reference system like that of Perrig [1].

However, the first alternative of marking the bucket, using an entire grid, was also considered. Furthermore, it is easy to erase and change the markings, if not satisfied. Consequently, a random first choice fell on a complete grid. Figure 8.2 shows an image in the process of making the grid in the bucket manually, on a sandblasted version of a bucket of Solemslie. Although this may not be the most accurate method, it was only thought of as a first test. The thickness of the pen used was originally 0.5 mm. However, due to hard use, some resulting lines were almost as thick as 0.8 mm. The distance between each line at the end was 5 mm.

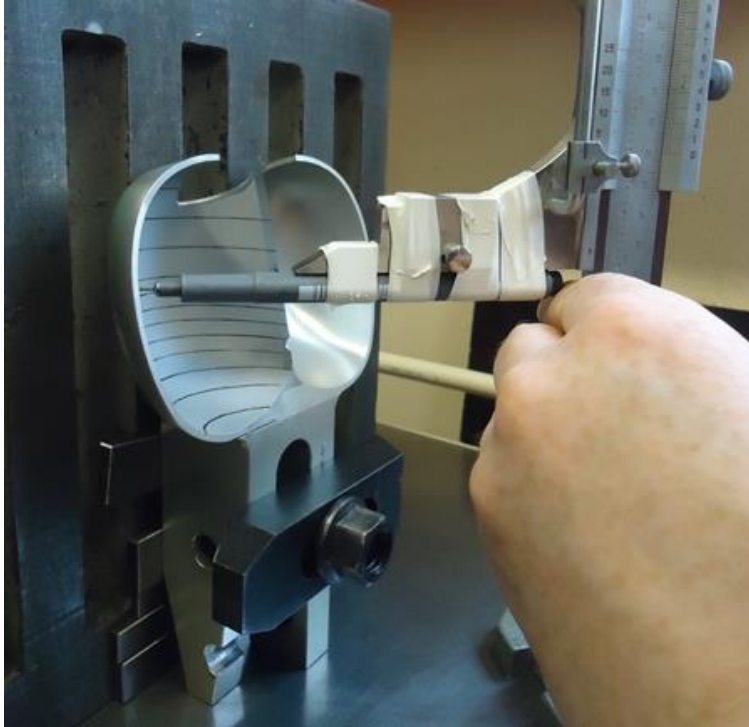


Figure 8.2: Making a grid in the bucket manually

8.2 CAMERA SETUP

The choice of improvement to the camera setup fell on a setup based on an onboard borescope, based on the same principles as that of Perrig [1]. The advantages of such a setup were considered superior to the drawbacks, as it represents a possible major improvement to the experimental setup if working properly.

8.2.1 Optical system

Using CAD modeling in Creo Parametric, an optical arrangement was designed, as shown in Figure 8.3. The borescope itself was embedded in one bucket, visualizing the inside of the adjacent bucket. The estimated region of the bucket of interest made visible through the borescope is illustrated in Figure 8.4. Due to the limited field of view of the borescope and limited ways of embedding the borescope inside one bucket, the visible region in Figure 8.4 was considered best possible, although some part of the bucket fell out of the image. After several design iterations, a custom-made borescope was produced by Henke-Sass, Wolf, to perfectly fit the runner of Solemslie. Additionally, a 90° angular adapter of 600 mm was chosen to connect the rotating borescope with the stationary camera. A camera lens adapter and a magnifier adapter to double the size of the obtained image, both stationary parts of the system, were also acquired. Figure 8.5 and Figure 8.7 show the optical parts, while Figure 8.6 show the acquired borescope.

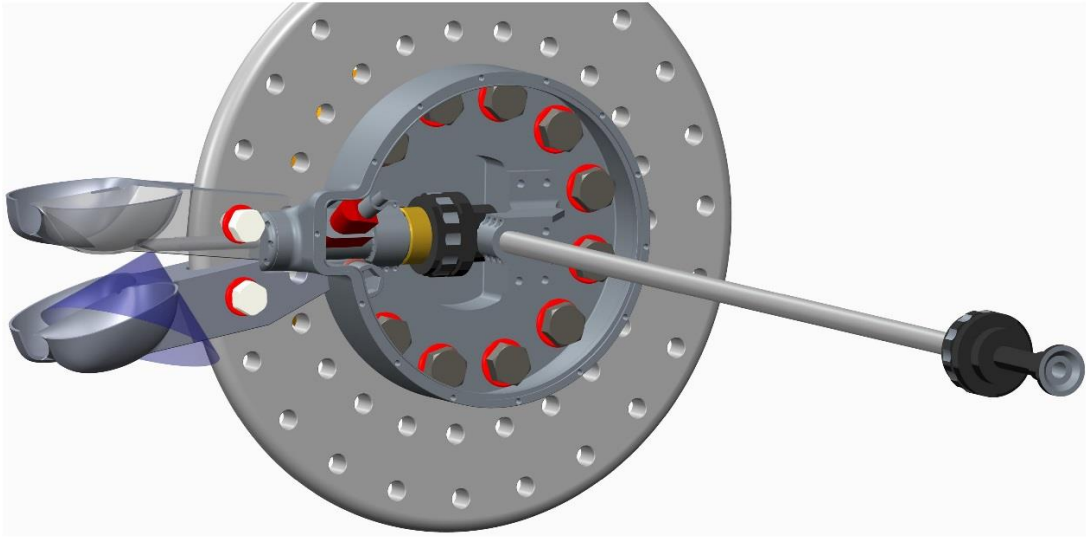


Figure 8.3: CAD-drawing from the design process, illustrating the desired setup

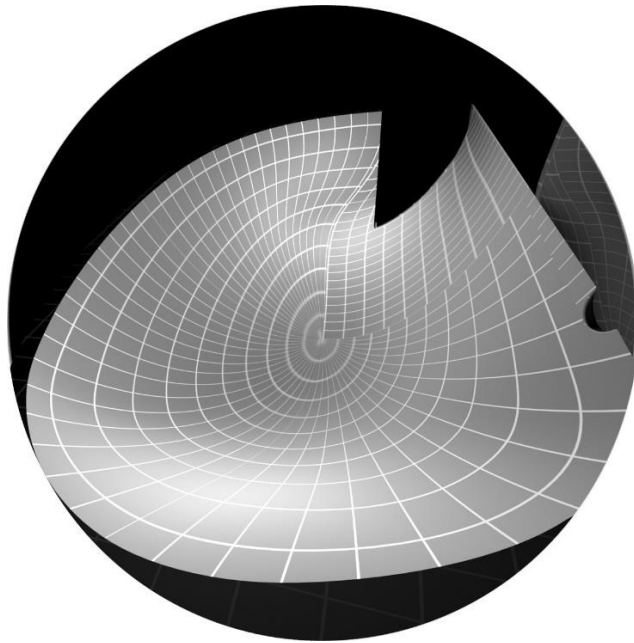


Figure 8.4: CAD-drawing from the design process, illustrating the resulting visible area seen through the borescope, as of Figure 8.3.



Figure 8.5: The optical system is split in a rotating and a stationary section

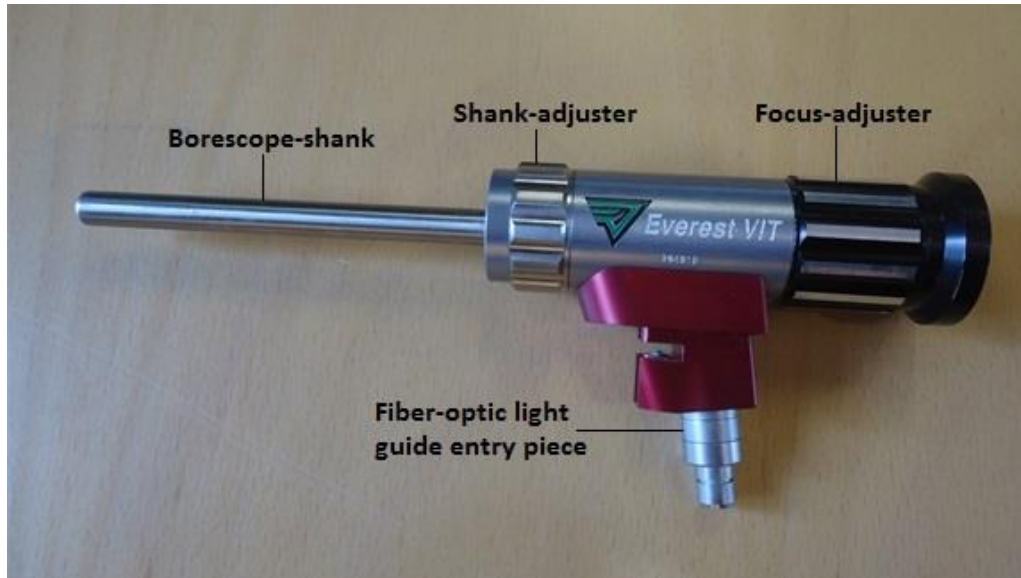


Figure 8.6: The borescope

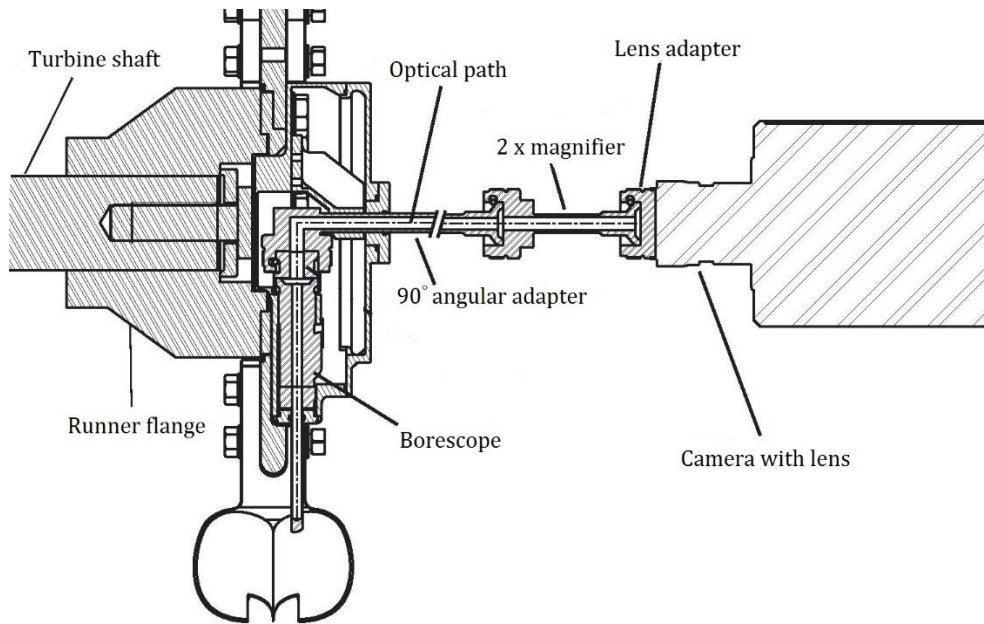


Figure 8.7: Schematic of the optical system

8.2.2 Support system

A solid supporting system was designed and acquired for the optical system and the camera, as illustrated in Figure 8.8. The frame of the system was made by aluminum profiles from the MB Building System, with dimensions of 80x80 mm. In the addition to the framework, the supporting system consists of a needle roller bearing and casings. The supporting framework is to be mounted to the turbine casing as a whole, lifted up from the floor. This has to be done in order to minimize the differences between the vibrations in the turbine casing and the camera, standing on the support. The framework is made to be adjusted in both the vertical and horizontal direction. Moreover, the bearing casing and camera support can be adjusted separately. This is done to be able to adjust the camera to be aligned with the 90° angular adapter, and to accommodate for the use of different cameras.

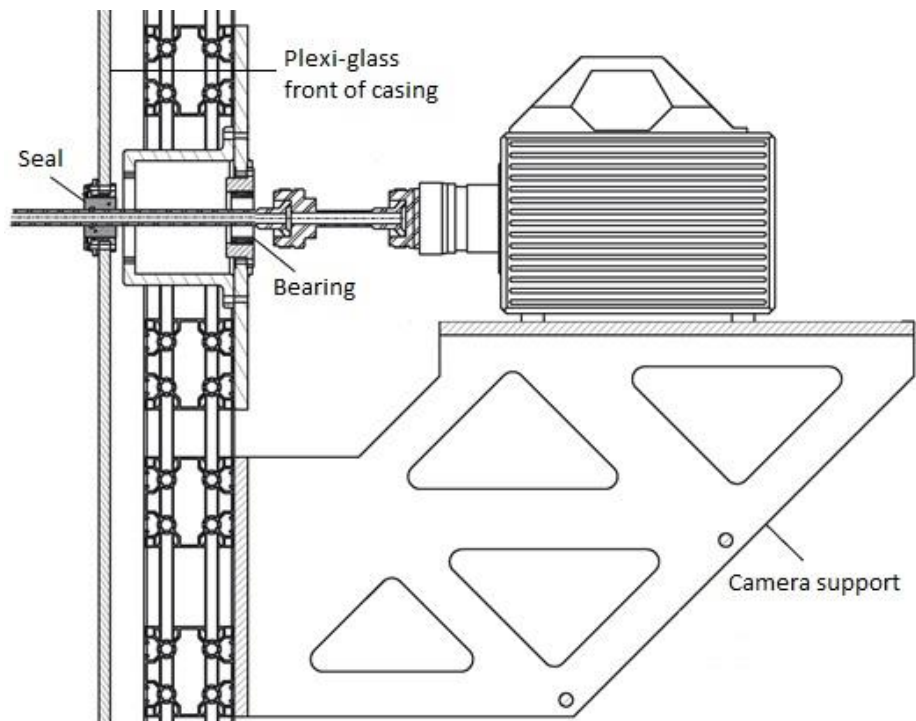


Figure 8.8: Schematic of the supporting system

8.3 LIGHTING

An Oxford Laser's Vapor Copper Laser LS 20-10 was already acquired and available at the Waterpower Laboratory at NTNU. Thus, the choice of lighting setup improvement fell on a setup being based on that laser. This laser has the possibility to be controlled by a pulsating trigger, giving a pulsating laser beam. This way, the laser can be synchronized with the camera, and hence be controlled by the position of the bucket. In such a way the laser will function as a blitz for the camera.

The laser was tested and found to have a nominal output of 19 W when the laser beam was pulsating at 10 kHz. The pulse duration of the laser is 25-30 ns. Assuming a scenario with a duration of 30 ns, the peak power at each "blitz" of laser light can then be approximated to be over 60 kW. The laser beam can be split into several beams by reflection. The laser beams can then be directed through optical fiber cables, and placed inside the turbine casing wherever desirable. Hence, several light sources can be placed anywhere suited for the requirements of covering the entire bucket duty cycle, with all bucket positions getting equal amount of light, as well as avoiding the shadowing from the water outflow. Although a splitting of the laser beam would lead to some losses in the effect output, this is not assumed to be of major concern.

Another advantage of using a laser as a light source is the short pulse duration of the light. This allows for capturing sudden changes, as well as details, in the images [25]. Since the minimum shutter speed of the camera is 1 μ s, and thus 40 times longer than the laser pulse duration, this place high demands on the coverage of the area towards the intake of light from the surroundings. However, covering the area around the casing properly with a light absorbing fabric will make the area dark. Besides, a complete coverage of the rig is necessary considering HSE issues concerning the light emission from the laser.

Another alternative for lighting setup was also made, in case the laser setup would not work as expected. A new window made of Plexi-glass was cut out and put in the casing just over the inlet pipe to the nozzle. This permits a new location for one lamp, where the shadowing from the bucket outflow is much less than for the location for the global lighting at the original setup.

9 NEW EXPERIMENTAL SETUP

This chapter describes the resulting experimental setup after the earlier discussed improvements were installed on the Pelton test rig.

9.1 GENERAL DESCRIPTION

A new experimental setup has been installed for high-speed visualization, using an onboard borescope. A lighting setup by means of a laser has been implemented, and the bucket of interest has been modified with a sandblasted surface and associated grid. The laser is synchronized with, and triggered by, the camera, and the recordings are controlled in the control room on a laptop by the camera software, FastCam Viewer. The camera used is the same as for the original setup.

A thorough and detailed procedure of how to assemble and use the new experimental setup has been made. Because of its length, it has been put in Appendix A.



Figure 9.1: Installed new setup, with an onboard borescope

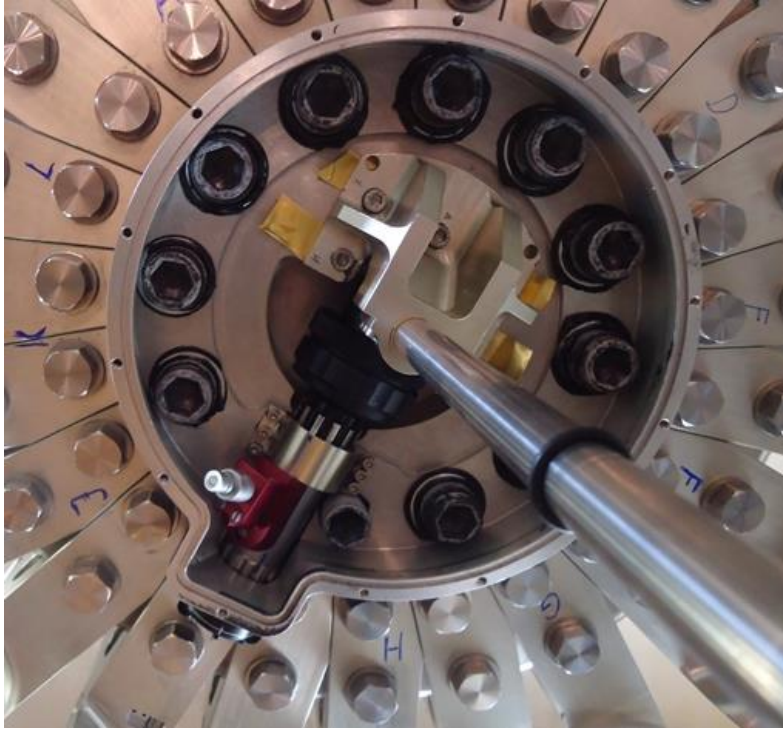


Figure 9.2: Close-up of the inside of the borescope casing

9.2 ILLUMINATION BY MEANS OF A LASER

As a start, the laser was implemented for the Pelton test rig with one optical fiber situated just over the nozzle exit, as shown in Figure 9.4. The lighting setup is shown in Figure 9.3. A thorough procedure of how to run this specific laser was also made, and is to be found together with the risk assessment report, given in Appendix B.

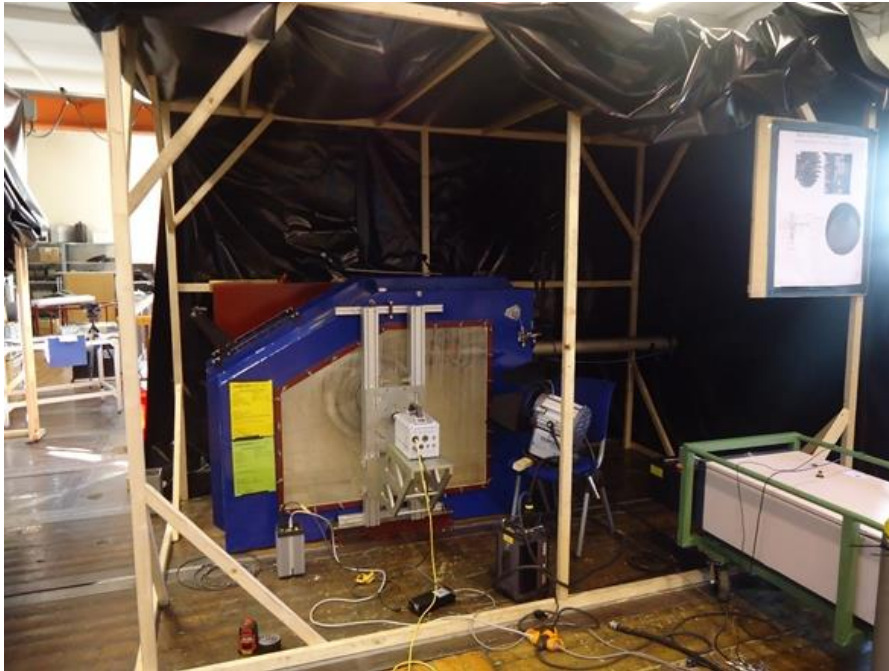


Figure 9.3: Complete installation, with the laser for lighting placed to the right. The other light sources are only used during installation



Figure 9.4: One optical fiber-cable for laser light placed inside a metal pipe, situated just over the nozzle exit.

9.3 ILLUMINATION BY LAMPS

Unfortunately, the laser did not work when the tests of the new setup were supposed to be carried out, and time did not allow for further testing. Instead, a test of the setup was run with light provided by the same lamps as used for the original experimental setup. The lamps from the original setup was used. The Dedolight lamp was placed on a tripod, as illustrated in Figure 9.5. The Fresnell lamp was used as global lighting source.



Figure 9.5: Experimental setup with lighting from lamps

At first, many tests were carried out where the positions of the lamps were varied greatly. This was done to find the optimal positions of the two lamps. Then, the sensitiveness of the lighting positioning was investigated further, by changing the location of the Dedolight light on the tripod by only a couple of centimeters. Three tests of the experimental setup were carried out, when these small changes of the lighting source position were made.

The frame rate used on the camera was 500 fps, the shutter speed 0.002 s, and the speed of the runner was 400 rpm. The resulting films were saved with an MRAW-format, allowing to process them later by changing the bit shift in FastCam Viewer. The resulting frames on the films were rotated using MATLAB, to orientate them in the same direction.

In addition, a still picture was taken of the bucket, as seen through the borescope, to investigate the maximum obtainable image quality for a lighting setup by means of lamps.

10 RESULTS FROM THE NEW SETUP

This chapter presents and discusses the results from the new experimental setup, with illumination by means of lamps.

10.1 STILL PICTURE

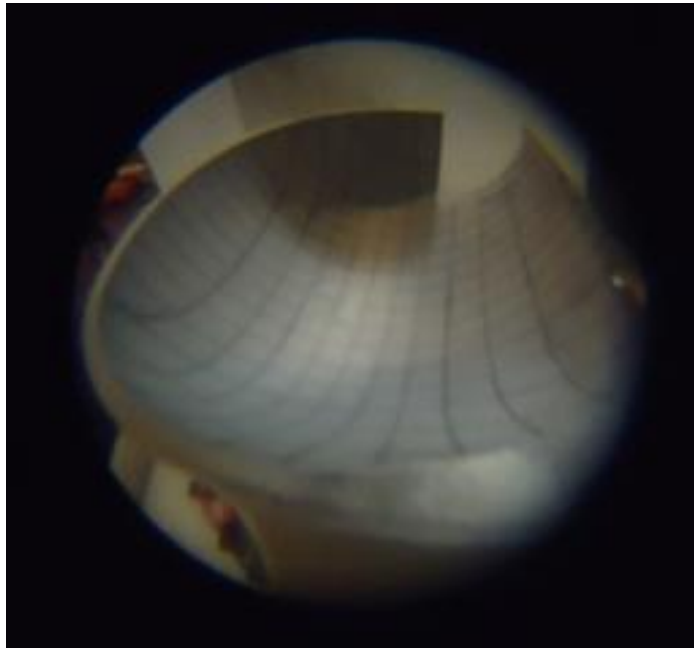


Figure 10.1: Visible region seen through the borescope, when no water in the system

Figure 10.1 shows a still picture of the bucket, as seen through the borescope. It shows that the entire inner part of the bucket half of interest is visible. However, the sharp edges of the circle surrounding the visible image get blurry in the lower right corner. This is due to a slight misalignment between the borescope and the 90° angular adapter. Beyond that, except from a shadowy part near the outer cut-out edge due to the direction of light, almost the entire grid is visible and somewhat clear. This means that the adjustment of the focus on the borescope has been done right.

10.2 HIGH-SPEED FLOW VISUALIZATION

Figure 10.2, Figure 10.3 and Figure 10.4 show a frame taken at the same bucket position, just after the start of the feeding process. However, the position of the Dedolight lamp for local lighting has been slightly changed between each test. The images are rotated so one sees the bucket from the root. There are large differences between the images concerning the brightness. One can see how the amount of reflection from the light differs between the images. For the cases with less brightness, a larger bit shift was executed on the image to highlight the light bits, as a compensation. However, this lead to a poorer quality of the image, as exemplified by Figure 10.4. In addition, the amount of visible reflection got bigger, suppressing the effect of the sandblasting of the bucket. Evidently, different details revealed in the images are highly dependent on the positioning of the light source.

Figure 10.2 turned out to have the best positioning of light sources, revealing the most details, and will thus be discussed further. At the upmost right corner one can see the water jet coming through the cut-out, interacting with the bucket. Along the right side of the image, it may look like there is some kind of fog. However, the probable reason is the relatively long shutter speed, as the water in the bucket changes its position while recording. The shown image was the frame being exposed to the most light during that given recording, thus having the most detailed image. Hopefully, illumination from laser will provide better lighting conditions, and thus more bucket frames will be visible. In addition, the short pulse duration of the laser of 30 ns will reduce the effective shutter speed drastically, leading to clearer images with more details.

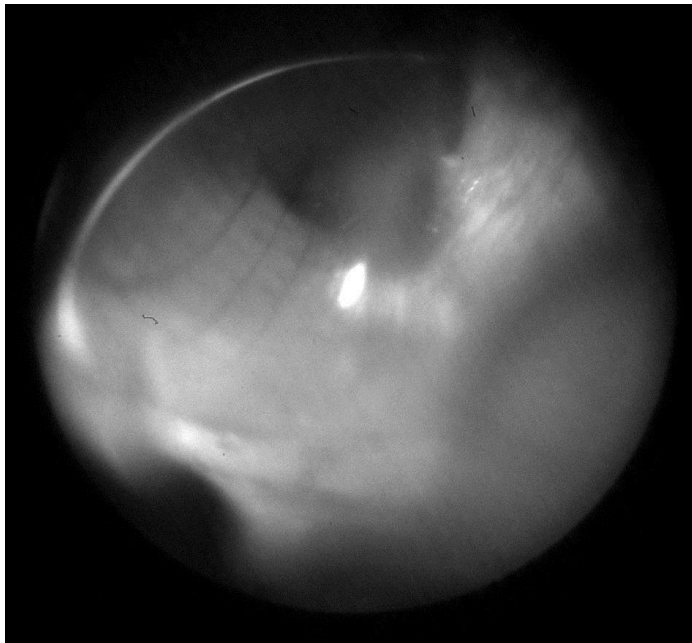


Figure 10.2: Test with water for the old lighting setup, test 1

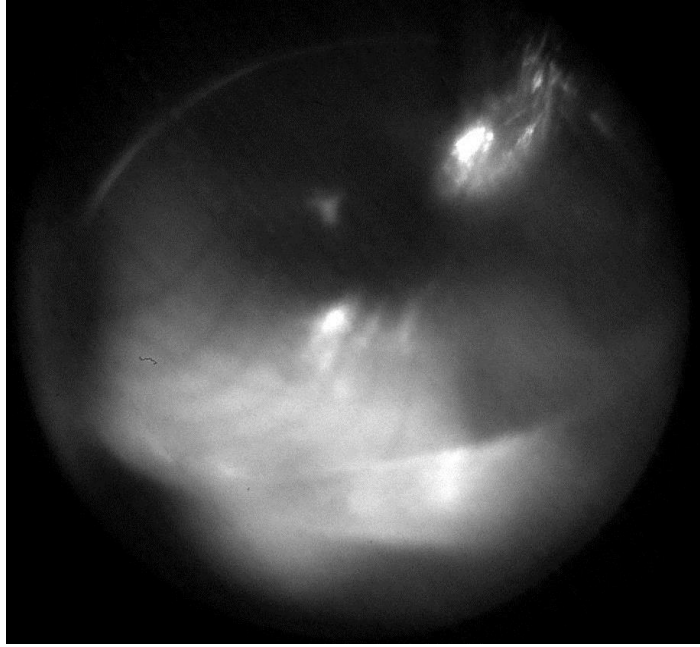


Figure 10.3: Test with water 2

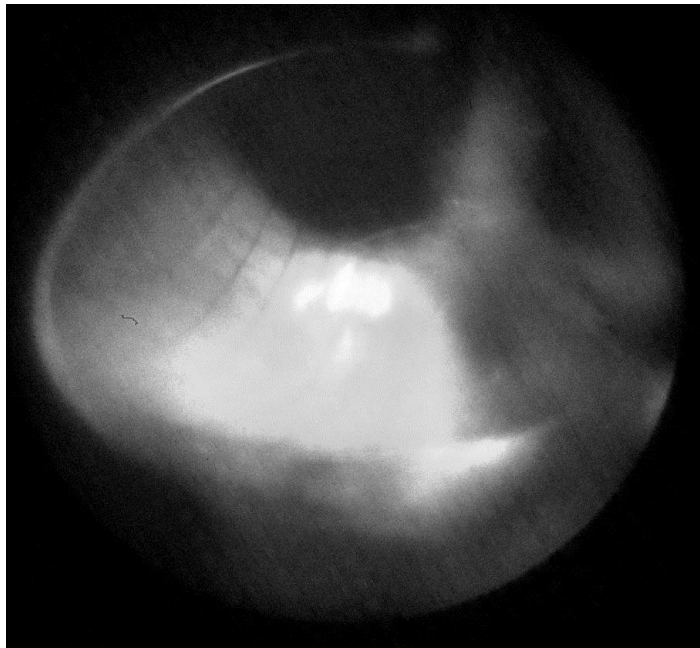


Figure 10.4: Test with water 3

11 EVALUATION

This chapter presents a summary of the thesis as a whole, with particular focus on the evaluation of the improvements made on the experimental setup. An evaluation of the goals, stated in the introduction of the thesis, is given.

11.1 EVALUATION OF THE IMPROVEMENTS ON THE SETUP

Unfortunately, the laser did not work when the tests were supposed to be undertaken. Consequently, the final outcome of all improvements done to the setup was not possible to evaluate. However, filming with the new setup, only with the old light settings, has been performed successfully. The need of a better lighting setup, like one by means of a laser, was demonstrated. Also, the sensitiveness to the placement of the light sources, regarding the amount of light reaching the camera, was found to be great. The camera setup with the onboard borescope was tested for high runner speeds, and worked successfully. No contact was obtained during experiments at the transition between the stationary and rotating optical parts, which was a point of critical character. Moreover, the obtained image gave a visible segment of the bucket that was even larger than expected, as seen by comparing Figure 8.4 and Figure 10.1. Considering the modifications made on the bucket itself, the grid turned out to be helpful when orientating the image, for the cases where no other reference lines were visible. Both the grid and the surface treatment of the bucket were meant to improve the image post-processing for further analysis. Because of the less available light due to the broken laser, and thus less clear images, post-processing the images was impossible. However, the goal of building a visualization system that enabled close-up images of the whole bucket half, throughout the entire bucket duty cycle, was accomplished. As soon as the laser gets fixed, one will be able to discuss whether the new setup needs more modifications to meet the requirements of image quality.

If there for some reason should be a need to return to the original experimental setup, the camera and light sources can easily be placed back to their old positions.

11.2 IMAGE PROCESSING

Few available, free image processing tools were found, except from the different edge detection algorithms and the built-in functions in Image Processing Toolbox in MATLAB. Moreover, when using a built-in function for edge detection, like the Canny method, one needs to learn the code before use, since the way of localizing the edges differ from detector to detector and may cause slightly different results. Consequently, it may be smart to build one's own algorithm when performing a custom edge tracing. Anyhow, edge detection methods may have several areas of application. In addition to tracing the waterfront, and thus be able to calculate the velocity of the waterfront, edge detection can be used to orientate an image, to locate the jet position and to adjust the camera for tilting.

The films from the new setup require some additional image processing, in order to be analyzed quantitatively. First of all, since the borescope is rotating relative to the camera, the obtained images are rotated relative to each other. Knowing the rotational speed and camera frame rate, one can rotate the images back to the same position, using software like MATLAB. Furthermore, the lens of the borescope is of the fish-eye type. Thus, the images obtained from the high-speed filming need to be converted into normal perspectives. Moreover, the images show a bucket that is inclined relative to the CAD-image of the bucket with known geometry. Using the known grid locations in the bucket, one can transform the inclined images into ones that fit the CAD-image. Then, each pixel in an image can be given an X, Y and Z-coordinate, corresponding to the real bucket, and one can start to analyze the flow in the bucket quantitatively. Work is still in progress at the Waterpower Laboratory to make a complete algorithm in MATLAB, which perform all these operations.

12 CONCLUSION

The original experimental setup allowed for detailed flow visualization in a Pelton bucket to some extent. The bucket flow at two different operating conditions were compared with help of image processing, regarding back wash, cut-out leakage and waterfront propagation.

However, the flow analysis revealed several areas of the original setup with potential for improvements. To be able to analyze the flow quantitatively, the obtained images from the high-speed visualization had to be clearer, with less disturbances from reflection. In addition, a reference system had to be made inside the bucket, in order to transfer the coordinates from the CAD-drawing to the image. Furthermore, a new camera setup was recommended in order to get even more details out of the images, to show a larger part of the bucket, and to cover more of the bucket duty cycle.

Consequently, necessary improvements were made, and a new experimental setup based on an onboard borescope was designed and installed to meet the above-mentioned requirements. The new camera setup performed well, providing close-up images of one bucket half, throughout the entire bucket duty cycle. However, due to a dysfunctional laser, which was implemented to provide lighting, the total performance of the complete new experimental setup has yet to be tested. The positioning of light sources was also shown to be of great importance regarding the obtained image quality.

Considering the use of edge detection methods for quantitative analysis, like waterfront tracing, it is suggested that one should make a custom algorithm that is specially designed for the case of investigation, to minimize the uncertainties regarding the localized position of the edges. However, well known algorithms, like the Canny edge detector, may be used for inspiration. Edge detection methods have also shown to be useful for other applications, like to orientate an image, to locate the jet position or to adjust the camera for tilting.

13 FURTHER WORK

As discussed in the previous sections, there are still areas left for further investigation. First of all, to be able to evaluate the complete new experimental setup, the laser needs to be fixed. It is likely that minor adjustments of the setup needs to be done, after having analyzed the films from said setup. One area that probably will require adjustments is the positioning of the fiber-optic cables inside the turbine casing, when illuminating by means of the laser. There is also a possibility to distribute the available laser power into several refracted laser beams.

If reflection of light in the bucket continues to be a problem for the new setup, one potential solution could be to color the water. A tracer dye called Rhodamine B is one of the dyes actively used by geologists to color the water for tracing purposes, and is very soluble in water.

To enable quantitative analysis of the flow in the obtained films, several image-processing algorithms are required. This includes algorithms that perform the following, in consecutive order: transforming the fish-eye perspective obtained by the filming to a normal perspective; transforming the given image into one that fits the CAD-drawing of the bucket, based on the reference grid; distributing the bucket coordinates of the CAD-drawing to the pixels of the image. Bjørn W. Solemslie, at the Waterpower Laboratory, has already started the process of making these algorithms.

To perform quantitative analysis of the flow, like calculating the velocity profile of the waterfront in the bucket or measuring the water-film thickness, post processing algorithms specialized for those purposes have to be made. Clear images, without disturbances from light reflection, are also required.

To get a better understanding of the relative flow patterns in the bucket, one can trace particles that are added to the water.

REFERENCES

- [1] A. Perrig, "Hydrodynamics of the free surface flow in Pelton turbine buckets," École Polytechnique Fédérale de Lausanne, Lausanne, 2007.
- [2] B. W. Solemslie and O. G. Dahlhaug, "A reference pelton turbine - design and efficiency measurements," in *IOP Conference Series: Earth and Environmental Science*, 2014.
- [3] H. Christie, "Teoretisk undersøkelse av vandstraalens bevægelse over en peltonturbinskovl," NTNU, 1918.
- [4] M. Hana, "Numerical analysis of non-stationary free surface flow in a Pelton bucket," NTNU, 1999.
- [5] Z. Zhang, "Flow interactions in Pelton turbines and the hydraulic efficiency of the turbine system," *Journal of Power and Energy*, vol. 221, pp. 343-357, 2007.
- [6] A. Perrig, F. Avellan, J. Kueny, M. Farhat and E. Parkinson, "Flow in a Pelton Turbine Bucket: Numerical and Experimental Investigations," 2006.
- [7] A. Rossetti, G. Pavesi, G. Cavazzini, A. Santolin and G. Ardizzon, "Influence of the bucket geometry on the Pelton performance," *Journal of Power and Energy*, vol. 228, pp. 33-45, 2014.
- [8] B. Zoppé, C. Pellone, T. Maitre and P. Leroy, "Flow Analysis Inside a Pelton Turbine Bucket," *Journal of Turbomachinery*, vol. 128, pp. 500-511, 2006.
- [9] R. Lowy, "Efficiency analysis of Pelton wheels," *Trans. ASME*, vol. 66, pp. 527-537, 1944.
- [10] A. Perrig, M. Farhat and F. Avellan, "High speed flow visualisation of an impinging jet on a Pelton turbine bucket," in *Proceedings of 5th Joint ASME/JSME Fluids Engineering Conference*, 2007.
- [11] T. Staubli and H. P. Hauser, "Flow Visualization - A diagnosis Tool for Pelton turbines," in *IGHM 2004*, 2004.
- [12] S. Trefall, "Modelltester av Peltonturbiner ved Vannkraftlaboratoriet," NTNU, 2011.
- [13] M. Wessel, "Test av Peltonturbin i Vannkraftlaboratoriet," NTNU, Trondheim, 2014.
- [14] R. Maini and H. Aggarwal, "Study and comparison of various image edge detection techniques," *International journal of image processing (IJIP)*, vol. 3, pp. 1-11, 2009.

- [15] J. R. Parker, Algorithms for image processing and computer vision, John Wiley & Sons, 2010.
- [16] K. Pithadiya, C. Modi and J. Chauhan, "Selecting the most favorable Edge detection technique for Liquid Level Inspection in Bottles," *International Journal of Computer Information Systems and Industrial Management Applications (IJCSIM)*, vol. 3, pp. 34-44, 2011.
- [17] Trucco (Ch. 4) and Jain et. al (Ch. 5), "Edge detection (notes)," [Online]. Available: <http://www.cse.unr.edu/~bebis/CS791E/Notes/EdgeDetection.pdf>. [Accessed 15 06 2015].
- [18] A. T. Larsen, "Pelton turbine - Model test of a runner," NTNU, 2014.
- [19] H. Brekke, Grunnkurs i hydrauliske strømningsmaskiner, Trondheim: NTNU, 2000.
- [20] A. Kjølle, Vannkraftmaskiner, Trondheim: Universitetsforlaget, 1980.
- [21] H. Brekke, Pumper & turbiner, Trondheim: NTNU, 2003.
- [22] "IEC 60193: Hydraulic turbines, storage pumps and pump-turbines – Model acceptance tests," International Electrotechnical Commission, 1999.
- [23] D. Ziou and S. Tabbone, "Edge Detection Techniques - An Overview," *International Journal of Pattern Recognition and Image Analysis*, pp. 537-559, 1998.
- [24] K. Reinertsen, "Testtrigg for Peltonturbinmodeller ved Vannkraftlaboratoriet," NTNU, 2012.
- [25] Oxford Lasers Ltd., "Laser for High Speed Imaging," Oxford Lasers Ltd, [Online]. Available: <http://www.oxfordlasers.com/imaging/high-speed-imaging/>. [Accessed 7 6 2015].
- [26] "IEC 62097: Hydraulic machines, radial and axial – Performance conversion method from model to prototype.," International Electrotechnical Commission, 2009.
- [27] V. Hasmatuchi, S. Roth, F. Botero, F. Avellan and M. Farhat, "High-speed flow visualization in a pump-turbine under off-design operating conditions," in *IOP Conf. Ser.: Earth and Environmental Science (Vol. 12, No. 1, p. 012059)*, 2010.
- [28] B. W. Solemslie, "Optimalisering av ringledning," NTNU, 2010.

APPENDIX A – HIGH-SPEED VISUALIZATION PROCEDURE

A procedure for performing detailed high-speed flow visualization with an onboard borescope in a Pelton bucket

Written by

Audun Tufte Larsen

CONTENTS

- List of figures ii
- 1 Introduction..... 1
 - 1.1 Operational principle 1
 - 1.2 Facilities..... 1
 - 1.3 Procedure structure 1
- 2 Illustrations of the setup 3
- 3 Lighting setup 7
- 4 Assembling the borescope setup 9
 - 4.1 Balancing the runner 9
 - 4.2 Placing the borescope 11
 - 4.3 Placing the 90° angular adapter 12
 - 4.4 Balancing the 90° angular adapter 12
 - 4.5 Sealing and supporting..... 14
- 5 Preparations before filming..... 19
 - 5.1 Triggering the camera 19
 - 5.1.1 Option 1 – By use of the rotational speed measuring system..... 19
 - 5.1.2 Option 2 – Filming without triggering..... 19
 - 5.2 Choosing the right camera frame rate 19
 - 5.2.1 Option 1 – Ensure frames from different films are taken at the same positions..... 19
 - 5.2.2 Option 2 – Setting a frame rate of one’s own choice..... 19
 - 5.3 Synchronizing the camera with a laser 19
 - 5.4 Installing the lighting setup 20
- 6 Filming 21
- 7 Post-processing of film..... 21
- 8 References 22

LIST OF FIGURES

- Figure 1: Schematic of the supporting system..... 3
- Figure 2: Schematic of the optical system. The stationary part starts from the magnifier 3
- Figure 3: CAD-drawing from the design process, illustrating the desired setup..... 4
- Figure 4: CAD-drawing from the design process, illustrating the resulting visible area seen through the borescope, as of Figure 3..... 4
- Figure 5: Complete installation, with the laser for lighting placed to the right. The other light sources are only used during installation..... 6
- Figure 6: Inside the borescope casing, while balancing the shank of the 90° angular adapter 6
- Figure 7: Visible region seen through the borescope, when no water 6
- Figure 8: Fastening the lid for the borescope casing. White marks indicate the right position..... 9
- Figure 9: Shim distribution for runner balancing 10
- Figure 10: The placement of the borescope..... 11
- Figure 11: 90° angular adapter with base and clamp mounted 12
- Figure 12: Shim distribution for adapter balancing 13
- Figure 13: Fastening the cover of the borescope casing..... 14
- Figure 14: Sealing and guiding cylinders 14
- Figure 15: Final balancing of the 90° angular adapter 15
- Figure 16: Fastening the clamp to lay inside the bearing in the camera support 16
- Figure 17: Mounting the bearing outside the camera support 17
- Figure 18: Aligning the camera with the adapter, while fastening it to the support 17

2 INTRODUCTION

This procedure describes the entire process for implementation and use of a setup for high-speed flow visualization, using an onboard borescope on a Pelton runner at the Waterpower Laboratory at NTNU. Special attention is given to the assembly of the borescope and its connection to the camera, involving balancing of all rotating parts. The procedure is aimed for students or staff with little or no experience from similar tasks. It is written as part of the author's Master's thesis, where more information of the background for the chosen setup is to be found [1].

In the future, when more experience is gained from the installation process, and the test results gotten more numerous, it is of the author's desire that anyone with the interest will update and rewrite the procedure.

2.1 OPERATIONAL PRINCIPLE

In brief, when conducting high-speed visualization of the flow in a Pelton bucket, one aims to get the clearest and most detailed view of the flow as possible. A borescope is a rigid endoscope, and can work as an extension of the camera lens. For this setup, a borescope and its associated customized adapter, is mounted on the runner and rotates together with it. This makes it possible to get close-up images of the bucket. Illustrations of the operational principle are given in Chapter 3.

2.2 FACILITIES

There are several requirements that need to be considered to obtain sufficient image quality when filming. In essence, this involves using a camera of high standard and having sufficient light delivered to the bucket of investigation [1].

When writing this procedure, the camera in use was a Photron FastCam SA5, with associated software, called FastCam Viewer. An Oxford Laser's LS20-10 Copper Vapor Laser was used to empower optical fiber-cables, for lighting inside the turbine casing. All parts associated with the borescope were specially designed for the reference Pelton runner in use, made by Bjørn W. Solemslie [2]. Detailed specifications of the borescope may be found on the website of the manufacturer, Henke-Sass Wolf [3].

Although the procedure describes a setup based on the above-mentioned facilities, the intention has been to write a procedure that allows for changes of facilities. Thus, it has been made as general as possible.

2.3 PROCEDURE STRUCTURE

Chapter 3 gives an illustrative representation of the operating principle, and shows the schematic drawings of the setup. Chapter 4 is about the lighting setup. If a laser will be used as a lighting source, a cover for the rig must be build and optical fiber-cables placed inside the turbine casing, before assembling the borescope setup. Chapter 5 stands out as the core of the procedure, and provides a detailed recipe on how to assemble the borescope setup, with both stationary and rotating optical parts. Chapter 6-8 contain tips and recommendations for creating a best possible basis for further analysis of the flow in the Pelton bucket, based on image post-processing.

3 ILLUSTRATIONS OF THE SETUP

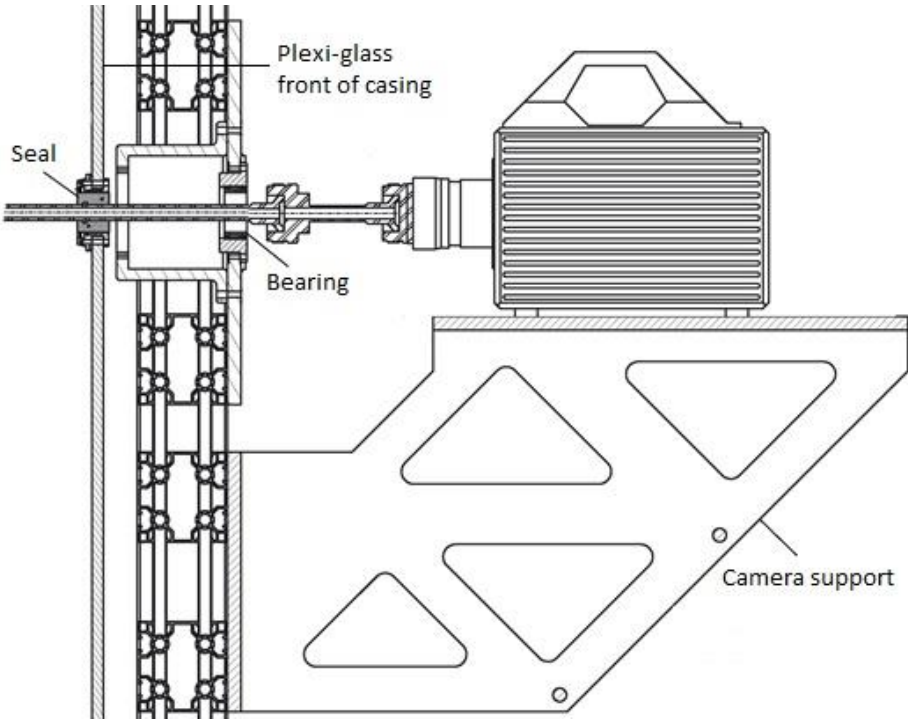


Figure 1: Schematic of the supporting system

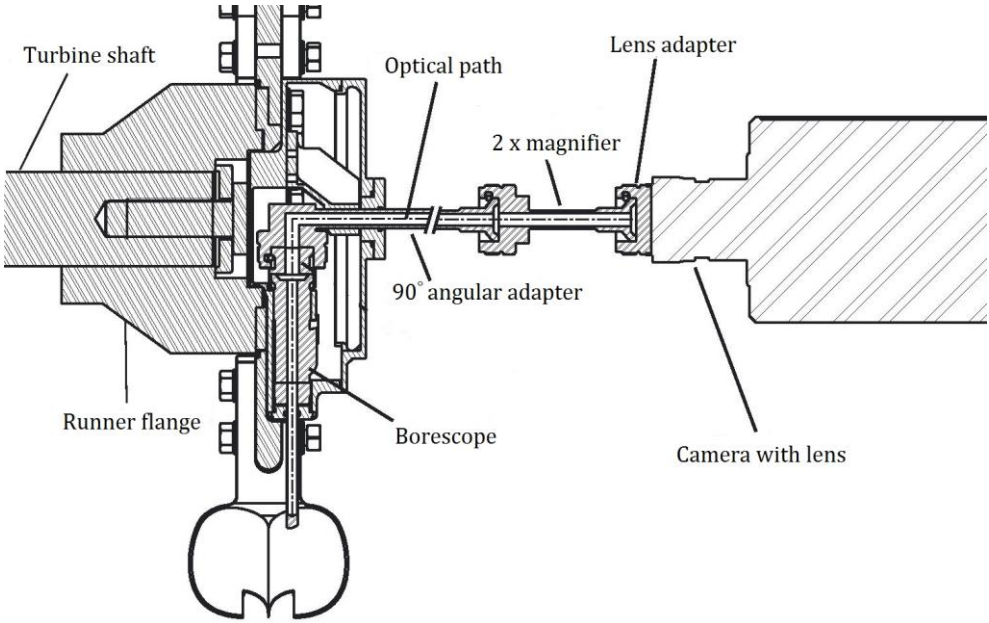


Figure 2: Schematic of the optical system

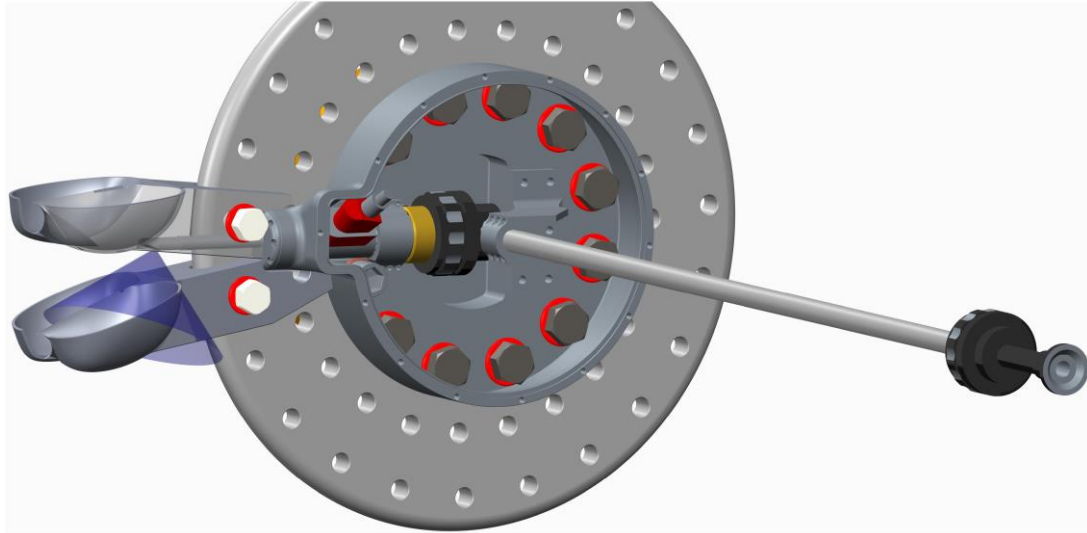


Figure 3: CAD-drawing from the design process, illustrating the desired setup

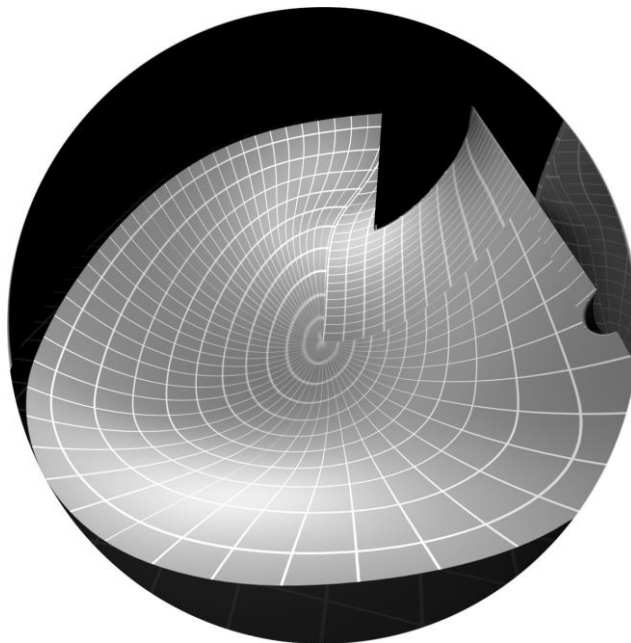


Figure 4: CAD-drawing from the design process, illustrating the resulting visible area seen through the borescope, as of Figure 3



Figure 5: The optical system is split in a rotating and a stationary section

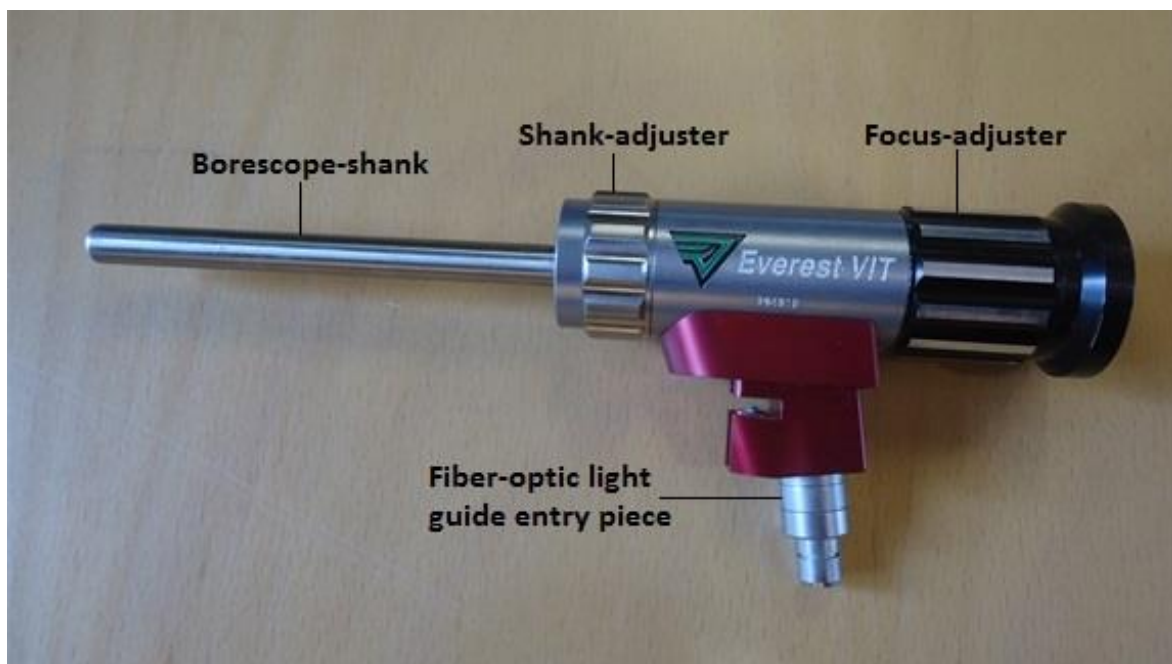


Figure 6: Borescope



Figure 7: Complete installation, with the laser for lighting placed to the right. The other light sources are only used during installation

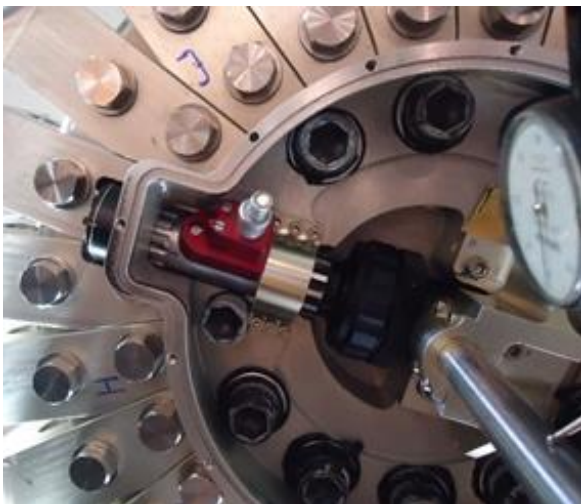


Figure 8: Inside the borescope casing, while balancing the shank of the 90° angular adapter

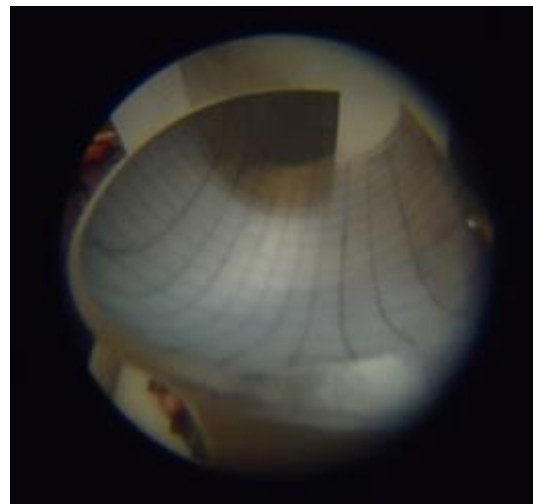


Figure 9: Visible region seen through the borescope, when no water in the system

4 LIGHTING SETUP

In general, the borescope, and its associated adapters, limit the amount of light that can slip through. In addition, the large amount of water inside the turbine casing during experiments hinders lights from sources outside the Plexi-glass to let through. The author's Master's thesis [1] suggests that a lighting setup including a pulsating laser functioning as a blitz may be a preferred option. However, other lighting setups, for example based on light intense flash lamps, may be an optional solution.

In case of using laser for illumination, cover the area around the Pelton test-rig with a light-absorbing tent. Since the laser pulse has less duration than the shutter speed of the camera, it is important for the clearness of the film that no light slips into the tent. In addition, for safety reasons, no light from the laser shall slip out of the tent. The tent has to be build high enough to allow hot light sources to be placed on top of the rig. There should be space for the end part of the laser, the camera support, as well as any other light sources. Typical dimensions of the tent can be height: 2.4 m; Length in the direction of the jet: 3.5 m; Width: 2.0 m. This is used in Figure 7.

Fiber-optic cables from the laser may be placed around inside the turbine casing at desired places, for lighting. One can for example use tiny metal pipes for leading the fiber cables. However, it is important that the laser never hit directly on the borescope lens, as it may ruin the camera. Factors that influence the choice of number and placement of optical cables are for example the angular span of investigation and the amount of laser power needed in each cable, depending on the amount of water at the operating points of investigation. The fastening of fiber-optic cables needs to take place before the mounting of the Plexi-glass, during installation of borescope setup.

5 ASSEMBLING THE BORESCOPE SETUP

This is the essence of the procedure, containing placement of the borescope, adapters and camera setup. A main part of this installation process is to ensure the rotating parts of the optical system can rotate without ever touching the stationary optical part. Thus, proper balancing of the rotating parts is of major concern. To prevent the water from getting near the optical parts inside the borescope casing, use plenty of Vaseline on O-rings and Loctite on screw threads, to ensure proper sealing. During experiments, the centrifugal forces will push the water away from the borescope. Therefore, the critical time concerning water leakage is just after running, when the turbine stands still. Thus, ensure the borescope is directed in either 5 o'clock or 7 o'clock direction when the runner is not in use.

5.1 BALANCING THE RUNNER

Depending on the design of the runner, and the way it sits on the shaft, the runner can obtain imbalance in the axial direction. To avoid fatal vibrations that eventually could cause the optical system to break, the runner needs to be balanced.

1. Attach the lid on the borescope casing, covering for the borescope shank, using an O-ring for sealing, as shown in Figure 10.



Figure 10: Fastening the lid for the borescope casing. White marks indicate the right position

2. Mount all buckets on the runner, with equal amount on force put on the bolts. Put the runner on the shaft, and mount the borescope casing on the runner. During the balancing of the runner, it is important to ensure all bolts through the borescope casing and runner is fastened tightly, with the same amount of strength. The borescope casing influence the way the bolts fasten the runner, and thus needs to be mounted on the runner while balancing.

Table 1: Shim distribution for runner balancing

A	0.30 mm
B	0.30 mm
C	0.35 mm
D	0.30 mm
E	0.20 mm
F	0.15 mm
G	0.10 mm
H	0.00 mm
I	0.00 mm
J	0.05 mm
K	0.15 mm
L	0.25 mm

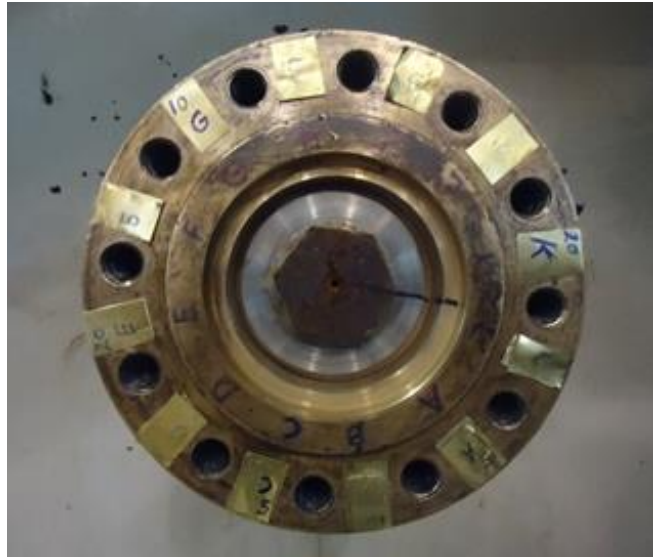


Figure 11: Shim distribution for runner balancing

3. Perform the balancing of the runner. Measure the deviation between the widest parts of the buckets, using a dial-indicator. Place shims on the shaft end, between the boltholes, as necessary to balance the runner. A maximum imbalance of less than 0.1 mm in all directions should be aimed for, although may be difficult to obtain. Ensure no weight is put on the turbine casing during the balancing process, as sitting on the edge of the casing can cause the dial indicator to move as much as 0.05 mm on average, when fastened on the casing. For the case with the runner of Solemslie, a shim distribution was put according to Table 1 and as shown in Figure 11. This resulted in a maximum imbalance of 0.15 mm. As the mid plate of the runner of Solemslie is thin, the amount and direction of imbalance depended strongly on the way the bolts were tightened. Therefore, a gradual shim distribution was needed. This shim distribution can be used as a foundation for later use as well, but in each case a complete balance process needs to be undertaken. It is of major importance that the shims are placed with equal distance from the center of rotation.
4. After obtained proper balance of the runner, seal the bolts to make sure no water slips through during experimentation.

5.2 PLACING THE BORESCOPE

Place the borescope in the borescope casing, as shown in Figure 12.



Figure 12: The placement of the borescope

5. To get the borescope in the right position with regard to the size of the obtained image, 7 disks are slid on the borescope. These disks are originally made for 6 mm bolts, all having a thickness of 1.5 mm.
6. Start the placement of the borescope by turning the borescope shank so that the lens is pointing directly outwards from the runner (at 9 o'clock). The fiber-optic light guide entry piece shall at the same be pointing at 11 o'clock direction, according to Figure 12.
7. Carefully push the borescope into the fitted hole in the bucket. When you see the tip of the shank with the lens being visible from the other side of the hole, stop. You will now feel the shaft gently butting against an edge at the hole exit. It is very important not to use any kind of force to try to fit the borescope, as it may jam. Instead, turn the shank-adjuster in the counter-clockwise direction, as the borescope is pointing to the left, until the borescope slips through the hole and into the right position.
8. Fasten the borescope with the associated clamp.

5.3 PLACING THE 90° ANGULAR ADAPTER

9. Fasten the adapter base to the 90° angular adapter, with the associated clamp. Place a shim all the way around the adapter inside the clamp, to make it tight.
10. Mount the adapter in the borescope casing, according to the engraved letters. Make sure the adapter does not jam to the borescope.

Set light to the bucket and look through the 90° angular adapter. Do approximate adjustments to the adapter relative to the borescope, to ensure no blurry edges on the visible image.

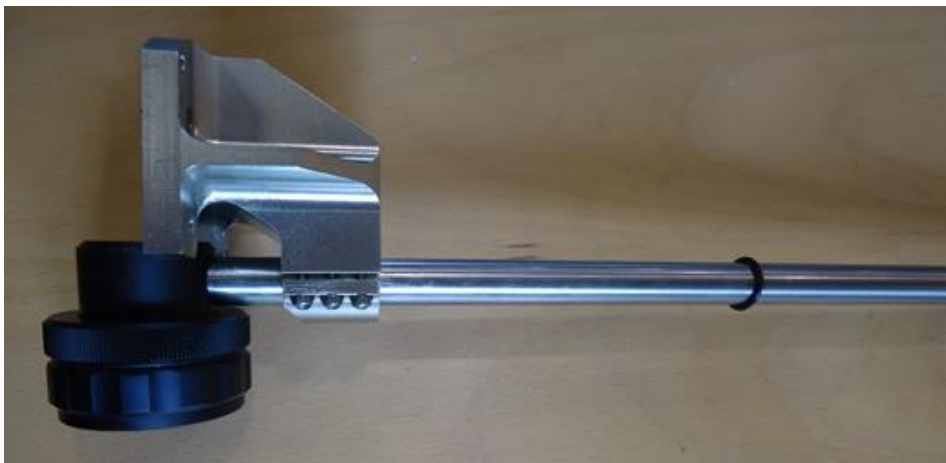


Figure 13: 90° angular adapter with base and clamp mounted

5.4 BALANCING THE 90° ANGULAR ADAPTER

During the balancing of the adapter, it is important to let the borescope point in the same direction between each adjustment with shims. This is because the adapter base is free to move sideways when the screws are loose, and the weight of the borescope will thus drag the base in one direction. For the case with Solemslie's runner, the runner was rotated so that the borescope pointed in the 7 o'clock direction. Place a dial indicator on both the inner and outer part of the adapter shank.

11. First, adjust the adapter base so to minimize the imbalance of the inner part of the adapter shank, i.e. close to the clamp, without the use of shims.
12. Then use shims to balance the outer part of the adapter. Be aware that the direction of the shim placement has large influence on its effect. When placing shims, ensure the adapter base does not change its location. The way the screws are tightened highly affects the way the shims work together. It might be wise to wait with the central screw until the end. As a starting point, the shim distribution for Solemslie's runner can be used, as described in Table 2. In that case, all shims were put directly in from the side, just touching the screw, as shown in Figure 14. It resulted in 0.08 mm of imbalance at both ends of the adapter.

5.5 SEALING AND SUPPORTING

16. Put an O-ring along the outer edge of the borescope casing, and put on the casing cover.

17. Fasten the disk on the top of the cover, as shown in Figure 15. Put some Loctite 510 between the two split halves, as the O-rings in the disk do not seal sufficiently.



Figure 15: Fastening the cover of the borescope casing



Figure 16: Sealing and guiding cylinders

18. Carry out a new balancing of the 90° angular adapter, and make a mark on the shank to show where the 0-point is. This is done to know what direction, and to what extent, to push the shank in, after putting on the sealing cylinder.
19. Fasten the sealing cylinder to the adapter shank. Put on the left part of the Plexi-glass, together with the guiding cylinders, which are mounted on each side of the Plexi-glass itself. This is illustrated in Figure 16.
20. Put on the right part of the Plexi-glass, and mount it tightly, keeping the guiding cylinders loose.
21. Go through a final balancing of the 90° angular adapter, looking for imbalance in two directions simultaneously. One other person must manually rotate the generator shaft while balancing. Remember to fasten the dial indicators to the turbine casing, as the bodyweight on the floor influences the measurement, if the floor is in connection with the dial indicator. Twist the guiding cylinders to push the adapter shank into balance. In the case of Solemslie's runner, a final imbalance of 0.15 mm was obtained, and considered acceptable.



Figure 17: Final balancing of the 90° angular adapter



Figure 18: Fastening the clamp to lay inside the bearing in the camera support

22. Fasten the clamp associated with the bearing on the adapter shank.
23. Mount the camera support to the rig. Then fasten the bearing on the camera support, as shown in Figure 19.
24. Adjust the camera support to allow the 90° angular adapter to move freely, without any contact with the bearing. The support is equipped with two screws that control the height. It is also possible to move the support sideways.
25. Place the camera on the camera support, and fasten the magnifier adapter to the camera. Do further adjustments to align the camera with the 90° angular adapter. The four screws holding the camera to the camera support are to be used for the final adjustment. Because of the rubber feet of the camera, the tightening of these screws has significant effect on the camera alignment.
26. As a final test to check that the 90° angular adapter moves completely freely inside the end of the magnifier adapter, a light nudge with a fingertip from all sides of the magnifier adapter end can be done. You should hear the sound of two metals hitting each other, as a sign that it is free space between the two adapter-ends.



Figure 19: Mounting the bearing outside the camera support



Figure 20: Aligning the camera with the adapter, while fastening it to the support

6 PREPARATIONS BEFORE FILMING

6.1 TRIGGERING THE CAMERA

6.1.1 Option 1 – By use of the rotational speed measuring system

1. Adjust the trigger on the slotted disk on the rotational speed measuring system, situated on the shaft. Set it in the angular position where you want the filming to start.
2. Connect the triggering signal from the computer in the control room with a laptop. Adjust the settings in FastCam Viewer to account for external triggering.
3. Connect a synchronization cable from the laptop to the camera, through a logging box.

6.1.2 Option 2 – Filming without triggering

Film several runner revolutions to ensure the desired angular span of the bucket duty cycle is covered. The drawback is that different films will not start at the same angular positions, thus making a flow comparison between different operation points less accurate.

6.2 CHOOSING THE RIGHT CAMERA FRAME RATE

6.2.1 Option 1 – Ensure frames from different films are taken at the same positions

If a comparison of the flow from operating points having different rotational speeds is to be undertaken, it is wise to choose the camera frame rate so that the increase in angle of rotation for the runner between every frame taken is the same for all films, regardless of the rotational speed.

1. Choose a desired angular span, θ , to investigate, and the number of frames you want to cover that span. Calculate the frame rate using the following relations:

$$\text{Filming time} = \frac{\theta}{\omega} \quad [s] \quad (1)$$

$$\text{Frame rate} = \frac{\text{Number of frames}}{\text{Filming time}} \quad \left[\frac{\text{frames}}{s} \right] \quad (2)$$

Where ω is the rotational speed of the runner, measured in degrees/s, and θ the chosen angular span, in degrees.

2. Make a LabView program to feed the calculated frame rate to FastCam Viewer.

6.2.2 Option 2 – Setting a frame rate of one's own choice

A frame rate restricted to give a certain number of frames over a desired angular span may not be an optimal frame rate with regard to resolution and shutter speed. If only one operating point is to be investigated, one can seek for optimal conditions and choose the desired frame rate directly in FastCam Viewer.

6.3 SYNCHRONIZING THE CAMERA WITH A LASER

One can synchronize the two units either way. To control the laser pulse on an Oxford Laser's LS 20-10 Copper Vapor Laser by the camera frame rate, do the following:

1. Pull one signal cable from the camera, marked “general out” to the “force external”-input on the laser. Set the settings for this cable in FastCam Viewer to “Rec pos”, meaning that laser should only send pulses when the camera is recording.
2. Pull another signal cable from the camera to the laser’s sync-input, also marked “general out”. This cable is set to “Sync neg” in FastCam Viewer.

Make sure not to force the laser to give any pulses in a frequency range the laser is not build for. Thus, it is wise to unplug the synchronization cables during start-up.

6.4 INSTALLING THE LIGHTING SETUP

When using a laser for lighting purpose, use the appropriate laser procedure for preparations. Any fiber-optic cable should be placed inside the turbine casing before installing the camera support assembly, as mentioned in Chapter 4.

7 FILMING

Use the procedures for running the Pelton test rig and appropriate laser, in case of lighting by laser. Use the associated camera software on a laptop for controlling the synchronizations and recordings. For FastCam Viewer, read the accompanying user manual before use. Check the connection between the stationary and rotating parts of the borescope setup regularly during testing, to ensure no direct contact is established. When done testing, rotate the runner manually to ensure the borescope is pointing in the 5 o'clock or 7 o'clock-direction. This is done to hinder the water to come inside the borescope casing, in case of improper sealing.

Recommended settings in FastCam Viewer, for better post-processing:

- Save the files in MRAW-format, and choose the highest bit-depth, to save the most information in the film. The choice of bits shown can be adjusted by the HDR function afterwards. However, this format takes a lot of space.
- Use the "shading" function each time it blinks.

8 POST-PROCESSING OF FILM

The obtained images are rotated relative to each other, since the borescope is rotating relative to the camera. Knowing the rotational speed and camera frame rate, one can rotate the images back to the same position, using software like MATLAB. The lens of the borescope is of the fish-eye type. Thus, the images obtained from the high-speed filming need to be converted into normal perspectives before quantitative analysis can take place. Furthermore, the images show a bucket that is inclined relative to the CAD-image of the bucket with known geometry. Using the known grid locations in the bucket, one can transform the inclined images into ones that fit the CAD-image. Then, each pixel in an image can be given an X, Y and Z-coordinate, corresponding to the real bucket, and one can start to analyze the flow in the bucket quantitatively.

9 REFERENCES

- [1] A. T. Larsen, «Pelton turbine - Model test of a runner,» NTNU, Trondheim, 2015.
- [2] B. W. Solemslie and O. G. Dahlhaug, "A reference pelton turbine - design and efficiency measurements," in *IOP Conference Series: Earth and Environmental Science*, 2014.
- [3] Henke-Sass Wolf, Henke-Sass Wolf GmbH, [Online]. Available: <http://www.henkesasswolf.de/>. [Accessed 25 6 2015].

APPENDIX B – LASER PROCEDURE

Attachment to Risk Assessment report

High-speed filming with Laser on Pelton Test Rig

Prosjektnavn	High-speed filming with Laser on Pelton Test Rig
Apparatur	LS 20-10 Copper Vapor Laser
Enhet	EPT
Apparaturansvarlig	Bård Brandåstrø
Prosjektleder	Ole Gunnar Dahlhaug
HMS-koordinator	Morten Grønli
HMS-ansvarlig (linjeleder)	Olav Bolland
Plassering	Waterpower Laboratory
Romnummer	11
Risikovurdering utført av	Audun Tufte Larsen and Bjørn Winther Solemslie

TABLE OF CONTENTS

ATTACHMENT A: PROCESS AND INSTRUMENTATION DIAGRAM	1
ATTACHMENT B: HAZOP TEMPLATE	3
ATTACHMENT C: TEST CERTIFICATE FOR LOCAL PRESSURE TESTING.....	6
ATTACHMENT D: HAZOP PROCEDURE (TEMPLATE).....	7
ATTACHMENT E: PROCEDURE FOR RUNNING EXPERIMENTS.....	8
ATTACHMENT F: TRAINING OF OPERATORS	12
ATTACHMENT G: FORM FOR SAFE JOB ANALYSIS.....	13
APPARATURKORT / UNITCARD.....	15
FORSØK PÅGÅR /EXPERIMENT IN PROGRESS	16

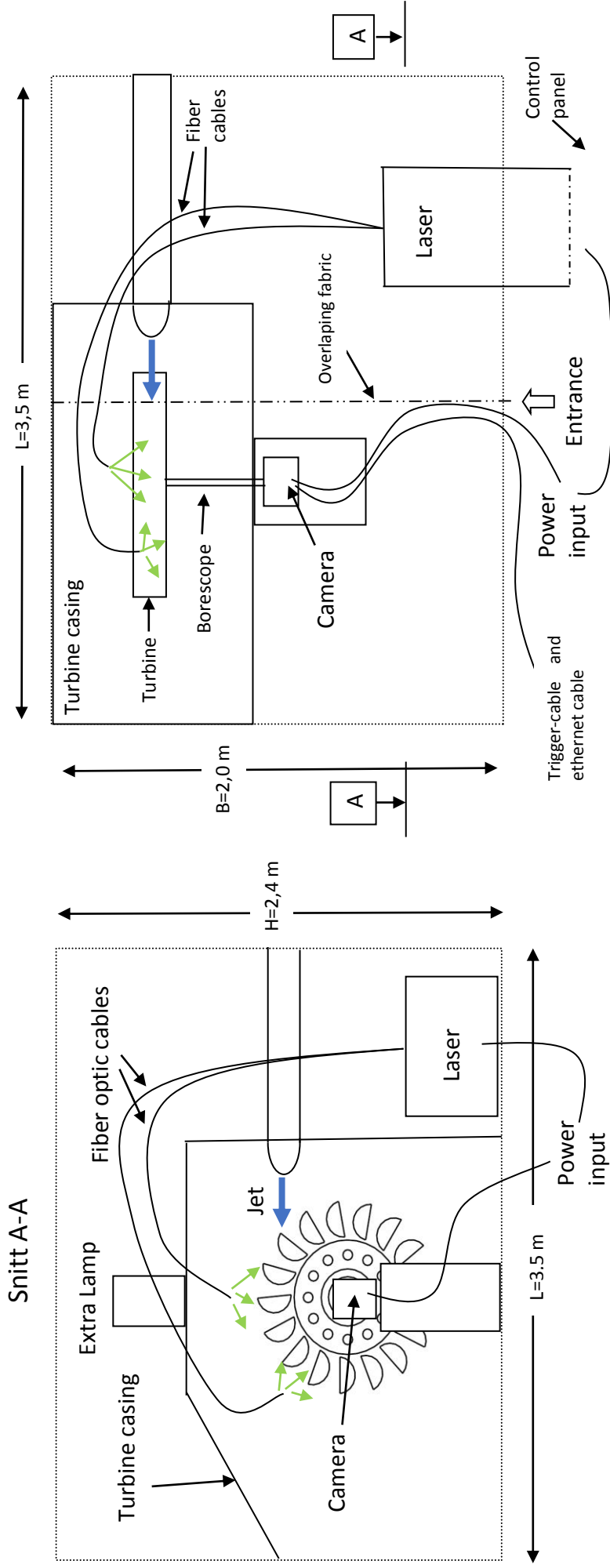
ATTACHMENT A: PROCESS AND INSTRUMENTATION DIAGRAM

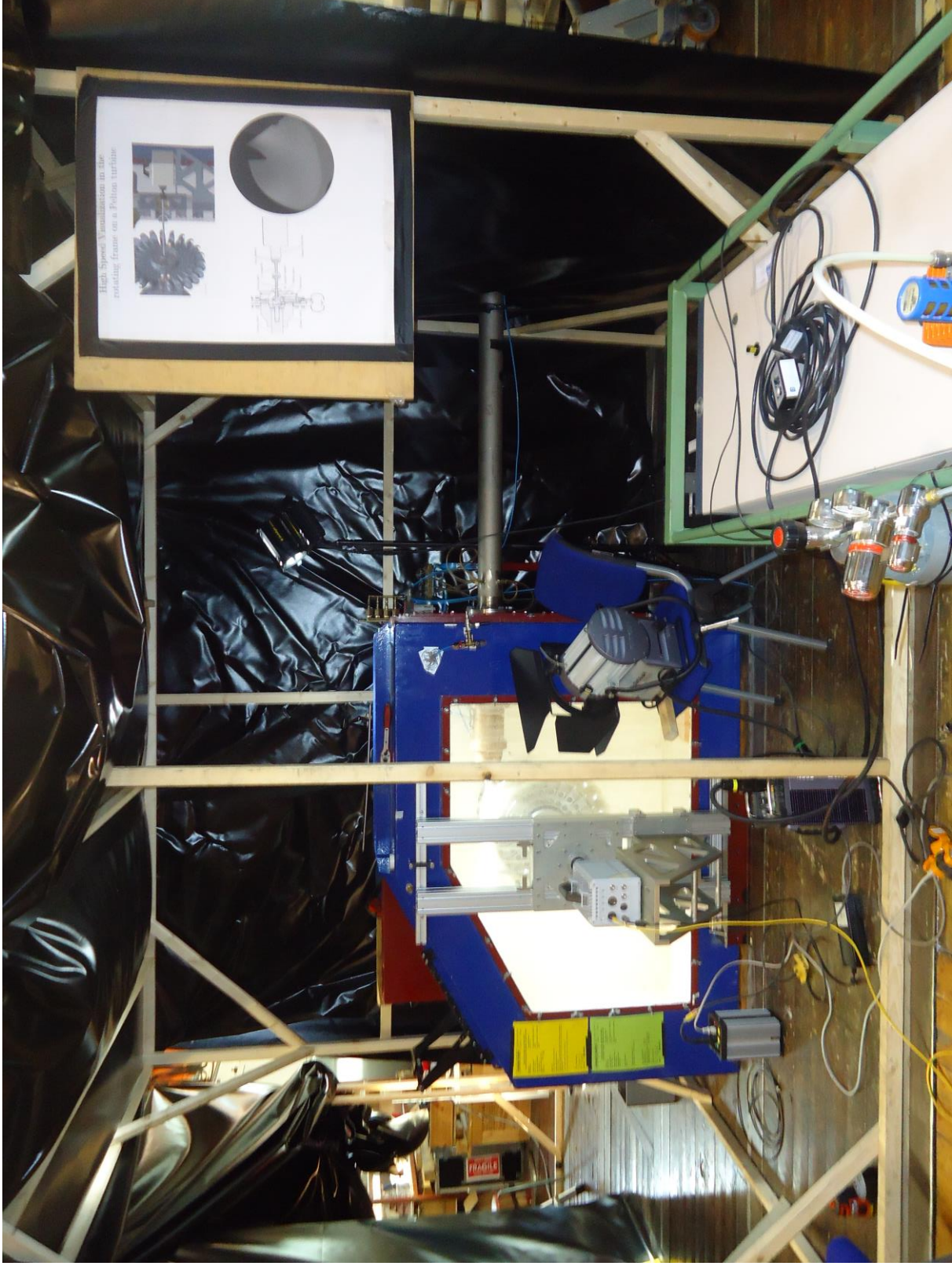
Radiation area is blocked on all sides by light-blocking fabric (this includes a roof). The holes in the floor will be covered satisfactory, so that, in general, no light will be emitted from inside the tent to the environment. Most of the casing of the laser is placed outside the tent, to have access to the control panel while using the laser. The end of the laser casing where the laser beam itself is emitted, is placed inside the tent, as illustrated on the figures on the next page.

The entrance is overlapping fabric, with a warning sign on it. A socket for the current powering the laser will be placed outside the entrance, to easily stop the laser in case of emergency shutdown. A warning light in front of the entrance will activate when the laser is on. During the operation of the laser, the operator will stand outside the tent, and control the triggered external pulse to the camera from a computer. At all time during operation of the laser, the operator will wear specialized necessary eyewear. Three pair of these glasses are provided.

On the figures on the next page, the rectangular frames denotes the placement of the plastic fabric covering the experimental area (the tent). Lengths are given as in the figures, although internal pieces are not in scale. The tent is held up by a simple construction of plank, with several joists (tverrplanker) on the top for holding the roof of the tent. The roof is made with extra clearance for the height, to give good space for the possible hot air coming for the equipment consuming electricity, or lamps.

There have been made specialized blockages in the Waterpower Laboratory, covering the two possible exits for laser beam. For safety reason, these will always be on, except when running the laser. This has been installed in order not to unintentionally emit the laser beam.





ATTACHMENT B: HAZOP TEMPLATE

Project: Node: Laser							Page
Ref	Guideword	Causes	Consequences	Safeguards	Recommendations	Action	Date/Sign
	Unintentional rarefaction of beam	Poor alignment of laser beam, unintentional beam obstruction	Damage to personnel, damage to equipment	Laser emitter latched in place, radiation area enclosed	Careful instrument handling		
	Laser generation unit temperature rise	Cooling system failure	Equipment will overheat and break	-	Be aware of equipment condition		
	Unprotected personnel entering radiation area	Insufficient signalling, radiation area too accessible	Possibility of severe damage to personnel	Signalling and warning light in place, radiation area enclosed with physical obstruction	Always run experiments with warning light on		
	Electrical failures in apparatuses	Wear, poor construction	Equipment failure				
	Fire hazard	Laser beam hitting flammable material	Fire	Enclosing fabric approved for shielding laser experiments.	Make sure a fire extinguisher is easily available		
	Beam interception by operator	Careless equipment handling, obstructed work area	Damage to personnel, severe if lacking protective gear	Goggles approved for laser in use worn by operator	Careful instrument handling		
	Unstable laser	Careless handling of pulse trigger	Equipment damage, worst		Carefully follow instructions, keep an		

Project: Node: Laser		Page					
Ref	Guideword	Causes	Consequences	Safeguards	Recommendations	Action	Date/Sign
	Cap for gas tank falls off	Gas tank falls to the ground, the cap hits the floor	case explosion Gas tank become like a projectile, gaining speed	Fasten the gas tank tightly to the laser cover	eye on pulse frequency Make sure cap is fastened		
	Unwanted water coming out from an open pipe	Forgetting to close the valve to the swirl rig	Destroyed electrical equipment	No important electrical equipment on the floor	Double check that all but the valves to the Pelton rig are closed. Know where the main electrical fuse is situated.		

ATTACHMENT C: TEST CERTIFICATE FOR LOCAL PRESSURE TESTING

Trykkpåkjent utstyr:	
Benyttes i rigg:	
Design trykk for utstyr (bara):	
Maksimum tillatt trykk (bara): (i.e. burst pressure om kjent)	
Maksimum driftstrykk i denne rigg:	

Prøvetrykket skal fastlegges i følge standarden og med hensyn til maksimum tillatt trykk.

Prøvetrykk (bara):	
X maksimum driftstrykk: I følge standard	
Test medium:	
Temperatur (°C)	
Start tid:	Trykk (bara):
Slutt tid:	Trykk (bara):
Maksimum driftstrykk i denne rigg:	

Eventuelle repetisjoner fra atm. trykk til maksimum prøvetrykk:.....

Test trykket, dato for testing og maksimum tillatt driftstrykk skal markers på (skilt eller innslått)

 Sted og dato

 Signatur

ATTACHMENT D: HAZOP PROCEDURE (TEMPLATE)

Project: Node: 1		Page					
Ref#	Guideword	Causes	Consequences	Safeguards	Recommendations	Action	Date/Sign
	Not clear procedure	Procedure is to ambitious, or confusingly					
	Step in the wrong place	The procedure can lead to actions done in the wrong pattern or sequence					
	Wrong actions	Procedure improperly specified					
	Incorrect information	Information provided in advance of the specified action is wrong					
	Step missing	Missing step, or step requires too much of operator					
	Step unsuccessful	Step has a high probability of failure					
	Influence and effects from other	Procedure's performance can be affected by other sources					

ATTACHMENT E: PROCEDURE FOR RUNNING EXPERIMENTS

Prosjekt High-speed filming with Laser on Pelton Test Rig	Dato 01.11.2014	Signatur
Apparatur LS 20-10 Copper Vapor Laser		
Prosjektleder Ole Gunnar Dahlhaug		

	Conditions for the experiment:	Completed
	Experiments should be run in normal working hours, 08:00-16:00 during winter time and 08.00-15.00 during summer time. Experiments outside normal working hours shall be approved.	
	One person must always be present while running experiments, and should be approved as an experimental leader.	
	An early warning is given according to the lab rules, and accepted by authorized personnel.	
	Be sure that everyone taking part of the experiment is wearing the necessary protecting equipment and is aware of the shut-down procedure and escape routes.	
	Preparations	Carried out
	<i>Ensure all people exposed to the laser system are wearing appropriate eye protection for any wavelengths of light that the laser could generate (510.6-578.2 nm (yellow and green light)).</i>	
	<i>Make sure the tent covering the area does not let any light out to the environment. Check holes in the floor, overlapping areas in the tent, including the entrance. The area within the tent should be totally dark.</i>	
	<i>Post the "Experiment in progress" sign and warning sign on the tent entrance. Put on "laser is on" signs on the entrance doors (on both ground- and first floor). Activate the warning light in front of tent (if it is not directly coupled to the main switch supplying the laser).</i>	
	<i>Ensure the laser has been installed correctly.</i>	
	<i>Make sure all necessary wires are connected, like the fibre from the laser output to the lighting area. If you want to use an external trigger for the laser pulse (instead of the internal pulse of 10 kHz), for instance as a blitz for camera, let the signal cable go from a computer, through the high-speed camera before it reaches the laser. In FastCam Viewer, one can set the "Camera options"-settings for a "General out"-cable to "Sync neg", and use the chosen cable for synchronization. However, for safety reasons, wait until the laser is ready to plug the sync-cable in the laser sync-input on the short-end of the laser. Just let it lay outside the tent.</i>	
	<i>For external triggering: Set laser switch to "internal trigger", and put in a "high" 5V signal in the "force external" input which forces the external triggering whenever the camera is recording – and only then. (E.g. "Rec Pos" controlled from the FastCam Viewer software, through a "General out"-cable). This mechanism is to ensure the frequency of the laser does not</i>	

	<i>change whenever the frequency is changed in FastCam Viewer.</i>	
	<i>For internal triggering: Use “internal trigger” only.</i>	
	<i>Remove the correct external blockages covering the exit of the laser beam, and make sure the beam does not get parted/reflected if only using one fibre.</i>	
	<i>Ensure the oil level on the water pump is within satisfactory limits. Per time (13.6.15) the water pump has some oil leakage, and needs to be refilled between each time used.</i>	
	<i>Turn the main power on, and ensure the emergency stop button is released. The red warning light outside the tent shall now be lighting, indicating activated laser/experiment in progress. The required power supply to the laser is 3 kW. Make sure you do not need a separate circuit supplying the laser.</i>	
	<i>Open the cap of the gas tank, so that the pipes get pressurized. The barometer normally shows 2-3 bar. Make sure the pressure in the tank does not go below 0.7 bar, and that the tank sits tightly.</i>	
	<i>Turn on the water supply, for the cooling system, and make sure the pump has power supply. The pump shall start by itself.</i>	
	<i>Turn on the isolation switch, next to the key-switch.</i>	
	<i>Turn on the key-switch (ignition/“tenning”). The vacuum pump will start by itself.</i>	
	<i>All the green lights on the front side display on the laser shall now be on, and the laser ready to start.</i>	
	<i>Ensure the internal physical power switch in front of the laser beam exit is working. The switch of this barrier is placed outside the tent, on the black box end of the laser, near the beam exit.</i>	
	<i>Press ‘start’ on the laser.</i>	
	<i>Wait for 1.5 hour for the laser to reach high enough temperature (typically in the order of 1500 °C), and desirable power output (max 20 watts).</i>	
	<i>Start the Pelton rig, according it its procedure, and turn on the camera.</i>	
	<i>When ready to use the laser, open the power switch from outside the tent, to let out the laser beam.</i>	
	<i>Make sure nobody enters the tent, including the operator, while the laser is running.</i>	
	<i>If you want to use an external triggered pulse (instead of the internal pulse of 10 kHz), plug in your signal wire into the sync-input at the short end of the laser, as well as the trigger signal wire in the “force external” input on the long front side of the laser.</i>	
	<i>In case of external triggering pulses, start your computer program and send the desired pulses to the laser. The laser is designed for a frequency range of 3.5-10 kHz. Extended Frequency Option is required to optimize the laser performance at frequencies below 10 kHz. Please NOTE: With current high voltage capacitor settings in the laser (per 13.6.15), the laser can only properly deliver 8-12 kHz. Ensure low frequency capacitors are inserted for lower frequency triggering. Also NOTE: Make sure not to change frequency up and down within a short period, as the laser then can become unstable and explode (although unlikely to happen).</i>	
	During the experiment	
	Keep unauthorized personnel out of radiation area.	
	Avoid wearing jewellery and/or shiny objects, to avoid getting any reflection	

Operator(s):

Navn	Dato	Signatur
Audun Tufte Larsen		
Bjørn Winther Solemslie		

ATTACHMENT F: TRAINING OF OPERATORS

Prosjekt	Dato	Signatur
High-speed filming with Laser on Pelton Test Rig	03.11.2014	
Apparatur LS 20-10 Copper Vapor Laser		
Prosjektleder Ole Gunnar Dalhaug		

	Knowledge about EPT LAB in general	
	Lab <ul style="list-style-type: none"> • Access • routines and rules • working hour 	
	Knowledge about the evacuation procedures.	
	Activity calendar for the Lab	
	Early warning, iept-experiments@ivt.ntnu.no	
	Knowledge about the experiments	
	Procedures for the experiments	
	Emergency shutdown.	
	Nearest fire and first aid station.	

I hereby declare that I have read and understood the regulatory requirements has received appropriate training to run this experiment and are aware of my personal responsibility by working in EPT laboratories.

Operator(s):

Navn	Dato	Signatur
Audun Tufte Larsen		
Bjørn Winther Solemslie		

ATTACHMENT G: FORM FOR SAFE JOB ANALYSIS

SJA name:	
Date:	Location:
Mark for completed checklist:	

Participators:		
SJA-responsible:		

Specification of work (What and how?):
Risks associated with the work:
Safeguards: (plan for actions, see next page):
Conclusions/comments:

Recommended/approved	Date/Signature:	Recommended/approved	Date/Signature:
SJA-responsible:		HSE responsible:	
Responsible for work:		Other, (position):	

HSE aspect	Yes	No	NA	Comments / actions	Resp.
Documentation, experience, qualifications					
Known operation or work?	X				
Knowledge of experiences / incidents from similar operations?		X			
Necessary personnel?	X				
Communication and coordinating					
Potential conflicts with other operations?		X			
Handling of an eventually incident (alarm, evacuation)?		X			
Need for extra assistance / watch?		X			
Working area					
Unusual working position		X			
Work in tanks, manhole?		X			
Work in ditch, shaft or pit?		X			
Clean and tidy?	X				
Protective equipment beyond the personal?		X			
Weather, wind, visibility, lighting, ventilation?	X				
Usage of scaffolding/lifts/belts/ straps, anti-falling device?		X			
Work at heights?		X			
Ionizing radiation?		X			
Influence of escape routes?		X			
Chemical hazards					
Usage of hazardous/toxic/corrosive chemicals?		X			
Usage of flammable or explosive chemicals?		X			
Risk assessment of usage?	X				
Biological materials/substances?		X			
Dust/asbestos/dust from insulation?		X			
Mechanical hazards					
Stability/strength/tension?		X			
Crush/clamp/cut/hit?		X			
Dust/pressure/temperature?		X			
Handling of waste disposal?		X			
Need of special tools?		X			
Electrical hazards					
Current/Voltage/over 1000V?		X			
Current surge, short circuit?		X			
Loss of current supply?		X			
Area					
Need for inspection?	X				
Marking/system of signs/rope off?	X				
Environmental consequences?		X			
Key physical security systems					
Work on or demounting of safety systems?		X			
Other					

APPARATURKORT / UNITCARD

Dette kortet SKAL henges godt synlig på apparaturen!
This card MUST be posted on a visible place on the unit!

Apparatur (Unit) LS 20-10 Copper Vapor Laser	
Prosjektleder (Project Leader) Ole Gunnar Dahlhaug	Telefon mobil/privat (Phone no. mobile/private)
Apparaturansvarlig (Unit Responsible) Bård Brandåstrø	Telefon mobil/privat (Phone no. mobile/private)
Sikkerhetsrisikoer (Safety hazards) Laser	
Sikkerhetsregler (Safety rules) -Wear appropriate safety goggles for laser wavelength -no shiny objects (eg. Jewellery) worn	
Nødstopprosedyre (Emergency shutdown) Turn off or unplug the laser from the power supply	

Her finner du (Here you will find):

Prosedyrer (Procedures)	Apparaturperm ved laser
Bruksanvisning (Users manual)	Apparaturperm ved laser

Nærmeste (Nearest)

Brannslukningsapparat (fire extinguisher)	Vestveggen i Lab
Førstehjelpsskap (first aid cabinet)	Vestveggen i Lab

NTNU
Institutt for energi og prosessteknikk

SINTEF Energi
Avdeling energiprosesser

Dato

Dato

Signert

Signert

FORSØK PÅGÅR / EXPERIMENT IN PROGRESS

Dette kortet SKAL henges opp før forsøk kan starte!
This card MUST be posted on the unit before the experiment startup!

Apparatur (Unit) LS 20-10 Copper Vapor Laser	
Prosjektleder (Project Leader) Ole Gunnar Dahlhaug	Telefon mobil/privat (Phone no. mobile/private) 918 97 609
Apparaturansvarlig (Unit Responsible) Bård Brandåstrø	Telefon mobil/privat (Phone no. mobile/private) 918 97 257
Godkjente operatører (Approved Operators) Bjørn Winther Solemslie Audun Tufte Larsen	Telefon mobil/privat (Phone no. mobile/private) 932 12 395 936 96 536
Prosjekt (Project) High-speed filming with Laser on Pelton Test Rig	
Forsøksstid / Experimental time (start - stop) 10.11.2014-10.11.2015	
Kort beskrivelse av forsøket og relaterte farer (Short description of the experiment and related hazards) Laser measurements with class IV laser on the Pelton Test Rig, danger of eye injury and skin injury. Radiation area clearly marked, and a tent is covering the area. The flashing laser light can in some cases trigger epilepsy if proper goggles are not worn.	

NTNU
Institutt for energi og prosessteknikk

SINTEF Energi
Avdeling energiprosesser

Dato

Dato

Signert

Signert

APPENDIX C – CALIBRATION DATA

APPENDIX C, CALIBRATION DATA

C.1 TORQUE TRANSDUCER

CALIBRATION PROPERTIES

Calibrated by: Audun Tufte Larsen
Type/Producer: HBM T12
SN: 2867610
Range: 0-500 Nm
Unit: Nm

CALIBRATION SOURCE PROPERTIES

Type/Producer: Torque Transducer HBM
SN: 66256
Uncertainty [%]: 0,01

POLY FIT EQUATION:

$Y = -8.60199723E+0X^0 - 50.28245571E+0X^1$

CALIBRATION SUMMARY:

Max Uncertainty : Inf [%]
Max Uncertainty : 0.919049 [Nm]
RSQ : 0.999938
Calibration points : 30

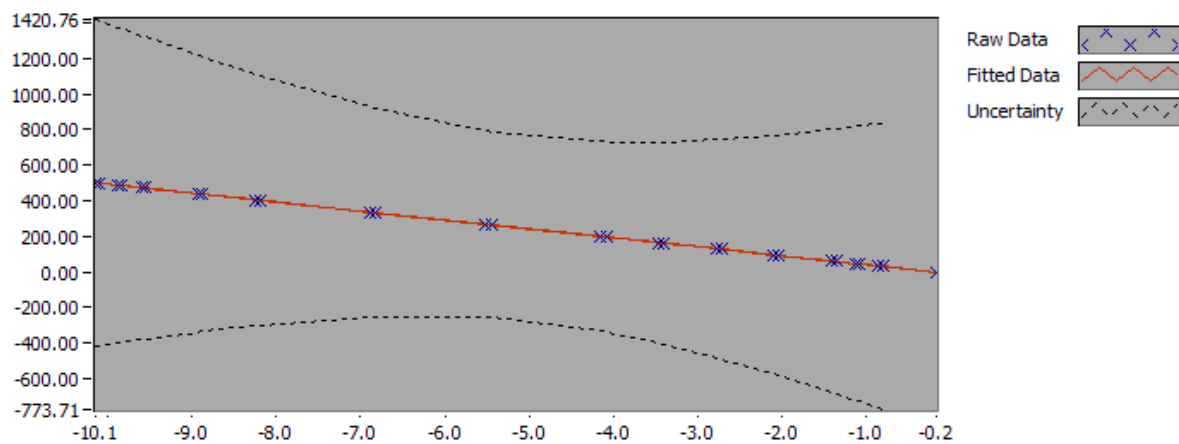


Figure 1 : Calibration chart (The uncertainty band is multiplied by 1000)

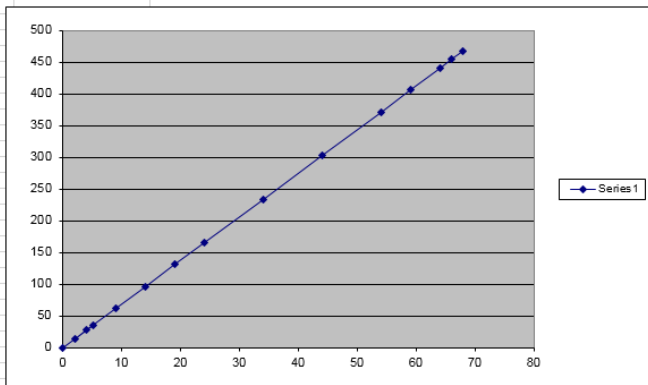
CALIBRATION VALUES

Value [Nm]	Voltage [V]	Best Poly Fit [Nm]	Deviation [Nm]	Uncertainty [%]	Uncertainty [Nm]
0.000000	-0.158988	-0.607689	0.607689	Inf	NaN
32.755950	-0.798340	31.540497	1.215452	2.458333	0.805250
46.523324	-1.069769	45.188622	1.334702	1.666144	0.775146
60.294927	-1.339806	58.766717	1.528210	1.237441	0.746114
94.730028	-2.024449	93.192279	1.537749	0.715046	0.677364
129.165597	-2.706375	127.481189	1.684409	0.478174	0.617636
163.600437	-3.393670	162.040087	1.560349	0.347861	0.569103
198.031131	-4.076709	196.384952	1.646178	0.270472	0.535619
266.904156	-5.444616	265.166646	1.737510	0.195905	0.522879
335.779317	-6.817756	334.211522	1.567795	0.173975	0.584171
404.652756	-8.199315	403.679711	0.973046	0.173307	0.701290
439.088339	-8.889021	438.359798	0.728541	0.176092	0.773199
473.521857	-9.559745	472.085446	1.436411	0.179281	0.848934
487.293466	-9.841618	486.258749	1.034717	0.181024	0.882117
501.049464	-10.110762	499.791927	1.257537	0.182502	0.914427
501.049464	-10.148865	501.707838	-0.658374	0.183425	0.919049
487.293466	-9.879830	488.180105	-0.886639	0.181960	0.886678
473.521857	-9.601173	474.168547	-0.646691	0.180302	0.853771
439.088339	-8.932784	440.560323	-1.471983	0.177182	0.777986
404.652756	-8.247788	406.117060	-1.464304	0.174498	0.706110
335.779317	-6.881803	337.431950	-1.652633	0.175281	0.588557
266.904156	-5.516236	268.767871	-1.863715	0.196443	0.524316
198.031131	-4.146676	199.903066	-1.871936	0.269200	0.533100
163.600437	-3.460489	165.399893	-1.799456	0.345429	0.565123
129.165611	-2.773169	130.839726	-1.674115	0.474096	0.612370
94.730028	-2.087089	96.341938	-1.611910	0.708834	0.671479
60.294927	-1.398837	61.734981	-1.440054	1.227124	0.739894
46.523324	-1.125978	48.014962	-1.491638	1.652987	0.769024
32.755950	-0.851922	34.234754	-1.478805	2.439994	0.799243
0.000000	-0.167853	-0.161955	0.161955	Inf	NaN

Kalibrering av Moment PÅLAST OG AVLAST

Arm 0.699941
 Gravitasjon 9.821465
 0.699851
 0.001429

D	Vekt [kg]	Moment [Nm]	Vekter	legg på	Ta av
0	0	0		0	
1	5.1275	35.24867168		5.1275	
2	1.999164	13.7431254	21	1.999164	21
3	3.998942	27.49047169	21 22	3.998942	22
4	8.999272	61.86492132	21 22 1	8.999272	1
5	13.99967	96.23985215	21 22 1 2	13.99967	2
6	18.99996	130.6140268	21 22 1 2 3	18.99996	3
7	23.99965	164.9840768	21 22 1 2 3 4	23.99965	4
8	34.00072	233.7357946	21 22 1 2 3 4 5 6	34.00072	5&6
9	44.0021	302.4896434	21 22 1 2 3 4 5 6 7 8	44.0021	7&8
10	54.00323	371.2417736	21 22 1 2 3 4 5 6 7 8 9 10	54.00323	9&10
11	59.00363	405.6167045	21 22 1 2 3 4 5 6 7 8 9 10 11	59.00363	11
12	64.00373	439.989573	21 22 1 2 3 4 5 6 7 8 9 10 11 12	64.00373	12
13	66.00351	453.7369261	21 22 1 2 3 4 5 6 7 8 9 10 11 12 23	66.00351	23
14	68.00102	467.468695	21 22 1 2 3 4 5 6 7 8 9 10 11 12 23 24	68.00102	24



0 0
 1 5
 2 10
 3 15
 4 20
 5 25
 6 40
 7 55
 8 70
 9 85
 10 100
 11 115
 12 130
 13 145
 14 160
 15 175
 16 180
 17 185
 18 190
 19 195
 20 200

C.2 VOLUME FLOW METER



WATERPOWER LABORATORY

Date: 19.09.2014

Operator: Audun Tufte Larsen og Ar

Calibration Sheet

Calibration of flow meter

Calibrator: Weighing tank system

Unit: Flowmeter, reg nr. 4624-7 (A03 36133)

Calibration constants for weighing tank correction

a ₁	3.73E-22
a ₂	-8.71E-17
a ₃	7.00E-12
a ₄	-2.19E-07
a ₅	1.00E+00

Corrected weight is calculated from formula where parameters a,b,c,d and e is achieved through substitution calibration.

$$W = a \cdot \frac{mW^5}{5} + b \cdot \frac{mW^4}{4} + c \cdot \frac{mW^3}{3} + d \cdot \frac{mW^2}{2} + e \cdot mW$$

Density of water is calculated from formula

$$\rho_w = \frac{1000}{(1 - 4.6699 \cdot 10^{-5} p_w) + 6 \cdot 10^{-4} (\theta - 4 + 2.1318913 \cdot 10^{-2} p_w)^2 - 6 \cdot 10^{-6} (\theta - 4 + 2.1318913 \cdot 10^{-2} p_w)^3}$$

Density of air is calculated from formula

$$\rho_a = \frac{(p_{atm} - 3.4837 \cdot 10^3)}{(273.15 + \theta)}$$

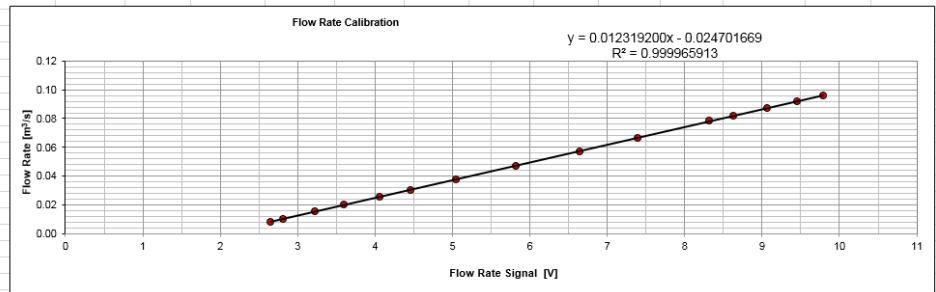
Comments: The flow rate changes during calibration. The inlet conditions to the pumps will

Discharge is found from formula

$$Q = \frac{W_2 - W_1}{\rho_a \cdot t \cdot (1 - \frac{\rho_w}{\rho_a})}$$

Date	Manual Observation before Weight [kg]	Manual Observation after Weight [kg]	Manual Observation Voltage [V]	Time [s]	Ambient pressure P _{amb} [kPa]	Water temp T _w [°C]	Air temp T _a [°C]	Calculated value before Weight [kg]	Calculated value after Weight [kg]	Differential weight [kg]	Density of water ρ [kg/m ³]	Density of air ρ [kg/m ³]	Differential volume [m ³]	Calculated Flow Rate Q [m ³ /s]	Estimate Q [m ³ /s]	Deviation [%]
19.09.2014	17523.8	19751.4	2.652572	280.094	101.34	18.52	20.74	17527.2	19753.3	2226.1	998.5406	1.2021	2.23207	0.0079690	0.00798	0.08630
19.09.2014	19751.4	21739.3	2.816493	200.099	101.33	18.79	20.77	19753.3	21739.7	1986.5	998.4878	1.2018	1.99186	0.0099544	0.01000	0.40927
19.09.2014	21739.3	23844.7	3.230079	140.098	101.33	18.93	20.78	21739.7	23843.5	2103.8	998.4601	1.2018	2.10956	0.0150577	0.01509	0.21610
19.09.2014	26188.1	28256.2	3.606099	105.100	101.32	19.00	21.03	26185.0	28251.5	2066.4	998.4462	1.2007	2.07213	0.0197158	0.01972	0.03449
19.09.2014	28256.2	30282.8	4.067891	80.099	101.31	19.04	21.12	28251.5	30276.4	2025.0	998.4382	1.2002	2.03057	0.0253508	0.02541	0.23892
19.09.2014	30282.8	32395.6	4.458641	70.100	101.30	19.04	21.10	30276.4	32387.5	2111.1	998.4382	1.2001	2.11697	0.0301993	0.03023	0.08562
19.09.2014	32395.6	34273.0	5.044404	50.099	101.31	19.07	21.10	32387.5	34263.5	1876.0	998.4322	1.2003	1.88116	0.0375489	0.03744	-0.28733
19.09.2014	34273.0	36385.0	5.820242	45.101	101.30	19.09	21.12	34263.5	36373.9	2110.4	998.4282	1.2001	2.11630	0.0469237	0.04700	0.16038
19.09.2014	36385.0	38671.7	6.650232	40.100	101.29	19.10	21.15	36373.9	38659.0	2285.1	998.4262	1.1998	2.29145	0.0571434	0.05722	0.14057
19.09.2014	38671.7	41336.0	7.399539	40.100	101.29	19.14	21.11	38659.0	41321.6	2662.6	998.4181	1.2000	2.66998	0.0665831	0.06645	-0.19316
19.09.2014	41336.0	44463.0	8.315051	40.100	101.29	19.14	21.16	41321.6	44446.7	3125.1	998.4181	1.1998	3.13385	0.0781507	0.07773	-0.53728
19.09.2014	44463.0	47740.2	8.631607	40.101	101.29	19.16	21.13	44446.7	47722.2	3275.4	998.4141	1.1999	3.28459	0.0819079	0.08163	-0.33691
19.09.2014	47740.2	51223.2	9.072892	40.101	101.29	19.18	21.22	47722.2	51203.5	3481.3	998.4101	1.1995	3.49107	0.0870568	0.08707	0.01409
19.09.2014	51223.2	54883.6	9.461261	40.099	101.28	19.17	21.26	51203.5	54862.3	3658.8	998.4121	1.1993	3.66905	0.0914999	0.09185	0.38498
19.09.2014	54883.6	58712.0	9.792714	40.099	101.28	19.20	21.33	54862.3	58689.2	3826.9	998.4061	1.1990	3.83762	0.0957036	0.09594	0.24299

Calibration constants, 20.02.2014	
C ₀	-0.0247017
C ₁	0.0123192



C.3 PRESSURE TRANSMITTER

CALIBRATION PROPERTIES

Calibrated by: Audun Tufte Larsen
Type/Producer: Tectis
SN: 3276.076.001
Range: 0-16 bar
Unit: kPa

CALIBRATION SOURCE PROPERTIES

Type/Producer: Pressurements deadweight tester P3223-1
SN: 66256
Uncertainty [%]: 0,01

POLY FIT EQUATION:

$Y = -402.46645267E+0X^0 + 199.91920601E+0X^1$

CALIBRATION SUMMARY:

Max Uncertainty : 0.390531 [%]
Max Uncertainty : 0.514565 [kPa]
RSQ : 0.999997
Calibration points : 49

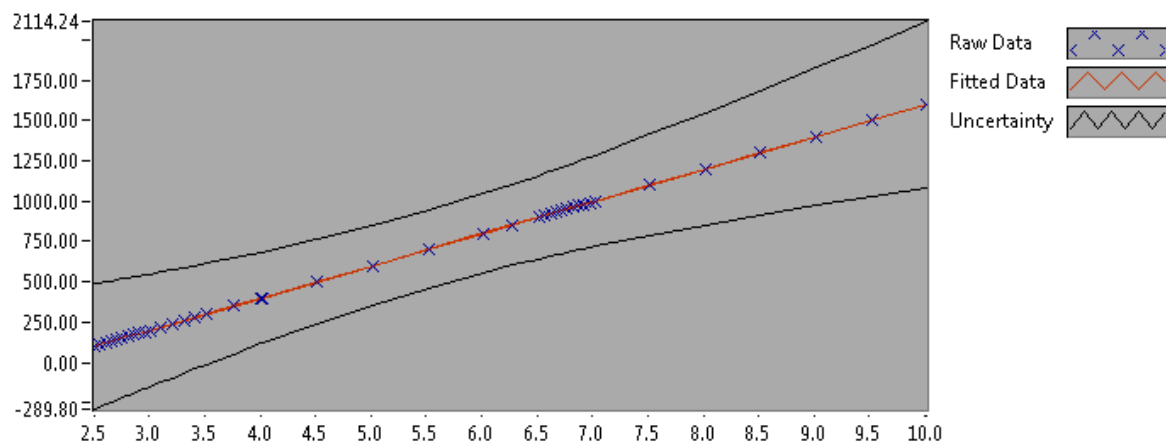


Figure 1 : Calibration chart (The uncertainty band is multiplied by 1000)

CALIBRATION VALUES

Value [kPa]	Voltage [V]	Best Poly Fit [kPa]	Deviation [kPa]	Uncertainty [%]	Uncertainty [kPa]
99.422200	2.505694	98.469841	0.952359	0.390531	0.388275
109.437307	2.555776	108.482227	0.955081	0.351128	0.384265
119.452414	2.606218	118.566572	0.885842	0.318319	0.380240
129.467521	2.656682	128.655354	0.812167	0.290612	0.376248
139.482629	2.706969	138.708675	0.773954	0.266913	0.372298
149.497736	2.757449	148.800559	0.697176	0.246401	0.368365
159.512843	2.807858	158.878336	0.634506	0.228484	0.364462
169.527950	2.858642	169.030906	0.497044	0.212687	0.360563
179.543057	2.908574	179.013365	0.529691	0.198705	0.356760
189.558164	2.958930	189.080519	0.477645	0.186201	0.352959
199.573271	3.009191	199.128562	0.444709	0.174971	0.349195
219.603485	3.109895	219.261296	0.342189	0.155624	0.341757
239.633699	3.210575	239.389185	0.244515	0.139581	0.334482
259.663914	3.311270	259.519980	0.143934	0.126069	0.327356
279.694128	3.412014	279.660608	0.033520	0.114548	0.320385
299.724342	3.512344	299.718550	0.005792	0.104644	0.313643
349.799878	3.763793	349.987984	-0.188107	0.085070	0.297576
399.875413	4.015139	400.237040	-0.361627	0.070755	0.282933
500.026484	4.517458	500.660252	-0.633768	0.051751	0.258766
600.177555	5.019121	600.952298	-0.774743	0.040510	0.243129
700.328626	5.520668	701.221110	-0.892484	0.033938	0.237677
800.479697	6.021989	801.444864	-0.965167	0.030353	0.242972
850.555232	6.272357	851.498229	-0.942997	0.029347	0.249609
900.630768	6.522485	901.503613	-0.872845	0.028700	0.258483
910.645875	6.572692	911.540907	-0.895032	0.028600	0.260448
920.660982	6.622745	921.547397	-0.886415	0.028526	0.262632
930.676089	6.672774	931.549201	-0.873113	0.028447	0.264752
940.691158	6.722783	941.547055	-0.855898	0.028376	0.266929
950.706265	6.772853	951.556963	-0.850698	0.028350	0.269530
960.721372	6.822837	961.549800	-0.828428	0.028298	0.271862
970.736479	6.872987	971.575712	-0.839233	0.028253	0.274263
980.751586	6.922954	981.564927	-0.813341	0.028228	0.276842
990.766693	6.972920	991.554257	-0.787564	0.028218	0.279570
1000.781800	7.022044	1001.374964	-0.593164	0.028194	0.282162
1100.932871	7.521687	1101.263217	-0.330346	0.028383	0.312480
1201.083942	8.021216	1201.128684	-0.044742	0.028941	0.347607
1301.235013	8.520208	1300.886734	0.348279	0.029678	0.386178
1401.386084	9.018661	1400.537111	0.848973	0.030490	0.427276
1501.537155	9.516796	1500.123794	1.413361	0.031317	0.470238
1601.688226	10.014348	1599.594109	2.094117	0.032122	0.514502
1601.688226	10.014768	1599.677999	2.010227	0.032126	0.514565
1501.537155	9.517160	1500.196636	1.340518	0.031320	0.470281
1401.386084	9.019017	1400.608252	0.777832	0.030496	0.427366
1201.083942	8.021824	1201.250178	-0.166236	0.028944	0.347642
1000.781800	7.022707	1001.507562	-0.725761	0.028194	0.282157
800.479658	6.022371	801.521231	-1.041573	0.030354	0.242978
600.177516	5.019802	601.088350	-0.910833	0.040522	0.243202
399.875375	4.015653	400.339736	-0.464361	0.070755	0.282932
199.573233	3.010039	199.298185	0.275047	0.174936	0.349125

COMMENTS:

C.4 FRICTION TORQUE TRANSDUCER

CALIBRATION REPORT

CALIBRATION PROPERTIES

Calibrated by: Jonas B. Bertelsen
Type/Producer: Load beam force cell Z6 HBM
SN: 0
Range: 0-10Nm
Unit: Nm

CALIBRATION SOURCE PROPERTIES

Type/Producer: Calibrated weights
SN:
Uncertainty [%]: 0,01

POLY FIT EQUATION:

$Y = -4.94075805E+0X^0 + 1.30857957E+0X^1$

CALIBRATION SUMMARY:

Max Uncertainty : Inf [%]
Max Uncertainty : 0.109429 [Nm]
RSQ : 0.998482
Calibration points : 12

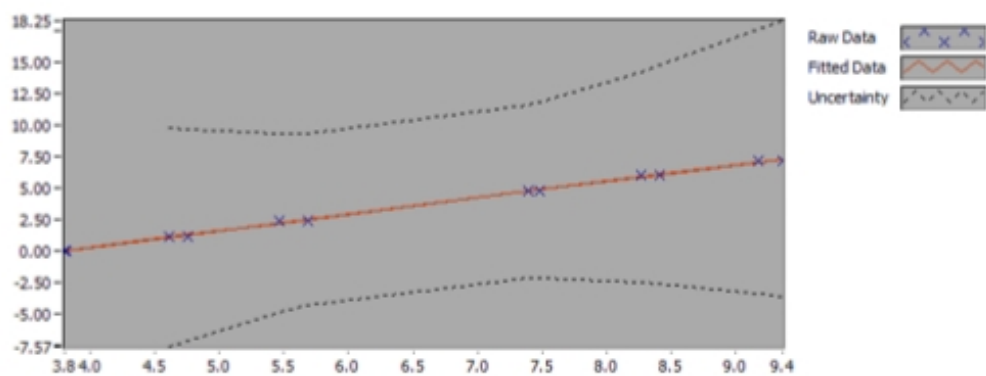


Figure 1 : Calibration chart (The uncertainty band is multiplied by 100)

Jonas B. Bertelsen

Value [Nm]	Voltage [V]	Best Poly Fit [Nm]	Deviation [Nm]	Uncertainty [%]	Uncertainty [Nm]
0.000000	3.816609	0.053578	-0.053578	Inf	NaN
1.193308	4.750257	1.275331	-0.082023	7.019077	0.083759
2.391527	5.682791	2.495626	-0.104099	2.832234	0.067734
4.797786	7.484461	4.853255	-0.055469	1.447632	0.069454
5.992321	8.411266	6.066052	-0.073731	1.442746	0.086454
7.157393	9.361357	7.309322	-0.151930	1.528890	0.109429
7.157393	9.172049	7.061598	0.095794	1.460941	0.104565
5.992321	8.267521	5.877951	0.114370	1.391290	0.083371
4.797786	7.385359	4.723572	0.074214	1.420103	0.068134
2.391527	5.468689	2.215457	0.176069	2.954176	0.070650
1.193308	4.613547	1.096435	0.096873	7.265910	0.086705
0.000000	3.803550	0.036490	-0.036490	Inf	NaN